

DISS. ETH NO. 30072

PLASMA CONTROL OF THERMOACOUSTIC
INSTABILITIES IN A SEQUENTIAL
COMBUSTOR

A dissertation submitted to attain the degree of

DOCTOR OF SCIENCES
(Dr. sc. ETH Zurich)

presented by

BAYU ADI DHARMAPUTRA
MSc ETH, ETH Zurich

born on 13.09.1995

accepted on the recommendation of

Prof. Dr. Nicolas Noiray
Prof. Dr. Christian Oliver Paschereit
Prof. Dr. Deanna Lacoste

2024

To my parents, brother, and family

ABSTRACT

Climate change and global warming, significantly caused by greenhouse gas emissions from human activities, pose various serious problems, including negative impacts on health, significant sea level rise, food instability, and various social issues. Intensive decarbonization needs to be carried out in various sectors, especially the electricity and heat production sector, which is the largest contributor to the carbon dioxide and greenhouse gases emissions. This has encouraged the development of renewable sources, such as solar and wind, for electricity generation to reduce dependence on fossil fuels. However, these energy sources often have elements of uncertainty and intermittency, as they are highly dependent on weather conditions.

The fluctuating nature of renewable energy sources presents a challenge in maintaining a constant equilibrium between electricity supply and demand in the electric grid. In this context, modern gas turbines could be a viable solution to bridge this gap. When these turbines are part of a combined cycle power plant—where both gas and steam turbines work in tandem—they operate at a high efficiency rate of around 60%, and have a quick load response to adapt to the demand of the grid. Furthermore, modern gas turbines have very low NO_x emissions at wide range of operating loads.

A leading example of modern gas turbine technology is the constant pressure sequential combustor (CPSC). This CPSC concept uses two combustion chambers arranged in series, increasing the gas turbine's flexibility to burn various types of fuels, including hydrogen, in a safe and efficient manner. Additionally, this technology offers a wider operational load range compared to gas turbine configurations that only have one combustion chamber.

However, thermoacoustic instability, arising from the constructive interaction between the acoustics of the combustion chamber and the flame heat release rate, can disrupt operations and damage components. Passive control methods such as Helmholtz dampers and quarter-wave resonators are common in practical combustors. Active control strategies could offer a wider operational range as they can adapt to changes in operating conditions. However, their implementation is rather limited due to the lack of fast and robust actuators. Recent advances in nanosecond repetitively pulsed discharges (NRPD) show great potential for active control of thermoacous-

tic instabilities. The main benefit of such an actuator is that it involves no moving parts and hence could be retrofitted to the existing combustor without major geometry modifications.

This thesis studies the application of NRPDs to control the thermoacoustic instabilities of a lab-scale sequential combustor. The discharges are generated by applying high voltage across a pair of electrodes in pin-to-pin configuration. The electrodes are strategically placed within a mixing duct, located downstream of the first-stage combustion chamber and upstream of the sequential burner outlet. This specific location is advantageous due to the gas temperature, which typically exceeds 1000 K. The elevated temperature results in a lower gas density, consequently reducing the voltage needed to initiate plasma breakdown.

The effect of NRPD parameters, such as generator voltage and pulse repetition frequency (PRF), on the thermoacoustic stability and NO emissions of a lab-scale sequential combustor is investigated through experiments at atmospheric pressure. High-speed OH* chemiluminescence imaging was employed to visualize the dynamics of the sequential flame. The study shows that NRPDs with a mean plasma power of 1.5×10^{-3} percent of the thermal power of the flame can effectively stabilize the thermoacoustics of the sequential combustor. However, in certain parameter combinations, NRPDs can inadvertently enhance thermoacoustic instabilities. This underscores the importance of developing an adaptive control algorithm to optimize control parameters safely and efficiently.

The optimization of control parameters is achieved using safe Bayesian optimization algorithms which are data-driven and do not require a model. However, the inclusion of a model is possible by incorporating it as a prior mean function. Three Bayesian optimization algorithms are presented, each with unique properties. The framework also allows for transfer of knowledge between operating conditions of the combustor through the use of Bayesian context. The performance of the algorithms is demonstrated via a numerical simulation using a low-order thermoacoustic network and two distinct experimental setups. The advantages and limitations of the algorithms are also discussed in detail.

The sequential flame could be sensitive to the upstream temperature fluctuations. To experimentally measure the acoustic response of the sequential flame, it is necessary to use a fast and robust temperature sensor. An advanced laser absorption spectroscopy method is developed to facilitate temperature measurement at a high sampling rate. The method is tunable diode laser absorption spectroscopy with wavelength modulation

spectroscopy (TDLAS-WMS). The efficacy of this sensor was tested using a single-stage premixed swirling flame setup, and peculiar entropic responses of the flame were uncovered.

Real gas turbines frequently operate under varying loads, which involve transient load changes. Thus, controlling the thermoacoustics during these transitions is essential. The effectiveness of NRPDs under transient operation was investigated using the same sequential combustor setup, located inside a high-pressure vessel. The first method entailed altering the outlet area geometry of the combustor transiently, while the second involved a simultaneous transient ramp-up of both power and combustor pressure. The combustor pressure in the experiments ranged from 4 to 6 bar. The ability of NRPD to stabilize the thermoacoustics is discussed, and novel results are presented.

In general, this thesis explores different aspects of active control of thermoacoustic instabilities in sequential combustor, including experimental demonstrations at atmospheric and high pressure, the establishment of data-driven algorithms to optimize the control parameters, and the development of a fast and robust temperature sensor.

ZUSAMMENFASSUNG

Der Klimawandel und die globale Erwärmung, die maßgeblich durch die vom Menschen verursachten Treibhausgasemissionen verursacht werden, stellen verschiedene schwerwiegende Probleme dar, darunter negative Auswirkungen auf die Gesundheit, einen erheblichen Anstieg des Meeresspiegels, die Instabilität der Nahrungsmittelversorgung und verschiedene soziale Probleme. Eine intensive Dekarbonisierung muss in verschiedenen Sektoren durchgeführt werden, insbesondere im Bereich der Strom- und Wärmeerzeugung, der am meisten zu den Kohlendioxid- und Treibhausgasemissionen beiträgt. Dies hat die Entwicklung von erneuerbaren Energiequellen wie Sonnen- und Windenergie für die Stromerzeugung gefördert, um die Abhängigkeit von fossilen Brennstoffen zu verringern. Diese Energiequellen unterliegen jedoch häufig Schwankungen, da sie stark von den Wetterbedingungen abhängen.

Die schwankende Verfügbarkeit erneuerbarer Energiequellen stellt eine Herausforderung für die Aufrechterhaltung eines konstanten Gleichgewichts zwischen Stromangebot und -nachfrage im Stromnetz dar. In diesem Zusammenhang könnten moderne Gasturbinen eine praktikable Lösung sein, um diese Lücke zu schließen. Wenn diese Turbinen Teil eines Kombikraftwerks sind, in dem Gas- und Dampfturbinen zusammenarbeiten, erreichen sie einen hohen Wirkungsgrad von etwa 60 %, und können sich schnell an den Bedarf des Netzes anpassen. Darüber hinaus haben moderne Gasturbinen sehr niedrige NO_x -Emissionen bei einer großen Bandbreite von Betriebslasten.

Ein führendes Beispiel für die moderne Gasturbinentechnologie ist die sequentielle Brennkammer mit konstantem Druck (constant pressure sequential combustor, CPSC). Dieses CPSC-Konzept verwendet zwei hintereinander angeordnete Brennkammern und erhöht die Flexibilität der Gasturbine bei der sicheren und effizienten Verbrennung verschiedener Arten von Brennstoffen, einschließlich Wasserstoff. Außerdem bietet diese Technologie im Vergleich zu Gasturbinenkonfigurationen mit nur einer Brennkammer einen größeren Betriebslastbereich.

Allerdings können thermoakustische Instabilitäten, die durch die konstruktive Wechselwirkung zwischen der Akustik der Brennkammer und der Wärmefreisetzungsrate der Flamme entstehen, den Betrieb stören und Komponenten beschädigen. Passive Regelungsmethoden wie Helmholtz-

Dämpfer und Viertelwellenresonatoren sind in Brennkammern häufig zu finden. Aktive Regelungsstrategien erlauben einen größeren Betriebsbereich, da sie sich an Änderungen der Betriebsbedingungen anpassen können. Ihre Umsetzung ist jedoch aufgrund des Mangels an schnellen und robusten Aktuatoren eher begrenzt. Jüngste Fortschritte im Bereich der repetitiv gepulsten Plasmaentladungen im Nanosekundenbereich (nanosecond repetitively pulsed discharges, NRPD) zeigen ein großes Potenzial für die aktive Regelung thermoakustischer Instabilitäten. Der Hauptvorteil eines solchen Aktuators besteht darin, dass er ohne bewegliche Teile auskommt und daher ohne größere geometrische Änderungen in bestehende Brennkammern nachgerüstet werden kann.

In dieser Arbeit wird die Anwendung von NRPDs zur Unterdrückung thermoakustischer Instabilitäten in einer sequenziellen Brennkammer im Labormaßstab untersucht. Die Entladungen werden durch Anlegen einer Hochspannung an ein Elektrodenpaar in Stift-zu-Stift-Konfiguration erzeugt. Die Elektroden sind strategisch innerhalb eines Mischungskanals platziert, der sich stromabwärts der Brennkammer der ersten Stufe und stromaufwärts des Auslasses des sequentiellen Brenners befindet. Diese spezielle Anordnung ist aufgrund der Gastemperatur, die in der Regel über 1000 K liegt, von Vorteil. Die höhere Temperatur führt zu einer geringeren Gasdichte und damit zu einer geringeren Spannung, die für die Zündung des Plasmas erforderlich ist.

Die Auswirkung von NRPD-Parametern wie Generatorspannung und Pulswiederholungsfrequenz (PRF) auf die thermoakustische Stabilität und die NO-Emissionen einer sequentiellen Brennkammer im Labormaßstab wird durch Experimente bei atmosphärischem Druck untersucht. Zur Visualisierung der Dynamik der sequenziellen Flamme wurde die Hochgeschwindigkeits Chemilumineszenz Bildgebung von OH^* eingesetzt. Die Studie zeigt, dass NRPDs mit einer mittleren Plasmaleistung von $1,5 \times 10^{-3}$ Prozent der thermischen Leistung der Flamme die Thermoakustik des sequentiellen Brenners effektiv stabilisieren können. Bei bestimmten Parameterkombinationen können NRPDs jedoch unbeabsichtigt thermoakustische Instabilitäten verstärken. Dies unterstreicht die Bedeutung der Entwicklung eines adaptiven Regelalgorithmus zur sicheren und effizienten Optimierung der Regelparameter.

Die Optimierung der Regelungsparameter erfolgt mit sicheren Bayes'schen Optimierungsalgorithmen, die datengesteuert sind und kein Modell erfordern. Die Einbeziehung eines Modells ist jedoch möglich, indem man es als a-priori Mittelwertfunktion einbezieht. Es werden drei Bayes'sche

Optimierungsalgorithmen vorgestellt, die sich durch unterschiedliche Eigenschaften auszeichnen. Das Framework ermöglicht auch die Übertragung von Informationen zwischen verschiedenen Betriebsbedingungen durch die Verwendung von Bayes'schem Kontext. Die Leistungsfähigkeit der Algorithmen wird anhand einer numerischen Simulation unter Verwendung eines thermoakustischen Netzwerkmodells niedriger Ordnung und zweier unterschiedlicher Versuchsaufbauten demonstriert. Die Vorteile und Grenzen der Algorithmen werden ebenfalls im Detail diskutiert.

Die sequenzielle Flamme könnte sensitiv auf die stromaufwärts gelegenen Temperaturschwankungen reagieren. Um die akustische Antwort der sequenziellen Flamme experimentell zu messen, ist es notwendig, einen schnellen und robusten Temperatursensor zu benutzen. Es wurde eine fortschrittliche Laserabsorptionsspektroskopie-Methode entwickelt, um die Temperaturmessung mit einer hohen Abtastrate zu ermöglichen. Bei der Methode handelt es sich um abstimmbare Diodenlaser Absorptionsspektroskopie mit Wellenlängenmodulation (TDLAS-WMS). Die Wirksamkeit dieses Sensors wurde an einer einstufigen, vorgemischten Wirbelflamme getestet, und es wurden besondere entropische Reaktionen der Flamme aufgezeigt.

Reale Gasturbinen werden häufig unter wechselnden Lasten betrieben, die mit transienten Lastwechseln einhergehen. Daher ist die Kontrolle der Thermoakustik während dieser Übergänge von wesentlicher Bedeutung. Die Wirksamkeit von NRPDs bei instationärem Betrieb wurde mit der gleichen sequentiellen Brennkammer in einem Hochdruckbehälter untersucht. Bei der ersten Methode wurde die Geometrie der Auslassöffnung der Brennkammer transient verändert, während bei der zweiten Methode sowohl die Leistung als auch der Druck in der Brennkammer transient erhöht wurden. Der Druck in der Brennkammer lag bei den Versuchen zwischen 4 und 6 bar. Die Fähigkeit von NRPD, die Thermoakustik zu stabilisieren, wird erörtert, und es werden neue Ergebnisse vorgestellt.

Im Allgemeinen werden in dieser Arbeit verschiedene Aspekte der aktiven Kontrolle thermoakustischer Instabilitäten in sequenziellen Brennkammern untersucht. Dazu gehören experimentelle Untersuchungen bei atmosphärischem und bei hohem Druck, die Entwicklung datengesteuerter Algorithmen zur Optimierung der Regelungsparameter und die Entwicklung eines schnellen und robusten Temperatursensors.

ABSTRAK

Perubahan iklim dan pemanasan global yang sebagian besar disebabkan oleh emisi gas rumah kaca dari aktivitas manusia menimbulkan berbagai masalah serius, antara lain dampak negatif terhadap kesehatan, kenaikan permukaan air laut yang signifikan, ketidakstabilan pangan, dan berbagai masalah sosial. Dekarbonisasi secara intensif perlu dilakukan di berbagai sektor, terutama sektor produksi listrik dan panas, yang merupakan penyumbang emisi karbon dioksida dan gas rumah kaca terbesar. Hal ini mendorong pengembangan sumber-sumber energi terbarukan, seperti tenaga surya dan angin, untuk pembangkitan listrik guna mengurangi ketergantungan terhadap bahan bakar fosil. Namun, sumber-sumber energi ini sering kali memiliki unsur ketidakpastian dan intermiten, karena sangat bergantung pada kondisi cuaca.

Sifat fluktuatif dari sumber energi terbarukan menjadi tantangan dalam menjaga keseimbangan antara pasokan dan permintaan listrik di jaringan listrik. Dalam konteks ini, turbin gas modern dapat menjadi solusi yang tepat untuk menjaga keseimbangan tersebut. Ketika turbin ini menjadi bagian dari pembangkit listrik siklus gabungan - di mana turbin gas dan uap bekerja bersama-sama (pembangkit listrik tenaga gas uap)- turbin ini beroperasi pada tingkat efisiensi yang tinggi, yaitu sekitar 60%, dan memiliki respons yang cepat untuk beradaptasi dengan permintaan jaringan listrik. Selain itu, turbin gas modern memiliki emisi NO_x yang sangat rendah pada berbagai macam beban operasi.

Contoh utama dari teknologi turbin gas modern adalah *constant pressure sequential combustor* (CPSC). Konsep CPSC ini menggunakan dua ruang bakar yang disusun secara seri, sehingga meningkatkan fleksibilitas turbin gas untuk membakar berbagai jenis bahan bakar, termasuk hidrogen, dengan cara yang aman dan efisien. Selain itu, teknologi ini menawarkan rentang beban operasional yang lebih luas dibandingkan dengan konfigurasi turbin gas yang hanya memiliki satu ruang bakar.

Namun, ketidakstabilan termoaustik, yang timbul dari interaksi konstruktif antara akustik dari ruang bakar dan laju pelepasan panas api, dapat mengganggu operasi dan merusak komponen. Metode kontrol pasif seperti peredam Helmholtz (*Helmholtz damper*) dan resonator seperempat gelombang (*Quarter-wave resonator*) adalah contoh yang umum digunakan di turbin gas komersil. Strategi kontrol aktif dapat menawarkan jangkauan

operasional yang lebih luas karena dapat beradaptasi dengan perubahan kondisi operasi. Namun, implementasinya terbatas karena kurangnya aktuatur yang cepat dan kuat. Riset-riset dan perkembangan terbaru dalam *nanosecond repetitively pulsed discharges* (NRPDs) menunjukkan potensi besar untuk aplikasi kontrol aktif. Manfaat utama dari aktuatur tersebut adalah tidak adanya bagian yang bergerak dan oleh karena itu dapat diimplementasikan di turbin gas yang sudah ada tanpa modifikasi geometri yang signifikan.

Disertasi ini mempelajari penerapan NRPD untuk mengontrol ketidakstabilan termoakustik dari *sequential combustor* skala laboratorium. Plasma dihasilkan dengan menerapkan tegangan tinggi pada sepasang elektroda dalam konfigurasi *pin-to-pin*. Elektroda ditempatkan secara strategis di dalam sebuah saluran, yang terletak di bagian hilir ruang bakar tahap pertama dan di bagian hulu ruang bakar kedua. Lokasi spesifik ini menguntungkan karena suhu gas, yang biasanya melebihi 1000 K. Suhu yang tinggi membuat masa jenis gas menjadi lebih rendah, sehingga mengurangi tegangan yang dibutuhkan untuk memulai plasma.

Pengaruh parameter NRPD, seperti tegangan generator dan frekuensi repetisi (*pulse repetition frequency*), pada stabilitas termoakustik dan emisi NO dari pembakaran berurutan skala laboratorium dipelajari melalui eksperimen pada tekanan atmosfer. Pencitraan *chemiluminescence* OH* berkecepatan tinggi digunakan untuk menggambarkan dinamika nyala api. Studi ini menunjukkan bahwa NRPD dengan daya plasma rata-rata 10^{-3} persen dari daya termal nyala api dapat secara efektif menstabilkan termoakustik CPSC. Namun, dalam kombinasi parameter tertentu, NRPD dapat meningkatkan ketidakstabilan termoakustik. Hal ini menggarisbawahi pentingnya mengembangkan algoritma kontrol adaptif untuk mengoptimalkan parameter kontrol secara aman dan efisien.

Optimalisasi parameter kontrol dicapai dengan menggunakan *safe Bayesian optimization* yang cara kerjanya berdasarkan data dan tidak memerlukan model. Namun, penyertaan model dapat dilakukan dengan menjadikannya sebagai nilai rata-rata. Tiga algoritma optimasi Bayesian disajikan, masing-masing dengan keunggulan yang unik. Kerangka kerja ini juga memungkinkan untuk mentransfer informasi di antara kondisi-kondisi operasi dari CPSC. Kinerja dari masing-masing algoritma ditunjukkan melalui simulasi numerik dan dua eksperimen yang berbeda. Keuntungan dan keterbatasan dari setiap algoritma juga dibahas secara rinci.

Api kedua dari CPSC, dibagian hilir, dapat memiliki respon yang sensitif terhadap perubahan suhu di belakangnya. Untuk mengukur respons akus-

tik dari api yang kedua secara eksperimental, dibutuhkan sebuah sensor suhu yang cepat dan tangguh. Metode spektroskopi penyerapan laser (*laser absorption spectroscopy*) yang canggih dikembangkan untuk memfasilitasi pengukuran suhu pada tingkat pengambilan sampel yang tinggi. Metode ini menggunakan laser dioda yang dimodulaskan dan dikenal dengan *tunable diode laser absorption spectroscopy with wavelength modulation spectroscopy* (TDLAS-WMS). Keampuhan sensor ini diuji di eksperimen dengan satu ruang bakar dan satu api di dalamnya. Hasil pengukuran menunjukkan respons entropik yang unik dari api tersebut.

Dalam praktik nyata, turbin gas beroperasi dengan beban yang bervariasi, yang melibatkan perubahan beban transien. Oleh karena itu, mengendalikan termoakustik pada situasi transien ini sangat penting. Efektivitas NRPD di bawah operasi transien diselidiki di disertasi ini dengan menggunakan konfigurasi eksperimen CPSC yang sama, namun diletakkan di dalam bejana bertekanan tinggi. Pada metode pertama, geometri saluran keluar diubah secara transien, sedangkan metode kedua melibatkan peningkatan daya dan tekanan secara serentak. Tekanan pembakaran dalam percobaan berkisar antara 4 hingga 6 bar. Kemampuan NRPD untuk menstabilkan termoakustik dibahas, dan hasil-hasil baru dipresentasikan.

Secara umum, disertasi ini menggali berbagai aspek kontrol aktif ketidakstabilan termoakustik dalam CPSC. Aspek-aspek tersebut meliputi demonstrasi eksperimental pada tekanan atmosfer dan tekanan tinggi, pembentukan algoritma-algoritma berbasis data untuk mengoptimalkan parameter kontrol, dan pengembangan sensor suhu yang cepat, akurat dan tangguh.

ACKNOWLEDGEMENTS

This dissertation represents the culmination of research I conducted at the Combustion and Acoustics for Power & Propulsion Systems (CAPS) Laboratory, generously funded by the European Research Council (ERC) via the ERC Consolidator Grant (No: 820091) TORCH (2019-2024). The journey to this point has been made possible by the support and contributions of numerous individuals to whom I wish to thank.

My doctoral study journey began in 2019, shortly after finishing my master's studies in the CAPS lab. Reflecting on my time at ETH Zurich, I recognize the exceptional opportunities I have been afforded, particularly the chance to work under the guidance of Prof. Noiray. As a mentor and supervisor, his approachability, open communication, and insightful guidance have been invaluable. I extend my heartfelt thanks to him for his unwavering support and confidence in me throughout this research endeavor, which has been as challenging as it has been rewarding.

The initial phase of my research involved enhancing laser absorption spectroscopy method, a progression from my master's thesis. I recall the countless hours dedicated to refining this technique, a task I could not have tackled without the expertise of Yuan Xiong, my master's thesis supervisor and then-colleague. From Yuan, I gained a wealth of knowledge in laser alignment, data analysis, and imaging. My deepest appreciation goes to Yuan for the invaluable discussions.

The core of my research focused on plasma discharges within a sequential combustor setup. This endeavor involved extensive experimentation and intricate data analysis. Throughout this rigorous process, my colleague, Sergey Shcherbanev, was an indispensable source of support. His profound knowledge in plasma physics, an inherently intricate and multifaceted field, greatly enhanced my understanding. I am deeply grateful for his assistance, persistent patience, and invaluable insights. I extend my heartfelt thanks to Bruno Schuermans for his guidance and invaluable support throughout this project. His expertise in thermoacoustics has clearly improved my understanding, and it is such a privilege to have worked with him. I also wish to express my gratitude to Stephan Caruso, the lab manager of the CAPS Lab, for his invaluable assistance with the experiments. His involvement in everything from planning to commissioning the high-pressure test rig, as well as various other lab-related tasks, was indispensable.

Special thanks to Prof. Deanna Lacoste and Prof. Christian Oliver Paschereit for their willingness to be part of my doctoral examination. Their work has been instrumental part of my inspiration during my research and it is a privilege that I deeply appreciate having both of them in the committee.

I extend my gratitude to the entire TORCH team as well. I am particularly thankful to the team's numerical experts, Matteo and Quentin, who executed advanced simulations that significantly enhanced our understanding of the physics of plasma-assisted combustion. I also owe a debt of gratitude to Richard, our expert in passive control, for his generosity in translating the abstract into German.

Thanks to the former members of CAPS lab: Roberto, Audrey, Luigi, Alex, and Georg. The lab has not been the same without your presence, but the legacy of your work continues to inspire us. I am grateful to the current members of the CAPS lab, first, to those in the affectionately known as the 'fun office': Bogdan, Kihun, Abel, and Florian. Conversations with them have expanded my scientific perspective and, amusingly, have somewhat improved my less-than-stellar foosball skills. Secondly, to the lab's theoreticians, Tiemo and Alex, with whom I engaged in discussions about 'complicated' subjects whenever I found myself missing such intellectual challenges.

I extend my sincere thanks to my former students: Alan, Pit, Tobias, and Lukas. Their dedication and hard work have yielded fantastic results and made a significant contribution to this research journey. It was a pleasure to have them at CAPS Lab.

I am deeply grateful to my parents, who have been my source of encouragement throughout my doctoral journey. They have always been committed to ensuring that I received the finest education and consistently motivated me to excel in all my endeavors. A heartfelt thank you to my dear papa and mama; this thesis is dedicated to both of you. I also extend my thanks to my younger brother, Bima, who has been the source of joy and entertainment every time he visited me in Switzerland. Amusingly, at the time of writing this thesis, he was also in the midst of writing his own.

Lastly, to my dear beloved Adelina, who has been a lovely partner and has been giving me unwavering support emotionally and intellectually throughout this challenging journey. Your presence has been a fundamental source of my happiness; I am sure that without you, I would not be half as happy as I am now, a thought I do not wish to entertain. I owe you more than words can express.

CONTENTS

1	Introduction	1
1.1	Motivation	1
1.2	World energy consumption and production	4
1.3	Sequential combustor	11
1.3.1	GT24/GT26 Gas Turbine	11
1.3.2	GT36 Gas Turbine	14
1.4	Thermoacoustic instabilities	16
1.5	Plasma-assisted combustion	22
1.6	Scope and structure of the thesis	26
2	Thermoacoustic stabilization of a sequential combustor with ultra-low-power nanosecond repetitively pulsed discharges.	29
2.1	Introduction	29
2.2	Experimental Setup	33
2.3	Results	37
2.4	Conclusions and outlook	53
3	BOATS: Bayesian Optimization for Active Control of ThermoacousticS	55
3.1	Introduction	55
3.2	Background Theory	60
3.2.1	Problem Statement	60
3.2.2	Gaussian Process	61
3.2.3	Safe Bayesian optimization (SafeOpt)	62
3.2.4	Modifications of safeOpt	67
3.2.5	Bayesian Context	68
3.3	Experimental Setup	70
3.3.1	Single stage combustor	70
3.3.2	Sequential combustor	71
3.4	Thermoacoustic Network Model	72
3.5	Results	75
3.5.1	Numerical validation	76
3.5.2	Experimental validation	79
3.6	Conclusions and outlook	95
4	Entropy Transfer Function Measurement with Tunable Diode Laser Absorption Spectroscopy	97
4.1	Introduction	97

4.2	Experimental set-up	99
4.2.1	Turbulent Combustor	99
4.2.2	Optical Setup	101
4.3	Methodology	101
4.3.1	Laser Absorption Spectroscopy (LAS)	101
4.3.2	Wavelength Modulation Spectroscopy (WMS)	102
4.3.3	Entropy Transfer Function	106
4.3.4	Flame Transfer Function	107
4.4	Results and discussion	107
4.5	Conclusion	114
5	Plasma Assisted Thermoacoustic Stabilization of a Transiently Operated Sequential Combustor at High Pressure	117
5.1	Introduction	117
5.2	Experimental set-up	119
5.3	Methodology	121
5.3.1	Plasma energy deposition	121
5.3.2	Operation of the sequential combustor	122
5.4	Results and discussion	123
5.4.1	Steady-state mapping	123
5.4.2	Transient operation	128
5.5	Conclusion	131
6	Summary and Outlook.	133
A	Feedback control of thermoacoustic in a sequential combustor with NRPD	139
A.1	Introduction	139
A.2	Setup	140
A.2.1	Experimental setup	140
A.2.2	Extended Kalman filter	141
A.3	Results	143
A.4	Conclusion and Outlook	147
	Bibliography	149

NOTATION

FREQUENTLY USED SYMBOLS

P	power
p	pressure
u	velocity
Q	heat release rate
E_D	energy deposition
V	voltage
I	current
ρ	density
τ	time delay
f	frequency
ω	angular frequency

ABBREVIATIONS

CPSC	Constant Pressure Sequential Combustor
FTF	Flame Transfer Function
TDLAS	Tunable Diode Laser Absorption Spectroscopy
WMS	Wavelength Modulation Spectroscopy
NRPD	Nanosecond Repetitively Pulsed Discharge
ETF	Entropy Transfer Function
PRF	Pulse Repetition Frequency
FGH	Fast Gas Heating

INTRODUCTION

The duty of the man who investigates the writings of scientists, if learning the truth is his goal, is to make himself an enemy of all that he reads, and attack it from every side. He should also suspect himself as he performs his critical examination of it, so that he may avoid falling into either prejudice or leniency

— Alhazen Ibn al-Haytham

1.1 MOTIVATION

Historically, controlled fire has been a key tool for human progress, with archaeological evidence indicating its early use dating back nearly a million years [1]. These ancient applications of fire were diverse, ranging from culinary practices to personal protection and wildlife management. Indeed, the ability to harness combustion has been a transformative force, playing a critical role in shaping the trajectory of human advancement. Perhaps,

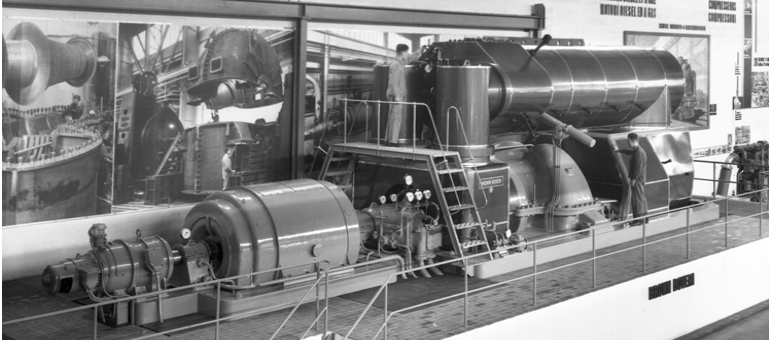


FIGURE 1.1: Cartoon illustration of early humans gathering around a campfire.
Generated with GPT-Vision

one of the most significant benefits of controlled fire was the ability to cook food, thus changing the quality of the human diet with the accompanying

increases in brain size [2]. Fire has played an important role in the intellectual development of global civilisations. The concept of fire has changed in the minds of humans, polarizing between fire that is revered, worshiped, and used, to being feared and suppressed as the population moves within the landscape [2].

a)



b)

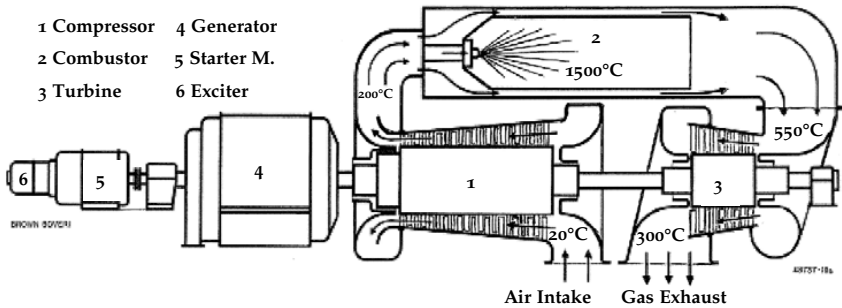


FIGURE 1.2: Photograph a) and schematic diagram b) of the first single cycle gas-turbine for electricity production in Neuchâtel, Switzerland. Images taken from [3]

Before the industrial revolution in the 1800s, humans relied on burning biomass for heat generation. During the industrial revolution, fossil fuel combustion began to be used on a large scale for energy production, raw materials, the manufacture of various goods, mainly steel, and transportation, for example, via steam engines, which were invented by James Watt in

1769 [4]. Later in 1791, John Barber, an English inventor, obtained a patent for an early gas turbine engine. The design was similar to that of a modern gas turbine engine, which includes compressor, combustor, and turbine. Frank Whittle in the 1930s also patented a design of a jet engine for a propulsion system. His design later on was implemented in an aircraft and inspired many modern jet engines today. In 1939, the first commercially operated gas turbine for electricity in the world was installed in Neuchâtel, Switzerland. Construction was carried out by Brown Boveri Company (BBC). The power of the gas turbine was 4 MW with a thermal efficiency of about 18% [3]. Figure 1.2 shows the image of the first Neuchâtel gas turbine during an exhibition and the schematic diagram of the engine. The gas turbine was awarded the GT Neuchâtel Historic Mechanical Landmark status in 1988 by ASME (American Society of Mechanical Engineers). Later on in 2005, Alstom (Switzerland) Ltd. relocated the engine to Birr, which is 14 km away from Baden.

Today, gas turbine engines are often used both for propulsion and power generation. However, since the engine fuel is dominated mainly by fossil fuels, it generates CO_2 and NO_x emissions and therefore contributes to global warming. One way to reduce NO_x emissions is to burn in a lean premixed condition to reduce the temperature. To reduce CO_2 emissions, a hydrogen mixture could be added to the fuel, thus lowering the carbon content of the fuel for the same thermal power. The hydrogen could be produced by electrolysis using energy generated from renewable sources such as solar PV and wind turbines. However, the design of the combustion chamber and the burner might need to be changed to avoid flame flashback due to increased mixture reactivity.

Thermoacoustic instabilities have remained a major challenge in the development of new gas turbines. The explanation of thermoacoustic instability will be elaborated in the subsequent sections, essentially, it is a constructive coupling between the acoustic field of the combustor and the heat release rate fluctuations of the flame, which induce typically high amplitude pulsation. It is more pronounced in the low emission premixed combustor configuration compared to the non-premixed one. This thesis focuses mainly on the development of active control strategies and actuators to suppress thermoacoustic instabilities in a constant pressure sequential combustor.

In the next section, the role of combustion in global energy production, its contribution to global warming, and its role in future energy production will be discussed shortly.

1.2 WORLD ENERGY CONSUMPTION AND PRODUCTION

Energy consumption plays a pivotal role in human society, manifesting in various forms including electricity, heat, transportation, manufacturing, and agriculture. The energy use per person on earth varies between countries. The countries with higher GDP per capita tend to use more energy per capita as well. Figure 1.3 shows the map of energy consumption per capita in 2022 for all countries on Earth.

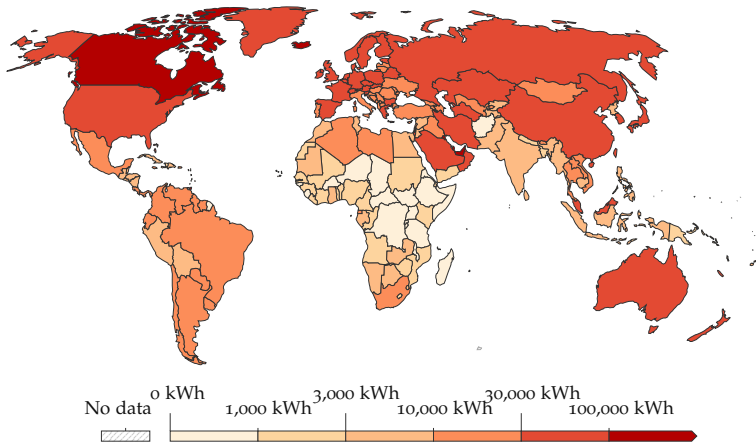


FIGURE 1.3: Energy use per person in 2022, measured in kWh. Energy refers to primary energy using the substitution method. Primary energy includes energy that the end user needs, in the form of electricity, transport and heating, plus inefficiencies and energy that is lost when raw resources are transformed into a usable form. The ‘substitution method’ is used by researchers to correct primary energy consumption for efficiency losses experienced by fossil fuels. It tries to adjust non-fossil energy sources to the inputs that would be needed if it was generated from fossil fuels. It assumes that wind and solar electricity is as inefficient as coal or gas. Figure adapted from [5]

On a global level, energy production has been dominated by fossil fuels that are based on combustion. About 80 % of the energy is produced by the combustion process even in the year 2022. Figure 1.4 shows the world energy production by source from 1995-2022. As seen, in the last 15 years, the contribution of solar and wind has increased dramatically in the energy production mix. However, their contribution has been rather marginal at

the global level. On the other hand, fossil fuels are not sustainable and in fact this will be a challenge in the next few years if we want to aim at producing energy sustainably.

When it comes to global electricity production, coal-based power plants have been dominating the mix, followed by gas and hydropower. Fossil fuel sources account for more than 50% of the global electricity production in 2022. Figure 1.5 shows the world electricity production by source from 1995 to 2022. By grouping countries according to their income level, the mix of electricity production sources also varies. Figure 1.6 shows the production of electricity by source in different income levels. The populations in each group in the year 2022 are about 703 million, 6.678 billion, 2.784 billion, and 1.244 billion people for the low-income, low-middle-income, upper-middle-income, and high-income countries, respectively [6]. Hence, it is remarkable that the high-income countries produce about three times the electricity than the lower-middle income countries, while the population is 5.35 times lower.

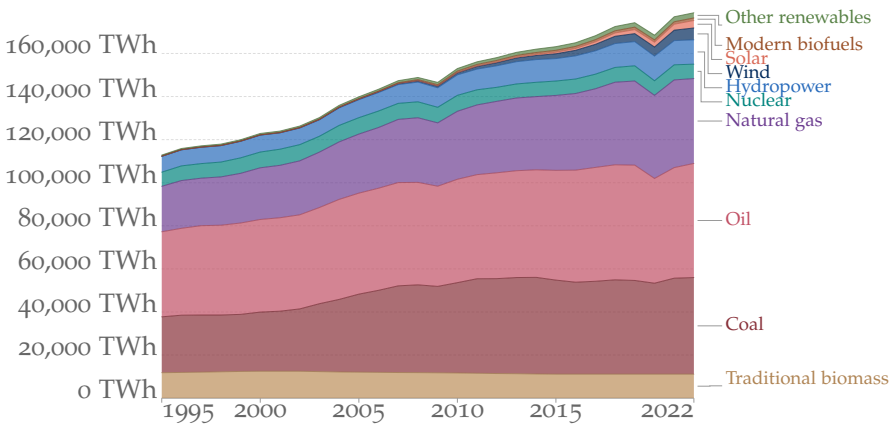


FIGURE 1.4: World energy production by source from 1995-2022, measured in TWh . Figure adapted from [7].

In high-income countries, the production of electricity from coal has been on the decline since 2008. In contrast, the generation of electricity using gas has seen a consistent rise and in 2022, it became the predominant source, accounting for 33% of the total energy produced that year. Additionally, both solar and wind energy have seen considerable increases from 2010 on. However, in the upper-middle-income and lower-middle-income countries, coal has been the main producer of electricity, even until 2022. Gas and coal

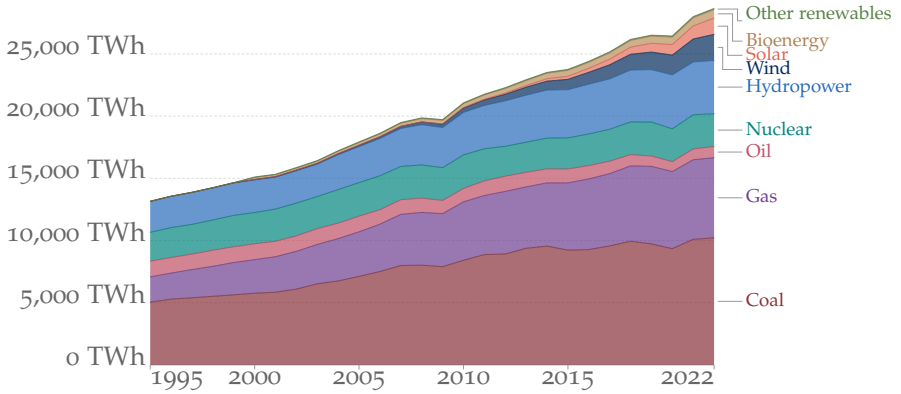


FIGURE 1.5: World electricity production by source from 1995-2022, measured in TWh. Figure adapted from [7].

accounted for 62.37% and 73.73% of total electricity production in countries of upper middle income and lower middle income, respectively. Similarly to high-income countries, solar and wind have seen rapid increases since 2010. In low-income countries, hydropower has been the main electricity production.

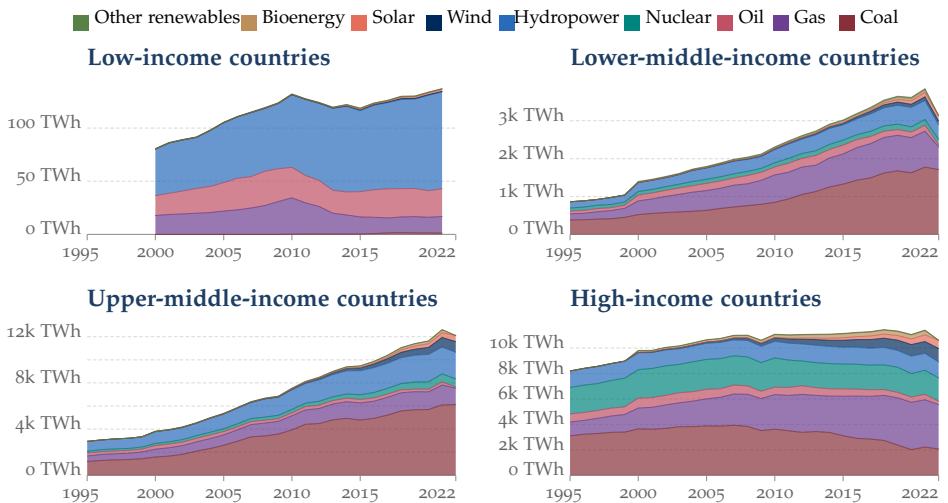


FIGURE 1.6: Electricity production by source in different countries category by income level. Figure adapted from [7].

A recent report by the International Energy Agency (IEA) in 2023 presented different scenarios for future energy and electricity production [8]. In all different scenarios, solar photovoltaic (PV) is predicted to dominate electricity production. However, combustion-based power production is still going to play an important role in all scenarios. It is also noted that in the future batteries and demand response play a critical role in meeting hourly variability, while dispatchable low-emission generators such as fossil fuel capacity with CCUS (Carbon Capture Utilisation and Storage), hydropower, biomass power, nuclear and hydrogen and ammonia-based plants will play a critical role in smoothing variability across seasons. It is predicted that the demand for oil and natural gas in developing countries such as China, India, Indonesia, southeast Asian countries, and African countries will remain significant. Furthermore, in one of their scenarios, Japan and Korea will import significant amounts of hydrogen and hydrogen-based fuels for use in the power sector and for direct use in industry.

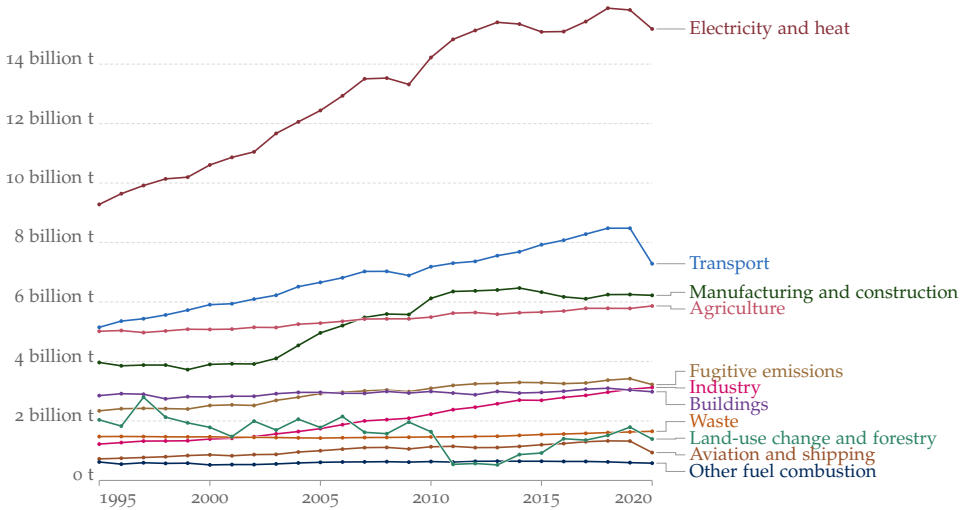


FIGURE 1.7: World greenhouse gas emissions by sector. Emissions are measured in tonnes of carbon dioxide-equivalents. The graph is adapted from [9].

Energy production and consumption emit greenhouse gases that contribute significantly to global warming. Other human activities such as agriculture, and land-use change & forestry also emit greenhouse gases (GHG). Figure 1.7 shows the greenhouse gas emissions by sector, measured in tonnes of CO₂ equivalent. As seen, electricity and heat are the main

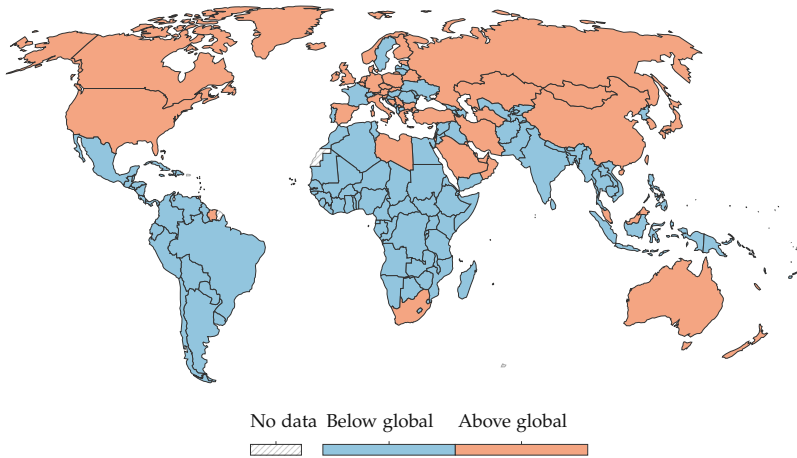


FIGURE 1.8: This map denotes whether a country's average per capita emissions are above or below the value of global per capita emissions, adapted from [5]. This is based on territorial emissions, which do not adjust for trade. Figure adapted from [9].

contributor to GHG emissions, followed by transportation in the second place. Both account for approximately 75% of the global GHG emissions. Therefore, abating CO₂ emissions from both sectors is essential to prevent further global warming. It should be noted that the equivalent emissions per capita also varies between countries. Figure 1.8 presents a geographical representation that distinguishes countries based on their per capita CO₂ emissions, comparing each country's emissions with the global average per capita emissions.

Contributions to global warming from different groupings of countries, classified by income levels, can be analyzed quantitatively. Figure 1.9 shows the impact of fossil fuels & industry and agriculture & land use on global warming for each income group, as well as the cumulative global impact, using 1850 as the baseline year. The calculation of the global mean surface temperature change incorporates emissions of carbon dioxide, methane, and nitrous oxide. The data clearly show that high-income countries are the predominant contributors to global warming, responsible for an increase of approximately 0.64 °C by 2021. Following them, upper-middle-income countries have contributed to a rise of 0.55 °C in global temperatures by

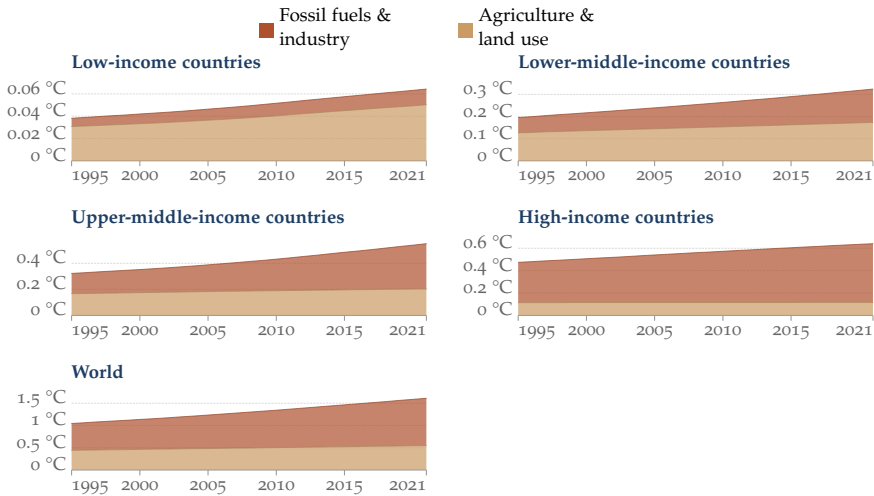


FIGURE 1.9: Global warming contributions from fossil fuels and land use, 1995 to 2021. Change in global mean surface temperature as a result of cumulative emissions by a country or region of three gases – carbon dioxide, methane, and nitrous oxide. The reference year is 1850. Figure adapted from [9].

2021. At the global level, the earth's temperature has increased by 1.6 °C since 1850.

To address climate change, the Paris Agreement convened in 2015 with a primary goal to limit global warming to below 1.5°C by the century's end. Peters et al. [10] emphasized the need for a unified approach to monitor progress, spanning various levels of detail and timeframes. They categorized key indicators into five layers, with the first layer encompassing total global or country-level CO₂ emissions. The second layer includes indicators like CO₂ emissions per energy unit, further dissected in the third layer into carbon intensity of fossil fuels and their share in the energy mix. They suggested that CO₂ emissions reduction could be achieved by transitioning from coal to gas, implementing carbon capture and storage (CCS), or increasing renewable energy use.

The switch from coal to gas could reduce CO₂ emissions, as well as NO_x, SO₂ and particulate matter (PM_{2.5}) [11]. As noted in the report of International Energy Agency (IEA) in 2019 [11], the combustion of natural gas emits 40% less CO₂ compared to coal for the same energy unit produced. The benefit of natural gas over other types of fuel is further reinforced when considering the emissions of particulate matter, sulfur oxides, and nitrogen

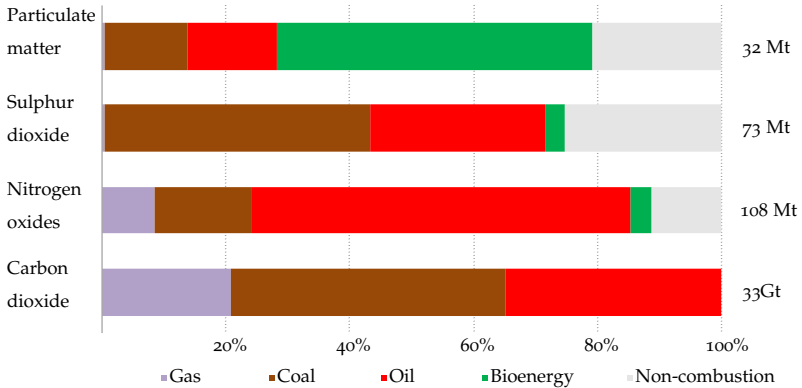


FIGURE 1.10: Share of fuel sources in pollutant emissions measured in metric ton (Mt). Non-combustion emissions are process emissions in industry and non-exhaust emissions in transport. Figure adapted from [11].

oxides. Figure 1.10 shows the proportion of different fuel sources in the emission of all the aforementioned emissions. It is evident that natural gas combustion releases significantly lower amounts of $PM_{2.5}$ and SO_2 .

Increasing the proportion of renewable sources, such as solar and wind, for electricity generation poses many challenges due to their intermittency and variability [12]. These sources require advanced strategies to balance the supply and demand in the electric grid. Owing to its high load flexibility and low emissions, combined cycle gas turbine power plants are a suitable candidate to fulfill the role of load balancer [13]. Furthermore, excess energy production from renewable sources could be stored in a form of hydrogen by electrolysis [14, 15]. Hydrogen produced in this way is termed green hydrogen. Hydrogen storage with up to 2 weeks of discharge duration is predicted to be cost-effective in future power systems [16]. The stored hydrogen could then be utilized as a fuel for gas turbines. The concept of power-to-hydrogen-to-power has received a lot of attentions. For example, in 2020, the HYFLEXPOWER (HYdrogen as a FLEXible energy storage for a fully renewable European POWER system) project received funding from the European Research Council. The goal of the project was to demonstrate a fully integrated Power-to-H₂-to-Power industrial-scale installation in a real-world power plant application with 12 MW electricity [17]. Skordoulias et al [18] investigated the techno-economic analysis of the “power to hydrogen to combined heat and power systems” (PtH₂tCHP). Their study showed that with the expected decrease in the capital cost of the electrolysis unit and the

high utilization rate of the electrolysis unit, the levelized cost of hydrogen production could drop to 3 €/ kg. Furthermore, with the expected increase in carbon cost in the coming years, the production of renewable electricity through PtH₂tCHP could be more economically viable and cheaper than the combustion of 100% natural gas in 2030. Thus, gas turbines are expected to remain a vital component of our energy infrastructure in the foreseeable future, balancing the integration of renewable energy sources.

The GT36 gas turbine, featuring a constant pressure sequential combustion (CPSC) design, can efficiently burn fuel with a high hydrogen blend [19]. Additionally, it offers a wide operating load range [20], while maintaining low emissions and high efficiency. By examining the CPSC configuration at a laboratory scale, this thesis aims to offer a solution to control the thermoacoustics of the combustor to further enhance the operational range.

1.3 SEQUENTIAL COMBUSTOR

Brown Boveri Company (BBC) installed the first 10 MW gas turbine unit for power generation at the Filaret power plant, Bucharest, Romania [3]. The photograph of the gas turbine engine and its schematic diagram are shown in Figure. 1.11. There are two sets of compressors, turbines, and combustors in the setup, with one set operating at high pressure and the other under low pressure. The maximum turbine inlet temperatures were about 566°C and 573°C, which were below the limit of the materials at that time (600 °C). The plant had a higher efficiency compared to the first gas turbine in Neuchatel, the corrected coupling efficiency during the acceptance tests in Baden 1946 was 23.72 percent [3].

1.3.1 GT24/GT26 Gas Turbine

The next milestone took place in the mid-1990s when the GT24/GT26 gas turbine engine was introduced and marketed as "sequential combustion" concept. At that time, the BBC company had been replaced by the ABB/Alstom company. The GT24/GT26 was created in response to the trends in the power market that were moving to higher output & efficiency, substantial NO_x reductions, and operational flexibility [3]. GT24 and GT26 were designated for 60 Hz and 50 Hz application, respectively. Both series operates with an efficiency of 38.2% in the simple cycle mode and 58.5% in the combined cycle mode [21]. Both are equipped with 22 stages of

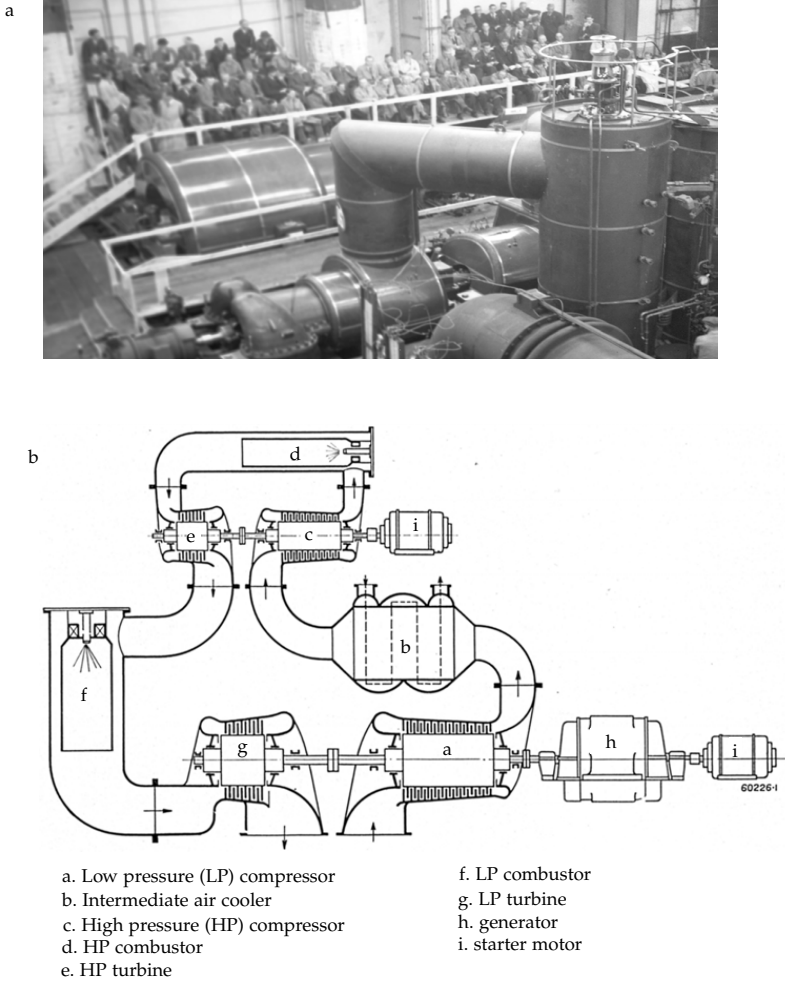


FIGURE 1.11: Photograph a) and schematic diagram b) of the first BBC's 10 MW power generating unit with sequential reheating at Bucharest, Romania. Images taken from [3]

compressor, resulting in a pressure ratio of 30, and 5 stages of turbines. The turbine exhaust temperature is 610°C , which is ideal for the combined cycle (gas and steam) configuration [21]. Images of the welded rotor and the schematic diagram of GT24/GT26 are shown in Figure. 1.12.

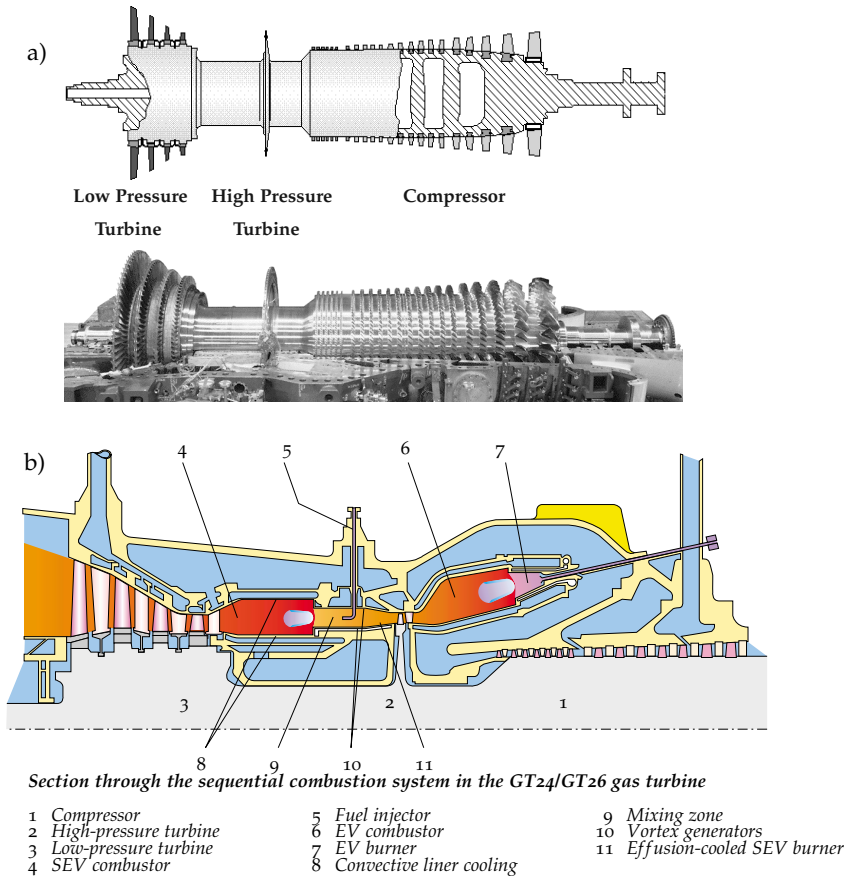


FIGURE 1.12: Photograph of the welded rotor a) and schematic diagram b) of the GT24/GT26. Images in a) are adapted from [3], the schematic diagram in b) is adapted from [21]

The combustor is made up of two sequentially staged EV (EnVironemntal) combustor with a high pressure turbine in between. The EV combustor design was first presented in [22], where the flameholding mechanism is based on then vortex breakdown generated by a swirler. The sequential EV combustor (SEV) relies on the self-ignition effect of the fuel and the hot mixture from the first stage EV combustor.

The compressed air coming from the compressor is fed through the first EV combustor which is supplied with 60% of the total amount of fuel (at

full load condition) [21]. The combustion gas then expands through the high pressure turbine and the pressure drops from 30 to approximately 15 bar. The hot air at 1000°C then goes to the SEV combustor and remaining fuel and the bled air from the compressor are then added to the SEV combustor. The bled air or the dilution air enhances the premixing and also acts as an ignition controller [21]. The temperature of the second combustion products reaches the maximum turbine inlet temperature. As in the EV combustor, the second flame is anchored at the vortex breakdown position, in which the vortices are generated by delta-wing vortex generators placed on the walls of the SEV burner. The final expansion happens within the subsequent 4-stage turbine. The rated NO_x emission was below 25 ppmv with dry fuel gas, and below 42 ppmv for wet oil combustion.

1.3.2 *GT36 Gas Turbine*

The most recent advancement in the commercial sequential combustor setup is the Ansaldo GT36 gas turbine. This development was carried on by Ansaldo Energia after General Electric (GE) acquired Alstom Power in 2014. The GT36's design resembles that of the GT24/GT26, which also uses a sequential combustor configuration. A significant change in GT36 is the elimination of the high-pressure turbine, leading to the introduction of the term CPSC (Constant Pressure Sequential Combustor) [20]. The rated power for GT36 s5 (50 Hz) and GT36 s6 (60 Hz) for combined cycle is 720 MW and 500 MW, with the ISO efficiency of 61.5% and 61.3%, respectively.

The GT36 shares several benefits with the GT26, including high turndown, high reliability, and low emissions. Additionally, it offers improvements in design simplicity and increased flexibility in load handling. The elimination of the high-pressure turbine simplifies the maintenance of the combustor because it requires no rotor extraction for more extensive combustor and turbine access.

Figure 1.13 shows the GT36 gas turbine and its cross-sectional cut. The dilution air mixer is introduced upstream of the sequential burner via a multi-row mixer with specific nozzles designed for uniform inlet profile to the sequential burner. The sequential fuel is injected downstream inside the so-called mixing duct. Similarly to GT26, the front panel of the sequential burner is equipped with Helmholtz resonators for thermoacoustic stabilization [20].

The air exiting compressor is split into two main paths; the first path goes to the first stage premix burner and combustor, the second path

goes to the sequential linear cooling and subsequently to the dilution air mixer. The hot gases from the first-stage combustion products mix well with the downstream dilution air at a temperature typically of around 1000°C . This temperature is termed the mixer exit temperature (MET) and is the control parameter for the combustor, which is a function of load, fuel composition, and dynamics. The sequential fuel is then injected through multiple downstream nozzles equipped with vortex generators to enhance mixing. Subsequently, the sequential flame burns downstream in the sequential combustor, whose length is chosen to minimize residence times to minimize the NO_x emissions through the Zeldovich mechanism.

The CPSC configuration allows for high fuel flexibility. For example, if there is a change in the reactivity of the mixture due to a higher hydrogen content, a lower inlet temperature, or MET, can be achieved by changing the split of the fuels between the first stage and the second stage [19, 20]. When

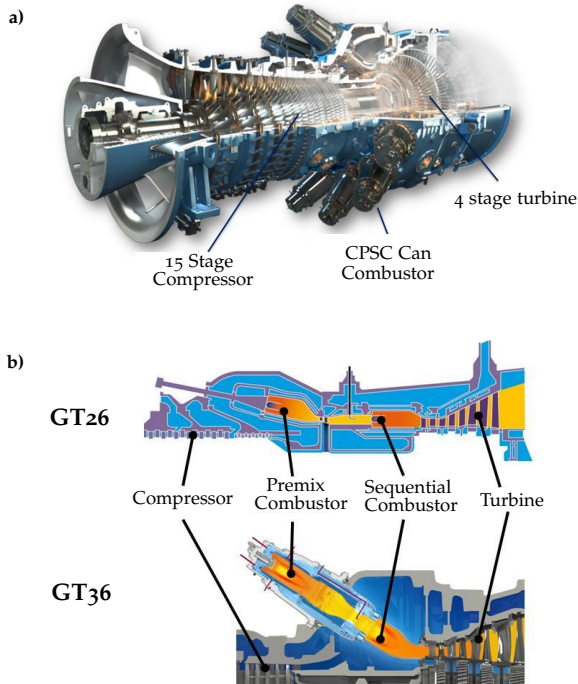


FIGURE 1.13: a). The GT36 H-class gas turbine. b) The evolution from GT26 to GT36. Adapted from [20]

operating in high-load conditions, and therefore, with increased heating of compressor exit air, the air routing is configured so that the first-stage flame burns colder than at the part load to minimize NO_x emissions. A single can high-pressure combustion test campaign was carried out to investigate the capabilities of CPSC to burn high volumetric hydrogen, and it was presented in [19]. It was noted that in the range of 0%-70% (vol.) H_2 , stable operations were possible at full nominal combustor exit temperature by adjusting the MET. However, for a larger amount of H_2 , adjustment was no longer possible because the flame propagation stabilization mechanism would dominate, and hence, a reduction in the equivalence ratio was necessary to be compatible with the burner design. However, NO_x emissions remained low in all test cases, highlighting the remarkable potential to fully decarbonize power generation. It is worth mentioning that Schulz et al. [23] identified through numerical simulations the three combustion regimes of the sequential flame: autoignition, flame propagation, and flame propagation assisted by autoignition. It was shown that variation on the inlet temperature of the sequential combustor, or equivalently, the MET, will result in changes in the flame stabilization mode.

Due to its high level of fuel flexibility, low NO_x emissions, and the ability to burn hydrogen, the CPSC configuration could be relevant in the future market for power generation. However, similar to the conventional single-stage combustor, the operability of the CPSC configuration is still limited by the thermoacoustic instabilities. The description of the thermoacoustic instabilities and its physical mechanism are described in the next section.

1.4 THERMOACOUSTIC INSTABILITIES

Thermoacoustic instabilities result from the constructive interplay between acoustic disturbances in the combustion chamber and the fluctuating heat release from the flame [24, 25, 26]. This interaction typically produces high-amplitude pressure pulsations that can be harmful. These instabilities are not restricted to a single type of application; they can be observed in a range of systems, such as boilers, rocket engines, jet engines, and gas turbines [26, 27]. In particular in gas turbines with premix-type combustor, these instabilities are more likely to occur [28].

The first person to observe the thermoacoustic phenomenon was Dr. Higgins in 1777 [29]. He noted that a hydrogen flame placed inside a tube produced sweet tones that vary according to the geometry of the tube. About 100 years later, Lord Rayleigh gave the explanation of the

phenomenon [30, 31]: *If heat be given to the air at the moment of greatest condensation, or be taken from it at the moment of greatest rarefaction, the vibration will be encouraged. On the other hand, if heat will be given at the moment of greatest rarefaction or abstracted at the moment of greatest condensation, vibration will be discouraged.* These sentences are widely known as the “Rayleigh Criterion”.

A prime illustration of the destructive impacts of uncontrolled thermoacoustic instabilities can be seen in the development of the F1 rocket engine. This issue persistently caused the rocket engine combustor to fail, over 2000 full-scale tests were done to eventually devise an optimal injector and baffle design to eliminate these instabilities [32]. Notably, the predominant instability mode was identified as the first tangential spinning mode, approximately at 500 Hz.

The examples of engine components damaged by these instabilities are shown in Figure 1.14. Such occurrences can significantly compromise the safety and reliability of engines. In the case of gas turbines, this would result in a need for extensive overhauls, leading to costly maintenance and operational downtime, ultimately causing a loss of revenue due to halted electricity or energy production.

The diagram in Figure 1.15 provides a simplified overview of the key thermoacoustic interactions and the associated feedback mechanisms. The process begins with modulation of the fuel and air flow, which leads to changes in the equivalence ratio and coherent mass flow fluctuations. These alterations contribute to coherent fluctuations in the rate of reactants consumption. In addition, turbulence introduces stochastic fluctuations in the equivalence ratio and mass flow, which in turn causes stochastic fluctu-

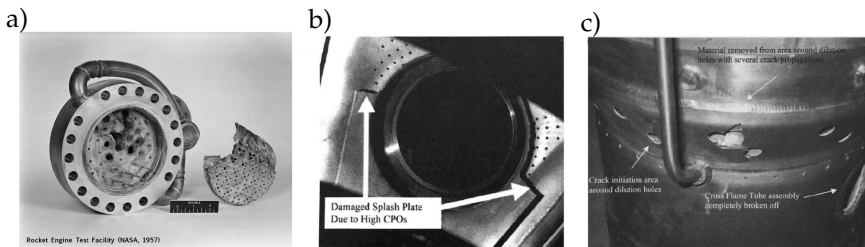


FIGURE 1.14: a). Rocket engine destroyed by thermoacoustic instability during the early years of the US rocket program, adapted from [33]. b) Borescope of damaged combustion chamber due to thermoacoustic instabilities and c) photograph of damaged combustion chamber assembly, adapted from [34]

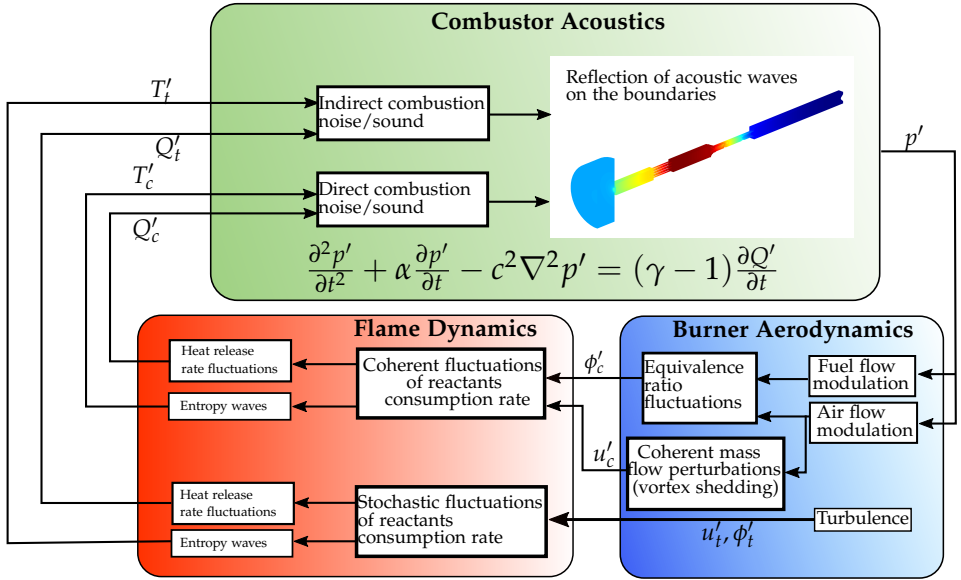


FIGURE 1.15: Diagram of thermoacoustic interaction in a combustion chamber. The picture in the first row is the Helmholtz solver solution of the sequential combustor configuration at CAPS Laboratory.

ations in the consumption rate of reactants. Consequently, this results in fluctuations in the heat release rate and the generation of entropy waves. The fluctuation in heat release acts as a source term in the wave equation, while the entropy waves have the potential to produce sound at the outlet boundaries, effectively altering the outlet reflection coefficient. These reflected waves then travel back towards the burner, completing the feedback loop.

The aforementioned ‘‘Rayleigh Criterion’’ could be mathematically derived by writing the acoustic energy balance. For simplicity, the contribution of the mean flow is neglected, and the flow is assumed to be isentropic. The energy balance between the acoustic energy flux \vec{I} , the acoustic energy of the system E , and the source Φ can be written as follows [35, 36, 37]:

$$\frac{\partial E}{\partial t} + \nabla \cdot \vec{I} = \Phi \quad (1.1)$$

$$\frac{\partial}{\partial t} \left(\frac{p'^2}{2\rho_0 c_0^2} + \frac{\rho_0}{2} \vec{u}' \cdot \vec{u}' \right) + \nabla \cdot (p' \vec{u}') = \frac{\gamma - 1}{\gamma p_0} p' q', \quad (1.2)$$

where p' , \vec{u}' , and q' are the acoustic pressure, acoustic velocity fluctuations, and heat release rate fluctuations, respectively. The mean density, the speed of sound, the mean pressure, and the specific heat capacity are denoted by ρ_0 , c_0 , p_0 , and γ , respectively. By integrating over the volume and applying the time averaging operator, $\langle \rangle$, Eq 1.2 can be written as follows:

$$\frac{\partial}{\partial t} \int_V \langle E \rangle dV = \int_V \frac{\gamma - 1}{\gamma p_0} \langle p' q' \rangle dV - \int_S \langle p' \vec{u}' \rangle dS. \quad (1.3)$$

The term on the left-hand side (LHS) denotes the rate of change of the total acoustic energy in the domain. The first term on the right-hand side (RHS) is the source term that depends on the phasing between the pressure fluctuations and the heat release rate fluctuations. When the phase is between -90° and 90° the term will be positive. The second term on the RHS denotes the flux or losses across the boundaries. When the first term in the RHS is larger than the second, there will be an increase in acoustic energy in the system and thermoacoustic instability could be established. Note that the energy will not increase to infinity as there will be some saturation mechanism taking place in the real system.

If the pressure field is the quantity of interest, the acoustic wave equation can be derived from the conservation of mass and momentum, and by noting that heat release rate fluctuation is a monopolar source, the wave equation is expressed as:

$$\frac{\partial^2 p'}{\partial t^2} + \alpha \frac{\partial p'}{\partial t} - c_0^2 \nabla^2 p' = (\gamma - 1) \frac{\partial Q'}{\partial t}, \quad (1.4)$$

where the second term on the LHS is the acoustic loss. The pressure field can be projected to orthogonal basis Ψ and write as:

$$p(\mathbf{x}, t) = \sum_{i=1}^{\infty} \psi_i(\mathbf{x}) \eta_i(t), \quad (1.5)$$

where $\psi_i(\mathbf{x})$ is the i^{th} eigenmodes of the system, and $\eta_i(t)$ is the corresponding modal amplitude. Note that the eigenmode ψ_i satisfies the following Helmholtz equation:

$$\nabla^2 \psi_i(\mathbf{x}) + \left(\frac{\omega_i^2}{c_0^2} \right) \psi_i(\mathbf{x}) = 0, \quad (1.6)$$

If one acoustic mode is dominating, a single mode projection can be employed: $p(\mathbf{x}, t) = \psi(\mathbf{x})\eta(t)$. Using the Laplace transform and considering Eq 1.4, the equation for the modal amplitude $\hat{\eta}(s)$ can be written as [38]:

$$\left(s^2 + \alpha s + \omega^2 \right) \hat{\eta} = s\hat{q}, \quad (1.7)$$

where \hat{q} is the projection of the flame heat release rate fluctuation to the mode ψ :

$$\hat{q} = \frac{\gamma - 1}{V\Lambda} \int_V \hat{Q}(s, x) \psi(x) dV, \quad (1.8)$$

where Λ is the mode normalization coefficient. The heat release rate fluctuations can be written as the sum of coherent and stochastic part: $\hat{q} = \hat{q}_c + \hat{q}_t$. The stochastic term is attributed to the turbulence in the practical combustor. The coherent part results from the interaction with the acoustic field. The linear coupling between those two is referred to as flame transfer function (FTF). In many cases, the relationship between the flame heat release rate and the acoustic amplitude (at a specific frequency) exhibits a sigmoid-like saturation and hence it is possible to approximate it with a cubic polynomial [38, 39, 40, 41]:

$$\hat{q}_c = \beta \hat{\eta} + \frac{\kappa}{3} \hat{\eta}^3, \quad (1.9)$$

where, β is the real part of the flame transfer function at the frequency of interest, and κ is the corresponding nonlinear coefficient. The imaginary part of β only affects the frequency and not the stability [38], hence it is assumed in this explanation that β is a purely real quantity. Combining equation 1.9 and equation 1.4, and going back to the time domain results in:

$$\ddot{\eta} + \omega^2 \eta = \dot{\eta} \left(\beta - \alpha - \kappa \eta^2 \right) + \zeta, \quad (1.10)$$

where ζ is the stochastic component of the heat release rate due to turbulence. The term $\beta - \alpha = 2\nu$ is the growth rate of the oscillations, which, for a positive value, causes the acoustic modal amplitude to grow and then eventually becomes saturated by the nonlinear term $\kappa \eta^2$. Equation 1.4 describes a van der Pol oscillator that is forced stochastically.

The growth rate ν , the saturation coefficient κ , and the noise intensity of ζ can be identified by analyzing the statistics of the envelope of η from

experiments [38, 41]. The information on the growth rate can then be used to develop a passive damper solution, optimize the parameters of an active control algorithm, or validate a thermoacoustic network model. It should be mentioned that a thermoacoustic network model has the advantage of being able to predict changes in thermoacoustic stability depending on some variation in the relevant parameters [42, 43, 44, 45].

In a sequential combustor, the first and second-stage flames communicate via the acoustic field and entropy waves [23, 46]. In low Mach number combustion, entropy fluctuations are proportional to temperature fluctuations [47, 48]. The heat release rate responds to upstream temperature fluctuations, due to changes in the ignition delay time [23, 46]. Despite flame stabilization in the propagation regime, nonlinear responses in the flame's heat release rate can occur due to autoignition kernels in the mixing channel, depending on the mean inlet temperature and temperature forcing amplitude [23]. When convected autoignition kernels reach the flame front, they promote a sudden increase in the heat release rate. The dynamics of the sequential flame can be characterized by a 3×3 flame transfer matrix relating upstream and downstream fluctuations in acoustic pressure, velocity, and temperature [49]. Notably, the study in [49] focuses on a sequential flame that is fully supported by autoignition. Currently, studies on the flame transfer matrix of a sequential flame are heavily based on numerical simulations, and no experimental investigations have been performed to date. This could be attributed to difficulties in measuring the temperature fluctuations. This thesis also addresses this issue, and later, in Chapter 4, a laser absorption spectroscopy-based temperature sensor for combustion applications will be outlined.

Thermoacoustic instabilities not only pose a threat to the structural integrity of the combustion chamber, but are also often associated with an increase in NO_x emissions [50]. Thermoacoustic instabilities can be controlled using passive and active control strategies [50]. Passive control strategies are more widely applied in practical combustors due to their simplicity. There are two categories in passive control strategies: increasing the acoustic losses and reducing the acoustic driving of the combustion process [51]. Examples of the application belonging to the first category are Quarter-wave and Helmholtz resonators. Helmholtz resonators have been widely applied in many practical combustors [20, 52, 53]. The second category includes modification of the fuel injection staging location and modification of burner geometry.

The application of active control strategies in the real practical combustors is rather limited due to the lack of fast and robust actuators. Moreover, it is crucial to ensure that the actuator's power consumption is kept minimal to avoid compromising the efficiency of the gas turbine. Another significant challenge is the development of a robust controller capable of adapting to dynamic changes in operational conditions [50]. Plasma discharges, specifically those generated by nanosecond repetitively pulsed discharges (NRPDs), have shown promising results in stabilizing the thermoacoustics of conventional single-stage combustors [54, 55]. This thesis explores the use of NRPDs in a laboratory-scale sequential combustor for thermoacoustic control. A brief overview of plasma-assisted combustion is provided in the next section.

1.5 PLASMA-ASSISTED COMBUSTION

Plasma is the fourth state of matter which is characterized by a collection of neutral and charged particles which are electrically neutral on average. In a laboratory, plasma could be generated by example applying a high-voltage drop across two electrodes with air in between. When the voltage is sufficiently high, that is, higher than the voltage required to promote a sufficiently intensive electron avalanche, a sharp increase in current would occur [56]. The process is typically accompanied by light emission, which is generated by the excitation of air molecules. For example, light emission at a wavelengths around 337 nm and around 357 nm are caused by the transition of excited nitrogen from the $N_2(C)$ to the $N_2(B)$ state and are often used to measure the gas temperature [57, 58]. There exist two types of plasma: **thermal** and **non-thermal** plasma [56]. In the former, the rotational (T_r), vibrational (T_v) and electron temperatures (T_e) of the particles are in equilibrium equal to each other. In the latter case, all temperatures are not in equilibrium and typically the relation among them is $T_e > T_v > T_r \approx T_i \approx T_o$, where T_i and T_o are the temperature of ions and heavy particles, respectively.

Thermal plasma for combustion applications has been applied since more than one hundred years ago in internal combustion (IC) engines and spark ignition systems [59]. The nonthermal plasma has a higher electron temperature (1-100 eV) compared to the thermal plasma, and has attracted a lot of interest in combustion applications [60]. Some examples of non-thermal plasma are nanosecond repetitively pulsed discharges (NRPD), dielectric barrier discharges (DBD), and microwave plasma.

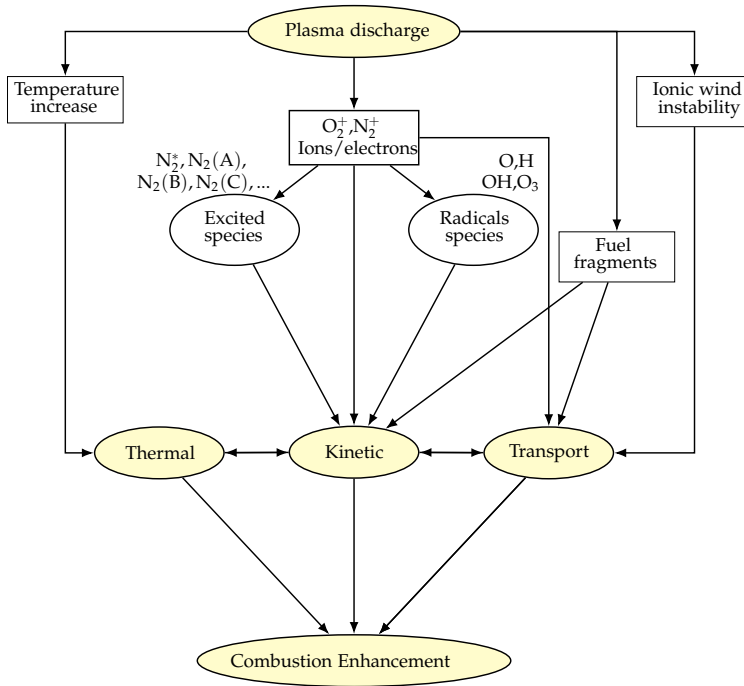


FIGURE 1.16: Diagram of the three major pathways of plasma and combustion interaction. Adapted from [60].

NRPDs refer to the type of plasma generation mechanism in which short (10 – 100 ns) high-voltage pulses are applied at a high repetition rate in the range of 1 – 100 kHz. Nanosecond discharges can produce a very strong reduced electric field that allows energy transfer for the electronic excitation and dissociation of gas molecules [60]. Therefore, nanosecond discharges have attracted a lot of interest for combustion applications. One of the typical uses of nanosecond discharges is to improve the lean flammability limit of a premixed flame; for example, Barbosa et al. presented the effect of NRPD on the extension of the lean flammability limit of a swirled lean premixed flame [61]. The next example is the use of NRPD to control the thermoacoustics of a turbulent swirled flame, as demonstrated in [54, 55, 62]. In these studies, it was shown that NRPD with a mean plasma power of approximately 1% the thermal power of the flame could reduce the acoustic pulsation.

There are three main pathways for plasma to interact and affect combustion: the kinetic, thermal, and transport pathways [60]. Figure 1.16 shows the diagram of the three major pathways. In the thermal pathway, plasma increases temperature and thereby accelerates the chemical reaction between the fuel and the oxidizer. In atmospheric pressure preheated air to 1000 K, nonthermal plasma discharges can result in gas heating rates between 30 and 50 K/ns. The rapid increase in temperature phenomenon is known as fast gas heating (FGH) [63]. It results from the relaxation of electronically excited states of atoms and molecules. However, note that the rate of FGH depends on the discharge parameters [57].

In kinetic pathways, the generated high-energy electrons and ions produce active radicals (e.g. O, OH, H) through direct electron impact dissociation, ion impact and recombination dissociation (e.g., O_2^+ , N_2^+), and collisional dissociations of reactants with electronically and vibrationally excited molecules. Understanding plasma kinetics is a complex subject, with numerous studies undertaken to gain both quantitative and qualitative insights into its processes.

In the transport pathways, plasma can breakdown the fuel into simpler molecules and hence changing the diffusivity and thus affecting the combustion processes. Plasma also changes the local flow velocity through ionic wind and hydrodynamic instabilities and hence affecting the flow mixing.

In weakly ionized plasma, that is, where the electron number density, n_e , is much smaller than the gas number density N , the reduced electric field, E/N , and n_e are the important parameters [64]. The reduced electric field is a function of the gas density, the applied voltage and the geometry of the discharge cell [59]. The value of E/N governs the electron temperature and electron-impact reaction rates, and it controls how the electron energy is dissipated to different excitation channels. Figure 1.17 shows the fraction of electron energy dissipated in different channels as a function of E/N for H_2 -Air mixture in stoichiometric [59, 63]. At low $E/N \approx 10 \text{ Td}$, most of the electron energy goes to the vibrational excitation of nitrogen and hydrogen. At higher E/N values which is the relevant range of interest in this thesis, in the range of 100 – 300 Td, the electronic excitation of nitrogen dominates. The excited particles are then quenched during the relaxation processes and result in the fast heating of the gas, which contributes to the thermal pathways in Figure 1.16. In nanosecond discharges, during and after the pulse, electronically excited nitrogen reacts with the molecular oxygen in exothermic reactions. The generation of the electronically excited

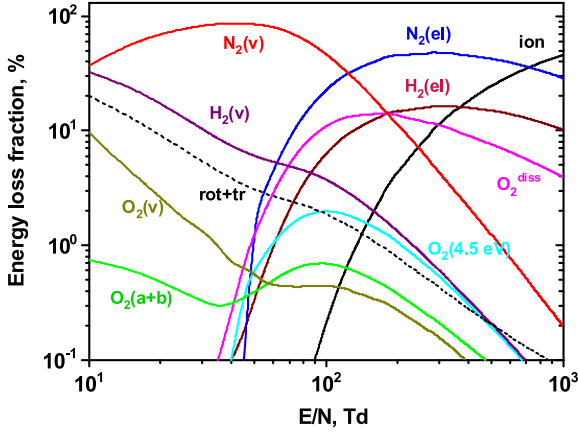
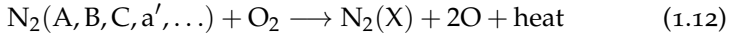
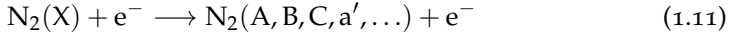


FIGURE 1.17: Computed fractional energy dissipated by electrons into the different molecular degrees of freedom in H_2 -Air mixture as a function of, reduced electric field, E/N in Td (V/cm^2) [59, 63]. rot+tr: rotational and translational excitation, v: vibrational excitation, el: electronic excitation, a+b: sum of singlet electronic excitation, ion: ionisation, dis: dissociation.

nitrogen and its reaction with oxygen molecules could be summarized in the following two-step mechanism [64]:



Equation 1.11 describes the excitation of nitrogen molecules to the electronically excited states, and equation 1.12 comprises of different quenching reactions of electronically excited states to ground states by the oxygen molecules which in turn produce oxygen atom and heat. The mechanism was first proposed and detailed in [65].

As mentioned previously, NRPDs have been employed to control the thermoacoustics of a turbulent combustor in single-stage combustors. This thesis explores the application of NRPDs in controlling thermoacoustics within a sequential combustor. The high-voltage electrodes are strategically positioned within the mixing channel of the sequential combustor, where gas temperatures exceed 1000 K. This placement is crucial because it enables plasma breakdown at reduced voltages, owing to the lower gas density at these temperatures. Consequently, the electrical energy required to initiate

the breakdown is less than that that would be necessary if the discharge were to happen at ambient temperatures.

1.6 SCOPE AND STRUCTURE OF THE THESIS

The central focus of this thesis is to apply nanosecond repetitively pulsed discharges (NRPDs) to stabilize the thermoacoustics of a lab-scale sequential combustor at atmospheric and elevated pressures of up to 6 bar. A novel adaptive control approach based on a safe Bayesian optimization algorithm is developed to optimize the control parameter of NRPDs and the combustor. Furthermore, a fast and robust temperature sensor based on tuneable diode laser absorption spectroscopy with wavelength modulation spectroscopy (TDLAS-WMS). This sensor is designed to support future studies aimed at understanding the dynamic behavior of sequential flames which are typically sensitive to inlet temperature fluctuations.

The main objectives of this thesis are summarized as follows:

- Introduce the ultra-low-power NRPD as an actuator to stabilize a sequential combustor under stationary operation at atmospheric pressure.
- Develop a safe optimization algorithm to optimize the control parameters of NRPD and the sequential combustor.
- To create a fast and robust temperature probe sensor, laying the groundwork for future research into entropy waves within the sequential combustor.
- Demonstrate the capability and effectiveness of NRPD in stabilizing the thermoacoustics of a transiently operated sequential combustor at high pressure.

Chapters 2 through 5 sequentially tackle the stated objectives. The following paragraphs provide brief overview of each chapter.

Chapter 2: Thermoacoustic stabilization of a sequential combustor with ultra-low-power Nanosecond Repetitively Pulsed Discharges. This chapter demonstrates the effectiveness of NRPD to stabilize the thermoacoustics of an atmospheric sequential combustor. The sequential flame was fueled with a mixture of hydrogen and natural gas. A parametric study of plasma repetition frequency (PRF) and generator voltage was performed. The experimental findings included measurements of NO emissions, high-speed

OH^* chemiluminescence imaging, plasma energy deposition, and acoustic pressure pulsations. It was observed that with a plasma power amounting to just 1.5×10^{-3} percent of the flame's thermal power, the NRPDs effectively suppressed thermoacoustic instabilities with negligible additional NO emissions. The insights gained from this chapter are pivotal for developing the adaptive control algorithm discussed in chapter 3 and for the high pressure experiments presented in chapter 5.

Chapter 3: BOATS: Bayesian Optimization for Active Control of ThermoacousticS. This chapter focuses on the development of safe Bayesian optimization algorithms to optimize control parameters safely. Three different algorithms are extensively presented in detail and demonstrated through numerical and experimental studies. The algorithms were evaluated first in a simpler numerical and experimental setup with only a single-stage combustor equipped with loudspeaker actuation. Subsequently, the same algorithm was employed in a sequential combustor with NRPDs actuation. With the help of the algorithms, it was possible to find regions in the control parameter space that were thermoacoustically unstable without plasma control but became stable with plasma and produced low NO emissions.

Chapter 4: Entropy Transfer Function Measurement with Tuneable Diode Laser Absorption Spectroscopy. This chapter describes in detail the tuneable diode laser absorption spectroscopy with wavelength modulation spectroscopy (TDLAS-WMS) method. The method was employed to measure coherent temperature fluctuations of a technically premixed turbulent swirled flame at three different operating conditions. The resulting entropy transfer function (ETF) and flame transfer function (FTF). This chapter establishes a fundamental groundwork for subsequent research in the experimental investigation of entropic response of sequential flame.

Chapter 5: Plasma Assisted Thermoacoustic Stabilization of a Transiently Operated Sequential Combustor at High Pressure. This chapter focuses on the evaluation of the actuation performance of NRPDs under transient operation at high pressure. The experiments are carried out in the newly built high-pressure setup at CAPS lab. Two different transient scenarios are considered: first, the combustor is operated at a pressure of 5 bar and the tunable outlet orifice area is progressively increased. This results in the change of outlet impedance and enhances the acoustic pulsations when the system is uncontrolled. Second, the thermal power of the sequential combustor is ramped-up from 273 to 341 kW, the combustor pressure

simultaneously increases from 4 to 5 bar. In addition, the performance of the actuator is evaluated in stationary conditions under high pressure.

THERMOACOUSTIC STABILIZATION OF A SEQUENTIAL COMBUSTOR WITH ULTRA-LOW-POWER NANOSECOND REPETITIVELY PULSED DISCHARGES.

It doesn't matter how beautiful your theory is, it doesn't matter how smart you are. If it doesn't agree with experiment, it's wrong.

— Richard Feynmann

In this chapter, the first demonstration of nanosecond repetitively pulsed discharges (NRPDs) to stabilize an atmospheric sequential combustor is presented. Parametric studies on the NRPDs parameter such as generator voltage and pulse repetition frequency (PRF) is conducted to evaluate their effect on the NO emissions and acoustic pulsations. It is found that NRPDs with a mean plasma power of 1.5×10^{-3} percent of the thermal power of the flame can adequately stabilize the thermoacoustics. However, Depending on the combination of the parameters, thermoacoustic instabilities could be enhanced. Changes in the flame structure of the sequential flame are studied by means of high-speed OH chemiluminescence imaging. This chapter introduces novel findings that establish a basis for future research.*

2.1 INTRODUCTION

One major technological breakthrough of the recent past in gas turbine technologies is the constant pressure sequential combustor (CPSC) [20, 66]. It significantly improves the operational range with very low pollutant emissions, and the fuel flexibility, which is the ability to be supplied with mixtures of hydrogen and natural gas, as well as non-conventional fuels derived from waste processes or biomass gasification [67]. Notably, the combustion of pure H₂ in an academic CPSC configuration has recently been investigated in [68]. In CPSC configurations, the hot products from the first-stage combustor are diluted with air bypassing the first-stage before the sequential fuel is injected. This combustor architecture reduces the temperature of the vitiated air flow at the inlet of the sequential stage to prevent too fast autoignition of the sequential fuel in poorly mixed conditions. Ensuring in this way a sufficient mixing time of the globally lean

mixture of gas and vitiated air, the exothermal reactions of the autoignition process in the sequential stage occur under well-mixed conditions, and therefore the NO_x emissions can be drastically reduced.

Similarly to a traditional combustor, CPSC combustors are also prone to thermoacoustic instabilities [69, 70, 71, 72]. These instabilities can lead to high amplitude acoustic pressure oscillations which can lead to vibration-induced structural damage and possibly flame flashback [33]. Therefore, the development of technologies to control instabilities is essential for the safety and operability of gas turbines.

Passive damping strategies have been widely studied and applied in real combustors. For example, the nonlinear behavior of Helmholtz resonators mounted on the walls of combustion chambers has been investigated in a recent study in order to draw design guidelines to avoid failures of their damping effectiveness [73]. Furthermore, dampers based of interconnected cavities with broadband acoustic absorption capabilities were successfully implemented in large modern gas turbines [53, 74]. However, the design of these passive dampers is still challenging for the following two reasons: First, it requires costly engine testing to obtain a relatively precise prior knowledge of the difficult-to-predict thermoacoustic instabilities, in order to tune their geometry for effective reduction of the acoustic amplitude. Second, for a given volume constraint for their implementation, there is always a trade-off to find between their broadbandness for addressing multiple instability frequencies and their effectiveness at a given frequency.

In contrast, active control strategies can adapt to the operating conditions of the system but, so far, their implementation in real engines has been hindered by the harsh thermodynamic and thermochemical conditions and by the lack of cost-effective and mechanically robust actuation solutions. The big challenge of implementing active control strategies is to find appropriate actuators [75, 76]. For example, the use of loudspeakers to stabilize an unstable combustor by tailoring its acoustic boundary conditions was successfully achieved in an academic configuration operated at atmospheric pressure [77] but could not be applied in a real engine. Another active control strategy, based on the fast modulation of the fuel mass flow has been successfully developed about thirty years ago for liquid spray [78] and natural gas [79]. The latter technology has even been validated in heavy duty gas turbines and was commercialised. However, effective modulation of the pilot gas mass flow cannot be achieved beyond 500 Hz, which prevents one from addressing the problem of high-frequency instabilities with

the corresponding valves. Furthermore, such modulation of the fuel mass flow could negatively impact the pollutant emissions.

In this context, the search for alternative actuators for gas turbine combustors, with high control authority, low power consumption, and minimal additional emissions, is highly relevant to increase the fuel and operational flexibility of future gas turbines. This chapter focuses on ultra-low-power plasma actuation, which has never been implemented in industrial systems so far, and aims to show that it is a very promising strategy for suppressing thermoacoustic instabilities in sequential combustors without increasing NO_x emissions.

Owing to its high influence to the kinetics of the reactive mixture, several studies have characterized the effect of nanosecond repetitively pulsed discharges (NRPD) on the heat release rate oscillations of acoustically-forced flames. For instance, Lacoste et al. [62] have studied this effect in a single stage swirled stabilized combustor. It was shown that NRPD affects significantly the gain and phase of the flame transfer function (FTF) and thereby, might influence the thermoacoustic stability of the combustor. In [80], it was shown with a laminar flame that strong heat release rate modulation can be induced by periodic series of constant voltage NRPD. The forcing mechanism was mainly attributed to the increase of local burning velocity close to the plasma region. In a similar set-up to the one in [62], Moeck et al. [54] have successfully demonstrated the applicability of nanosecond plasma discharges to stabilize a linearly unstable combustor with active feedback control. By using the extended kalman filter (EKF), the instantaneous phase of the acoustic pulsation was estimated and then fed to the gate signal for the actuation of the plasma generator. The plasma power required to stabilize the combustor was at around percent of the flame thermal power. Furthermore, Kim et al. [81] have demonstrated the capability of NRPD to stabilize a combustor under realistic low-power conditions of aeroengine combustors.

Nanosecond plasma discharges in pin-to-pin configuration have shown high potential for second-stage flame stabilization in constant-pressure sequential combustors, as the hot reactive mixture in the sequential burner already undergoes radicals-producing chemical reactions that precede auto-ignition. Xiong et al. [82] demonstrated that NRPD could shorten significantly the auto-ignition time of a CH_4 sequential flame with low electric power and NO emissions. In a more compact laboratory-scale sequential combustor, Shcherbanev et al. [57] demonstrated the effectiveness of plasma discharges in igniting very lean mixtures of hydrogen and natural gas

blending, thereby enabling a continuous ignition of the sequential flame. One significant advantage of the NRPD actuation is that the electrode system implementation does not require a drastic modification of the combustor geometry and could also be considered for retrofitting existing systems.

Another advantage of NRPD is their fast response time, which enables high-frequency actuation without moving parts that are usually causing reliability and durability issues in mechanical actuators. Indeed, non-equilibrium plasma actuation can quickly influence flames, improving their stability and extending their lean flammability limit [55, 83, 84].

Finally, the mean NRPD power is known to be small compared to the thermal power of the flame [55, 62, 85]. It should be noted that the mean NRPD power reported in literature pertains only to the electrical energy that gets transferred to the system, without accounting for the electrical energy necessary for the high-voltage generator. However, if we consider an optimistic scenario where an exceptionally efficient high voltage generator is feasible, including the achievement of a perfect impedance matching at the electrodes, the generator's power requirements would match the energy deposited into the system. In the case of a sporadic use of the NRPD, for flame ignition assistance or during transient operation, the electric power requirements of a NRPD system is not a major driver in the development of plasma-assisted combustion technologies. Although the mean NRPD electric power reported in previous works is on the order of 1 percent of the thermal power of the flame [54, 86], it is worth mentioning that the cost-benefit analysis of an NRPD system with an electric power of 1 percent of the combustor thermal power would not be straightforward for heavy duty gas turbines, for the following two reasons. First, 1 percent is still a large penalty for gas turbine manufacturers which struggle for gaining any 0.1 percent of engine thermal efficiency during stationary operation (over the last decade, this efficiency increased toward 65 percent for combined cycle power plants by only a couple of percents). Second, for an H-class gas turbine exhibiting a combustor with 1 GW of thermal power, it means that, by assuming linear scaling, a system of 10 MW electric power would have to be developed, just for the NRPD actuation, which is technically rather challenging. This study demonstrates that for a sequential combustor, operated at atmospheric pressure, successful actuation suppressing thermoacoustic instabilities can be achieved with a mean plasma power that is about 3 orders of magnitude lower than 1 percent of the thermal power, which would be much more realistic for implementation in practice (for 1 GW of thermal power, one would need about 10 kW of mean plasma power). Therefore, as research

in this area continues, it is foreseen that such NRPD technology may be implemented in future gas turbines burning green H_2 in sequential combustors for compensating the intermittency of renewable sources.

This chapter aims to introduce ultra-low-power nanosecond plasma rapid discharges (NRPD) to thermoacoustically stabilize a sequential combustor which has never been attempted so far. Parametric studies on plasma repetition frequency (PRF) and generator voltage are also performed to investigate the effectiveness of the actuator in suppressing the instability and the associated NO emissions.

2.2 EXPERIMENTAL SETUP

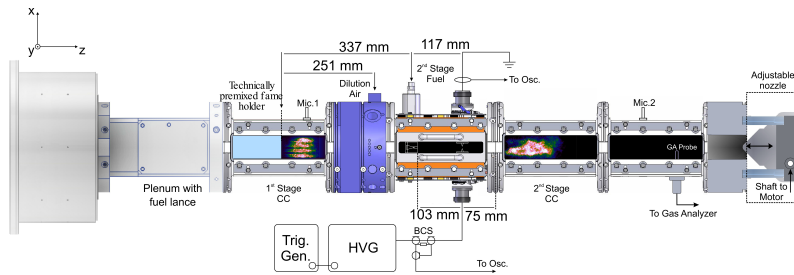


FIGURE 2.1: Lab-scale sequential combustor test-rig. CC- Combustion chamber, HVG- High Voltage Generator, BCS- Back Current Shunt.

The lab-scale sequential combustor is depicted in Figure 2.1. The setup consists of a plenum, a 4×4 array of jet flames anchored on a so-called matrix burner, a combustion chamber with $62 \times 62 \text{ mm}^2$ cross section, a dilution air section, a sequential burner featuring a mixing channel with $25 \times 38 \text{ mm}^2$ cross section in which secondary fuel is injected, a sequential or second-stage combustion chamber equipped with a motor-driven adjustable outlet orifice. This variable outlet geometry enables an online tuning of the acoustic reflection coefficient, and thus an independent control of the thermoacoustic instabilities, which is key for validating the NRPD-based control. The first stage combustor is fed with a mixture of natural gas and air, with the air preheated to 230°C and supplied from the plenum, while natural gas is added in the matrix burner, which corresponds to a technically premixed first stage. The thermal power of the first stage combustor is 35 kW with an equivalence ratio of 0.7. A piezo sensor is placed on a flush mounted plate to monitor the acoustic pressure inside

the first stage and denoted as Mic. 1 in the Figure. A massflow of 18 g/s of dilution air at 25 C is introduced from the dilution air port and mixes with the hot gases from the first stage. A mixture of 0.07 g/s of hydrogen and 0.6 g/s of natural gas is injected into the sequential injector. The sequential injector features an X-shaped vortex generator to enhance the mixing process. The total thermal power of the two flames is 73.4 kW. A pin-to-pin electrode configuration, with an inter-electrode distance of 5 mm, is located 10.3 cm downstream from the sequential fuel injector, and a gas analyzer probe is placed at 45 cm from the outlet of the second-stage burner to monitor the NO emissions. Another piezo sensor is placed downstream of the sequential flame to monitor the acoustic pressure pulsation of in the second combustion chamber. The exhaust gas analysis is conducted using an ABB EL3040 gas analyzer equipped with an Uras26 infrared photometer, operating at a sampling rate of 1 Hz. Automatic calibration with integrated calibration cells and the sealing tests of the propagation line were carried out before the start of each measuring set. The device exhibits a relative extended uncertainty of 7.9% for NO measurements within the range of 0–200 mg/m³.

As indicated above, the outlet of this chamber has an adjustable orifice to control the thermoacoustic stability of the system. The outlet orifice is composed of a conical piston which is connected to a DC motor. Adjusting the position of the piston horizontally enables the variation of the exit area. To measure NO emissions accurately, the system requires continuous operation for a duration of 90 seconds. In order to quantify NO emissions in the absence of plasma discharges, the adjustable orifice is adjusted to stabilize the flame.

The OH* chemiluminescence is used to characterize the sequential flame, with the camera capturing a portion of the mixing channel downstream of the electrodes. The intense light emission from the plasma discharges is masked by an optical obstacle. The recording setup comprises of a LaVision Star X high-speed CMOS Camera and a LaVision HS-IRO high-speed intensifier, which are equipped with a 45 mm CERCO UV lens (F/1.8 Cerco) and an Edmund Optics optical bandpass filter (centered at 310 nm, FWHM 10nm).

To measure the energy deposition of the plasma, a current probe and a back current shunt are placed on the anode and cathode to acquire current and voltage. The plasma generator (FID) initiates the high voltage pulses with a 2-3 ns rise time and a pulsed width of 10 ns. A mixed signal digital oscilloscope (Tektronix MDO3104) was used to record the current

and the voltage signals at 1 GHz bandwidth and 5 GHz sampling rate. A Pearson fast current monitor (model 6585, 0.5 V/A, 50.) was used to measure the current. During testing, four generator voltages (11, 11.7, 12.5, and 14 kV) at three pulse repetition frequencies (10, 20, 40 kHz) were used, with an additional voltage value of 13.2 kV at 40 kHz. All experiments were performed using only the negative polarity of applied pulses.

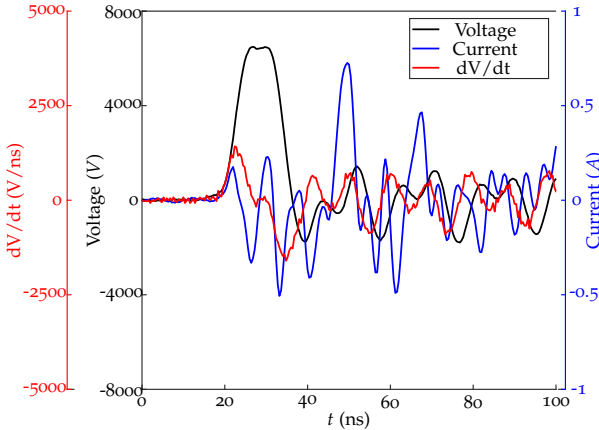


FIGURE 2.2: Measured voltage, current, and the time derivative of the voltage without plasma initiation.

To obtain synchronization between the current and voltage measurements, an additional series of measurements were conducted under cold conditions. During these experiments, the signals of current and voltage pulses were recorded at room temperature and pressure without initiating the plasma. The lengths of the current probe and BCS cables were chosen to be nearly the same to minimize signal propagation time disparities. The displacement current was determined by decreasing the applied voltage amplitude until the peak voltage was smaller than the breakdown voltage value. The procedure used is similar to the one in [87]. As the displacement current is proportional to the derivative of the voltage waveform, an instrumental time lag between the measured current waveform and the time derivative of the voltage signal was calibrated, with a time adjustment of 2.5 ns. This adjustment corresponds to the time lag between current and voltage traces.

Characteristic voltage and current waveforms without plasma initiation are shown in figure 2.2, demonstrating the synchronization process. The absolute value of the conduction current during discharge was found to be significantly higher than the displacement current values, and thus the value of the latter was neglected when calculating the deposited energy values.

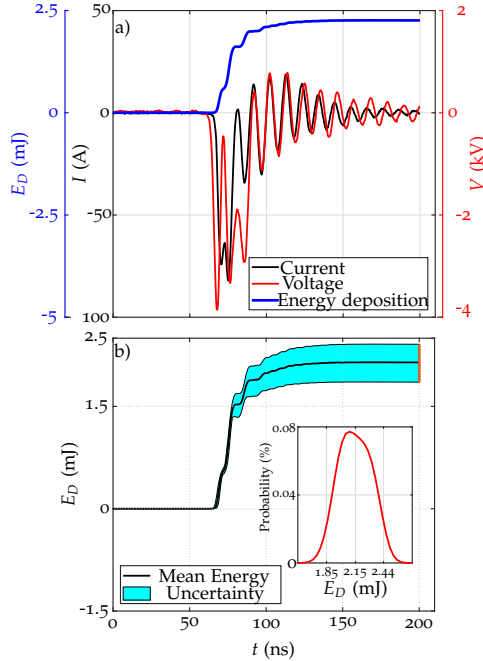


FIGURE 2.3: a) One realization of current (black), voltage (red), and energy deposition (blue). The energy deposition is obtained by taking the integral of the product of the current and voltage signal. The measured voltage corresponds to the voltage across the electrodes' gap and hence it is not necessarily equal to the voltage of the generator. b) The time trace of the mean energy deposition and the uncertainty bound at every time instance. This uncertainty range encompasses the minimum and maximum values derived from all measured pulses. The inset shows the distribution of the energy deposition at the end of each measurement ($t = 200$ ns).

Figure 2.3a illustrates the deposited energy measured within one pulse of the applied burst (14kV and 10kHz). The observed oscillations in voltage and current are due to the mismatch between the generator impedance and the plasma impedance. Under these conditions, the mean energy deposition is approximately 2mJ, classifying the plasma as spark plasma [88].

To obtain a precise estimate of the mean plasma power, the data were gathered over a substantial number of applied pulses. Figure 2.3b displays the time trace of the mean value (solid black line) and the confidence intervals (cyan shadow) of the deposited energy measured over 500 applied pulses. The inset provides a clear representation of the distribution of the final values of the instantaneous energies. Further in the text, the error bars of the deposited energy are defined as $(\pm 2 \cdot \sigma)$, where σ is the standard deviation of the final values of the measured energy profiles. Note that the measurements of current and voltage were conducted during the open-loop plasma actuation and may not fully represent the transient case for the transition from a state without plasma to a state with plasma. The temporal evolution of the voltage and current signals is recorded during the time period of 5 ms after the steady-state conditions are reached (10 s after the start of NRPD actuation). For each operating condition, this recording was repeated 10 times to acquire more pulses for an overall statistical analysis of the deposited energy per pulse.

The resulting energy deposition under all conditions is shown in Figure 2.4a). It is interesting to note that the y-axis has a logarithmic scale, and the energy deposition increases exponentially with respect to the generator voltage. Furthermore, except at 14 kV, the energy deposition per pulse at higher frequencies and the same voltage decreases. This is probably due to the interference between the incoming and reflected pulses inside the high voltage cable. Additionally, no plasma was observed at 11kV and 40kHz, consequently, the data cannot be displayed in the plot.

By multiplying the energy deposition and the plasma repetition frequency (PRF), the mean plasma power is obtained and shown in figure 2.3b). The highest power is at 81 W, which corresponds to 1.1×10^{-1} percent of the thermal power of the flames. The ratio between the plasma and thermal power is indicated on the right axis of figure 2.4(b), denoted as η_p .

2.3 RESULTS

Figure 2.5 shows the effects of plasma discharges on the stability of the sequential combustor at a PRF of 10 kHz and generator voltage of 11.7 kV.

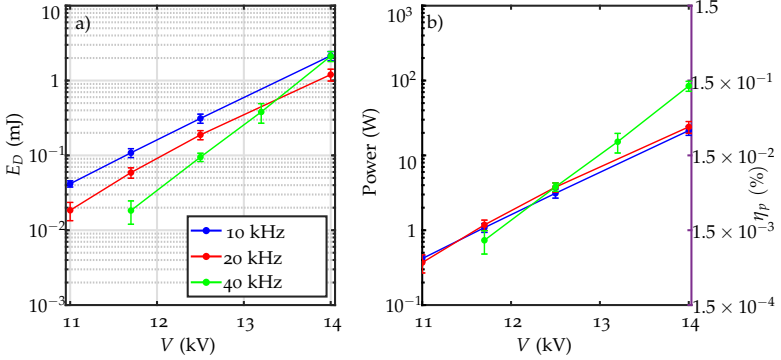


FIGURE 2.4: Energy deposition measurement a) and the plasma power b) at three different PRFs and four generator voltages. The mean plasma power is obtained by taking the product of the PRF and the energy deposition. The ratio between the mean plasma power and the thermal power of the combustor is indicated on the right y-axis in b). There is no plasma discharge observed at PRF = 40 kHz and $V = 11$ kV. The error bars represent the uncertainty at the $\pm 2\sigma$ level

The plasma was turned on at $t = 5$ s and turned off at $t = 35$ s. In Figure 2.5a and 2.5b, the acoustic pressure signals from the first and second stage combustion chambers are presented, along with their corresponding power spectra. The definition of power spectra is as follow:

$$S_{pp}(\omega) = 20 \log_{10} \left(\frac{\hat{p}_{rms}(\omega)}{2 \times 10^{-5} \text{Pa}} \right) \quad (2.1)$$

where ω is the frequency, \hat{p}_{rms} is the root mean squared of the pressure signal, and $S_{pp}(\omega)$ is the power spectrum at the corresponding frequency.

Without plasma discharges, the combustor exhibits a strong pulsation at the frequency of 330 Hz, by looking at the corresponding probability density of the bandpass filtered time trace around 330 Hz, it is clear that the system exhibits a stable limit cycle. Furthermore, the power spectra of the first microphone show a resonance peak at 260 Hz for which the importance will become clearer later.

Immediately after the start of plasma actuation, a burst of the mean pressure signal is observed, which then decays to the nominal value. This burst is attributed to the rapid change in flame position induced by the start of the NRPD and the presumed abrupt variation of pressure drop across the sequential burner. Nevertheless, its amplitude and relaxation

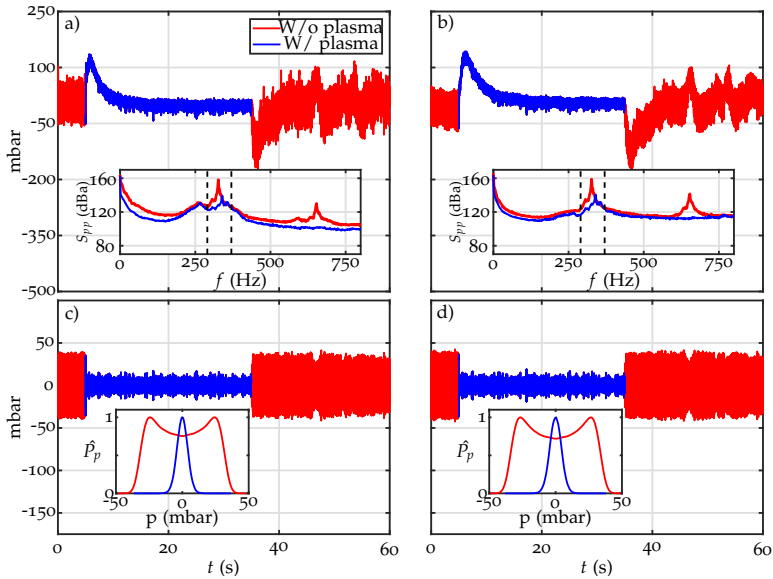


FIGURE 2.5: The time trace of the acoustic pressure signal with and without plasma discharges and their corresponding power spectra inside the first a) and second b) stage combustion chambers. The PRF is at 10 kHz, and the generator voltage is at 11.7 kV. The mean plasma power is 1.1 W, which is about 1.5×10^{-3} percent of the thermal power of the flame. The band-pass-filtered acoustic pressure signal and its associated normalized probability density function inside the first c) and second d) stage combustion chambers. The low-pass and high-pass frequencies are indicated by the dashed lines in a) and b).

time do not provide quantitative information about the actual evolution of the mean pressure in the combustor, as the piezoelectric sensor's signal is high-pass filtered in the data acquisition system card and is responsible for this apparent decay. It is possible that the rise in mean pressure is due to the plasma discharges altering the flow conditions around the flame. The purpose of this work is to study thermoacoustic stability control with NRPD. Therefore, the acoustic signals are bandpass filtered around the thermoacoustic peak frequency of 330 Hz and are shown in Figure 2.5c and 2.5d, along with their corresponding scaled probability density functions (PDFs) in the inset.

As seen in Figure 2.5c and 2.5d, when the plasma is on, the combustor becomes linearly stable. On the contrary, without the plasma, the PDF of the acoustic pressure exhibits a bimodal distribution, which is a typical feature of a system that undergoes a limit cycle. Additionally, the first harmonic at around 660 Hz is also detected in the spectra.

Figures 2.6a to 2.6f show the OH chemiluminescence of the sequential chamber and of a portion of the burner mixing channel. In Figures 2.6a to 2.6c, the OH chemiluminescence is shown at three different time instances before plasma initiation, while Figures 2.6d to 2.6f show the OH chemiluminescence after plasma activation. The PRF is at 10 kHz with a generator voltage of 11.7 kV. The mean intensity within the red and blue squares in Figures 2.6a to 2.6f is illustrated in figure 2.6g. Figure 2.6h depicts the acoustic pressure inside the first and sequential combustion chambers. Remarkably, the thermoacoustic limit cycle in the sequential combustor can be effectively suppressed with a mean plasma power of only 1.1 W, which is about 1.5×10^{-3} percent of the thermal power of the flame. The mean plasma power in our case is similar to that in [86]; however, the thermal power of the flame in our case is 300 times higher than in their case.

In Figure 2.7, the frequency spectra of the pressure oscillations are displayed, with the PRF fixed at 10 kHz and at varying generator voltages. It is evident that the peak corresponding to a limit cycle around 330 Hz becomes smaller, and thus corresponding to a thermoacoustic stabilization, and shifts to higher frequencies as the voltage and energy deposition increase. This frequency shift can be indirectly attributed to a change in the mean flame position, which will be quantified later. In Figure 2.7a, another peak at around 260 Hz becomes more prominent as the voltage is increased, but the gaussian-like PDF of the acoustic pressure filtered around that peak (not shown here), indicates that it remains a resonance peak, i.e. the thermoacoustic oscillations at that frequency are linearly stable. Notably,

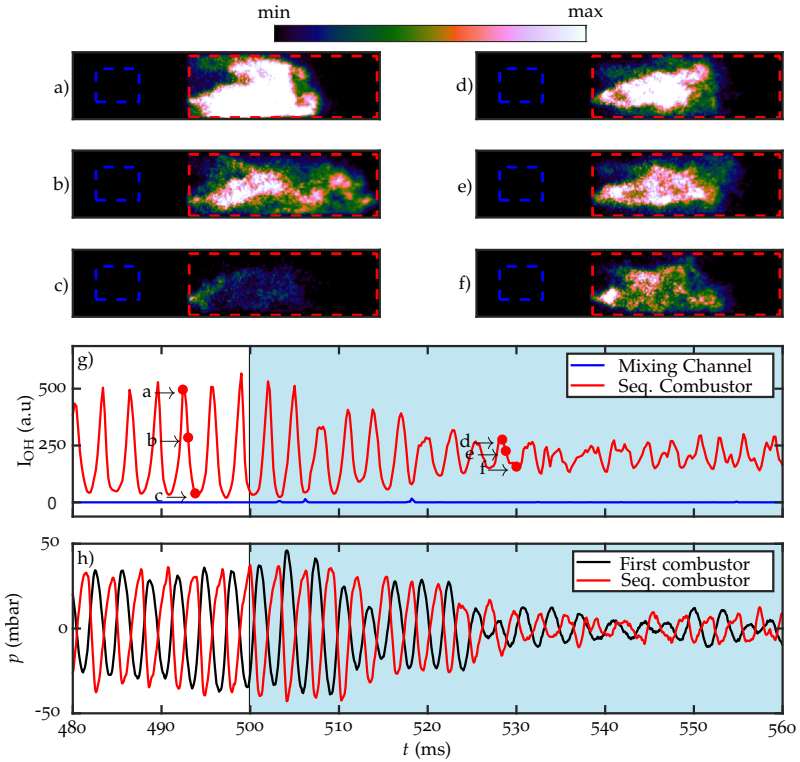


FIGURE 2.6: (a-f) OH chemiluminescence of the sequential combustor at 6 different time instances with the time instances shown in g). The PRF is 10 kHz and the generator voltage is 10 kV. Plasma is initiated at $t = 500$ ms. g) The mean OH intensity inside the mixing channel and sequential combustor. h) The bandpass filtered acoustic pressure signal inside the first and sequential combustor.

the first microphone has a more intense peak around 260 Hz, compared to the second microphone. However, for the mode at 330 Hz, almost the same amplitudes are observed with both microphones.

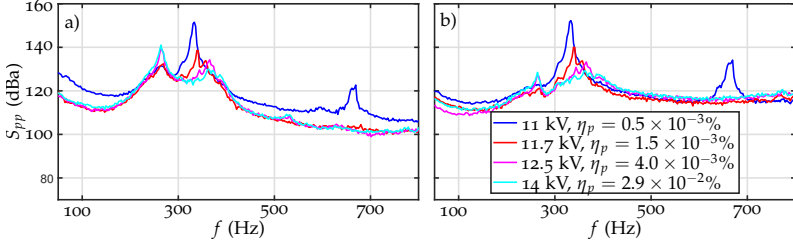


FIGURE 2.7: The frequency spectra of the acoustic pressure signal with plasma discharges at PRF = 10 kHz and four different generator voltages inside the a) first and b) second stage combustor.

Another important aspect of the actuator's performance is its ability to stabilize the system quickly, which can be expressed as a decay rate. To measure this decay, in a similar way to [38], a periodic on-off cycle of plasma actuation is applied. The plasma is turned on for 5 seconds, followed by a 5-second off period, and the entire cycle is repeated for 5 minutes. The time trace of the first microphone's bandpass-filtered acoustic signal during this process is shown in Figure 2.8, with the PRF set at 10 kHz and the generator voltage at 12.5 kV. The envelope of the acoustic pressure signal A is obtained from these data by computing the analytical signal using the Hilbert transform and is averaged over the cycles. Figure 2.8 illustrates the distribution of the pressure envelope at different time points, with the black line indicating the mean value. This procedure is repeated at generator voltages of 11.7 kV and 14 kV. The resulting decay rates at different voltages are shown in Figure 2.9, where the envelope is normalized to its value at $t = 0$ for a better comparison. It is evident that the envelope decays faster as the voltage increases. The system takes around 30 ms to reach a quasi-steady-state value with generator voltages of 12.5 and 14 kV, and the steady-state value is lower at higher voltages.

Figure 2.10 displays the time evolution of the flame centre of mass at PRF of 10 kHz and various voltages. The OH^* chemiluminescence data are vertically integrated, and the centre of mass is computed along the streamwise direction. At 11 kV, the plasma has little effect on the flame, and the fluctuation around 330 Hz is still evident. With increasing voltage, the fluctuation of the flame centre of mass decreases more rapidly, which

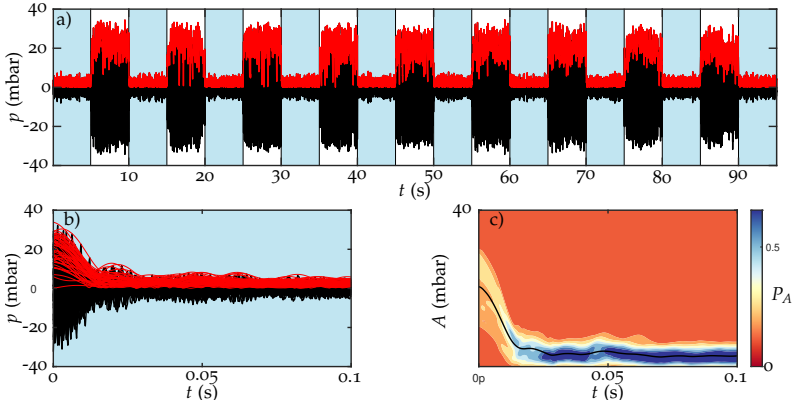


FIGURE 2.8: a) Periodic on-off plasma excitation at PRF = 10 kHz and generator voltage of 12.5 kV, the modulation frequency is at 0.1 Hz, red and black line depict the envelope and acoustic pressure evolution, respectively. The blue shaded regions show the period in which the plasma is on. b) Cycle to cycle superposition of acoustic pressure time trace. c) The time evolution of the distribution of the acoustic pressure envelope A is shown for the first 0.1 second of the actuation. The mean envelope \bar{A} is the black line.

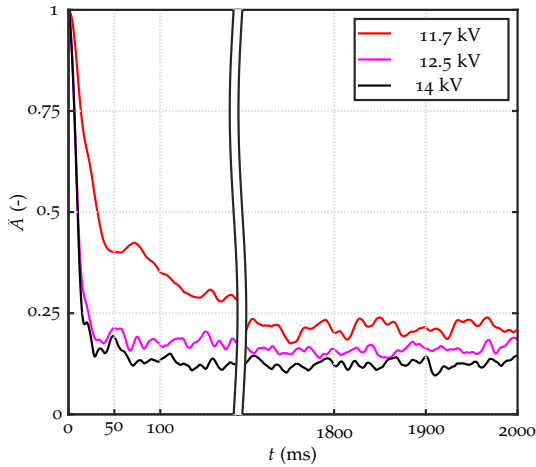


FIGURE 2.9: Evolution of the normalized mean acoustic pressure envelope after plasma is applied at three different generator voltages. The values of the envelope are normalized with respect to their value at $t = 0$ ms

is strongly correlated with the pressure signal. Moreover, the steady-state value of the flame centre of mass with plasma actuation decreases as the voltage is increased, and the centre of mass shifts closer to the burner outlet. This shift is due to higher energy deposition, resulting in increased mean plasma power that enhances the autoignition process in the mixing section of the sequential burner more effectively.

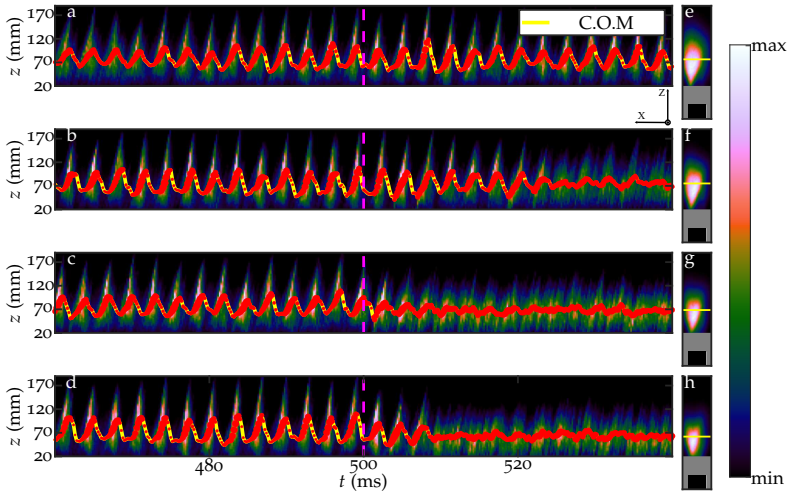


FIGURE 2.10: Evolution of the OH^* intensity integrated horizontally along the x -axis and the flame centre of mass before and after the plasma actuation (a-d). Only the region in the sequential combustor, which corresponds to the red box in figure 2.6, is considered. The start of the plasma actuation is at $t = 500$ ms and indicated by the dashed magenta line in (a-d). The size of the red markers is proportional to the sum of OH^* chemiluminescence intensity. The PRF is fixed at 10 kHz, the generator voltages are a) 11 kV, b) 11.7 kV, c) 12.5 kV, and d) 14 kV. The corresponding averaged flame OH^* chemiluminescence images after the plasma initiation for each generator voltage are presented in (e-h).

Although the decay rate gets faster and the acoustic pressure amplitude gets smaller as voltage increases, NO emissions increase slightly. Figure 2.11 shows the root mean square of the acoustic pressure p_{rms} , NO emissions, and the flame center of mass with respect to generator voltage. As it can

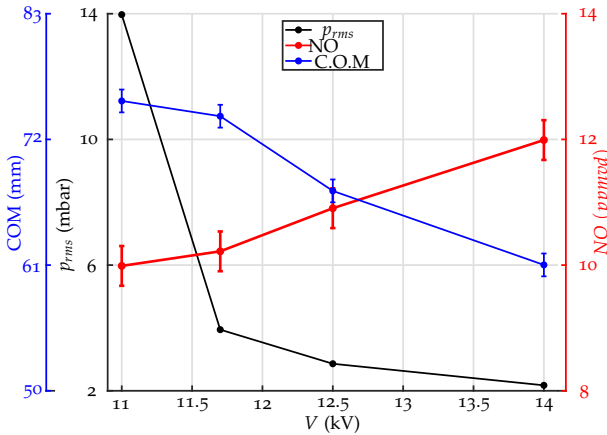


FIGURE 2.11: The dependency of root mean squared of acoustic pressure (band-pass filtered around 330 Hz), NO emission, and the flame centre of mass on the applied generator voltage. The PRF is fixed at 10 kHz. The error bar of the flame centre of mass represent the uncertainty due to the spatial resolution. The error bar of the NO measurement represent the uncertainty of the measurement device. The error of the root mean squared of the acoustic pressure becomes vanishingly small and not shown in the plot.

be seen, NO emissions increase from around 10 ppmvd at 11 kV to around 12 ppmvd at 14 kV. It is a well-known fact that spark plasma can produce significant NO emissions [89]. However, in our configuration, the flame center of mass is shifted upstream, resulting in an increased residence time for the burnt gases which can also be the cause of the NO increase. Furthermore, the energy deposition increases by an order of magnitude, from 0.2 mJ to 2 mJ, as depicted in figure 2.4. According to [57], the plasma regime changes from glow to spark. However, NO emissions only increase by less than 1 ppmvd. The exact mechanism behind this process is not yet clear, and further investigations are needed.

In the context of the stabilization mechanism by NRPD, recent research by [90] demonstrated a notable influence of NRPD on the gain of the flame transfer function (FTF). Furthermore, as the application of NRPD leads to an upstream shift of the centre of mass of the sequential flame within our experimental setup, as shown in Figures 2.10 and 2.11, it is reasonable to anticipate a corresponding variation in the phase of the FTF. Research

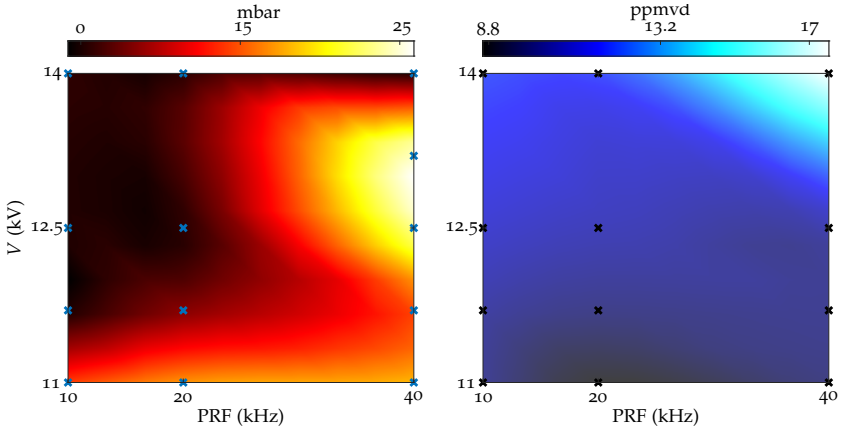


FIGURE 2.12: Contour maps of the rms acoustic pressure (left) and the NO emission (right) with respect to the variation of plasma repetition frequency and pulses voltage. The crosses indicate the measurement points. The bandwidth for the rms acoustic pressure calculation is from 200 Hz to 400 Hz. The NO measurement at $V = 13.2$ kV and $PRF = 40$ kHz is not available because the combustor cannot be operated for a long enough time interval under this condition due to excessive acoustic amplitudes.

presented in [91] has demonstrated how the changes in both flame transfer function's gain and phase can influence the stability of the system. The potential alteration of both gain and phase of the FTF for the sequential flame, induced by NRPD, could consequently introduce variations in the overall stability of the system. To conclusively validate this hypothesis, future investigations will necessitate conducting measurements of the flame transfer function (FTF) for the sequential flame under NRPD conditions, followed by thermoacoustic stability analyses. This line of investigation will be a focal point of forthcoming studies.

The same approach was followed at higher PRFs, and the resulting p_{rms} and NO emission maps are shown in Figure 2.12. Since the thermoacoustic peak of interest in the power spectra of the acoustic pressure is at around 260 Hz that needs to be considered, the bandpass filter was set to span from 200 Hz to 400 Hz for the rms calculation. Examining the map, at 11.7 kV the plasma discharges at $PRF = 10$ and 20 kHz are more effective than at $PRF = 40$ kHz. This is consistent with the fact that the mean plasma power obtained at 40 kHz for this voltage is lower than that at 10 kHz or 20 kHz

as shown in Figure 2.4b. At 40 kHz and 11.7 kV, the plasma is therefore not strong enough to affect the system. However, at 12.5 kV, all mean plasma powers at all PRFs are in the same order of magnitude (see Figure 2.4 b). When the PRF is set to 40 kHz, the rms pressure increases. The same behavior is observed at 13.2 kV, but the system stabilizes again when the voltage is set to 14 kV. Because there is strong pulsation at $V = 13.2$ kV and $\text{PRF} = 40$ kHz, NO measurement could not be performed. However, it is clear that the NO emission map shows an increasing trend towards high PRF and high generator voltage, which is consistent with the findings in [82], which investigated the effect of plasma on the sequential flame position and on the NO emissions in another sequential combustor. Looking at the contour maps, it is evident that staying at $\text{PRF} = 10$ kHz with a pulse voltage above 11 kV, the thermoacoustic eigenmode in the combustor can be effectively stabilized without compromising the NO emissions.

To shed light on the peculiar phenomenon at $\text{PRF} = 40$ kHz, it is interesting to show the power spectra of both microphones. This information is given in Figure 2.13. Notably, at 12.5 kV and 13.2 kV, the mode at 260 Hz becomes self-excited and exhibits a very high amplitude of 160 dB, while

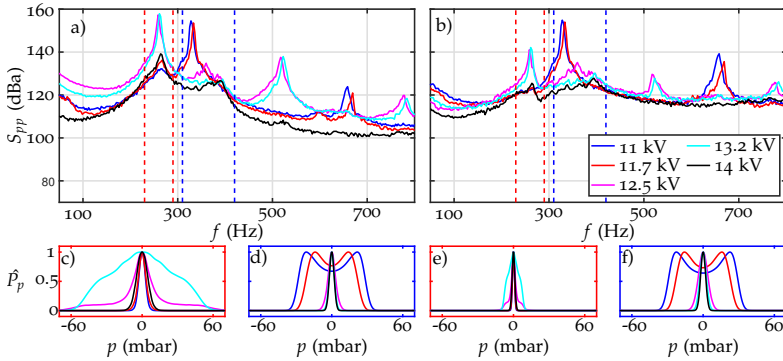


FIGURE 2.13: The frequency spectra of the acoustic pressure signal with plasma discharges at $\text{PRF} = 40$ kHz at four different generator voltages inside the a) first and b) second stage combustor. The acoustic pressure histogram of the bandpass filtered signal inside the first stage combustor at around 260 Hz c) and 330 Hz d). The acoustic pressure histogram of the bandpass-filtered signal inside the second stage combustor at around 260 Hz e) and 330 Hz f). Another mode at around 260 Hz is excited when the generator voltage is at 12.5 kV and 13.2 kV.

the mode at 330 Hz is stabilized. As outlined previously, altering the flame response with respect to the acoustic perturbation, known as the flame transfer function (FTF), can affect the overall stability of the system. Alteration of the center of mass of the flame will affect the phase of the flame response. The alteration of the flame phase can stabilize and destabilize the system in a periodic manner, as demonstrated in [92, 93, 94]. Contrary to previous studies, it is important to note that enhancing the mean power of NRPD does not consistently lead to an enhancement in the suppression of thermoacoustic instabilities. The PDF of the acoustic pressure \hat{P}_p shown in Figure 2.13 c exhibits in the case of repetitive pulses of 13.2 kV a typical feature of an intermittently unstable thermoacoustic system. This observation is also confirmed by the time trace of the filtered signal.

The OH* chemiluminescence signals at 13.2 kV and PRF = 40 kHz, recorded during a time interval when the NRPD was activated, are shown in Figures 2.14a to 2.14f. When the NRPD actuation is turned on with these pulse generator settings, the thermoacoustic dynamics changes from a robust limit cycle at 330 Hz, to a limit cycle at 260 Hz, and in contrast to the PRF of 10 kHz and 20 kHz, the thermoacoustic system is not stabilized. As can be seen in Figure 2.14, OH chemiluminescence is visible inside the mixing channel after plasma actuation, due to the formation of ignition kernels induced by NRPD. Figure 2.14 g shows the intensity of chemiluminescence OH* inside the mixing channel, which fluctuates as the intensity in the combustion chamber at the acoustic pressure oscillation frequency of 260 Hz. The acoustic pressure time trace shown in Figure 2.14h clearly indicates that, before plasma actuation, both microphones record similar acoustic pressure amplitudes. However, after the NRPD are applied, the acoustic pressure in the first stage combustor is significantly higher than that in the sequential combustor. This observation is consistent with Figure 2.13, which shows a 20 dB difference in power spectra at 260 Hz between the two microphones.

To understand the characteristics of the two observed modes at around 260 Hz and 330 Hz, modal analyses by solving the acoustic Helmholtz equation were performed using COMSOL. Figure 2.15 shows the side view of the 3D computational domain and the imposed temperature distribution along the longitudinal direction. The temperature was obtained by computing the adiabatic flame temperature with Cantera. The temperature inside the mixing channel is obtained by assuming a homogeneous mixing between the hot products from the first-stage combustor and the dilution air.

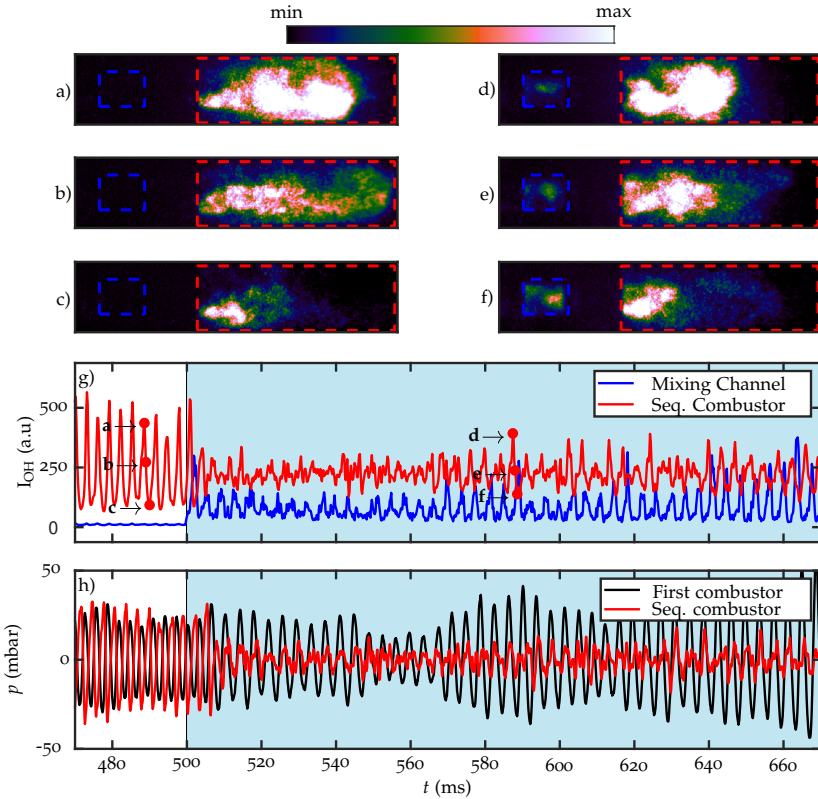


FIGURE 2.14: (a-f) OH chemiluminescence of the sequential combustor at 6 different time instances, the PRF is at 40 kHz and the generator voltage is at 13.2 kV. g) the mean OH* intensity inside the mixing channel and sequential combustor. h) The bandpass filtered acoustic pressure signal inside the first and sequential combustor.

The purpose of the analysis is not to exactly model the complete acoustics of the system. This would require an appropriate description of the complex-valued frequency dependent boundary conditions and loss mechanisms at the area changes as well as the transfer functions of both flames. The intend is to provide a visual rendering of length scales of possible modes involved and that it is plausible that the two observed peaks are of acoustic origin, despite being rather closely spaced in frequency. The inclusion of aeroacoustic and thermoacoustic gains and losses, as demonstrated in the work by [43, 95], can lead to alterations in the system eigenmodes.

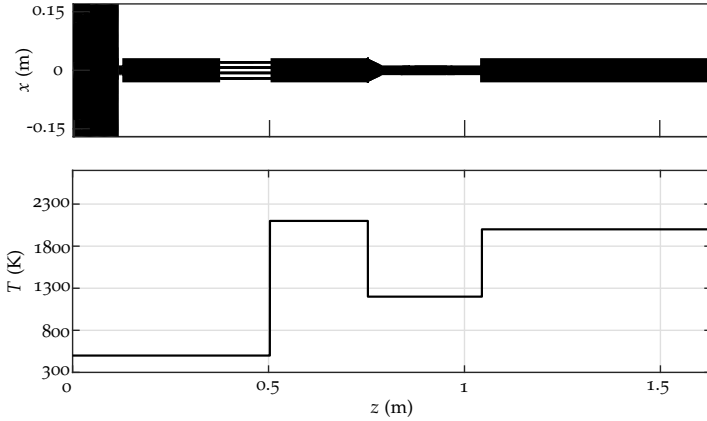


FIGURE 2.15: Side view of the computational domain for the pure acoustic analysis (top). The imposed temperature distribution along the longitudinal direction (bottom).

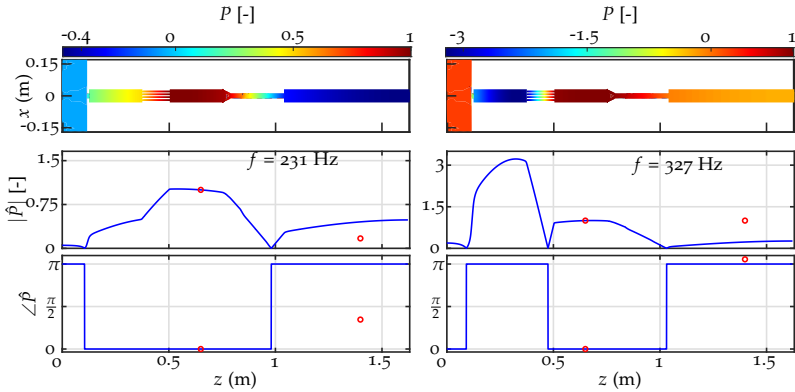


FIGURE 2.16: Computed longitudinal eigenmodes (top), longitudinal profile of the absolute values of the eigenmodes (middle), and the angle of the eigenmodes (bottom). The circles in the middle and bottom plot correspond to the experimentally measured signals. The pressure mode is normalized with respect to its value at the first microphone location ($z = 0.75$ m). The left and right plots show the eigenmodes at the eigenfrequency of 231 Hz and 327 Hz respectively.

Figure 2.16 shows the computed eigenmodes of the pure acoustic problem. The second and third rows compare the solutions with the experiments. The disparities observed between the solutions from the Helmholtz solver and the experimental results can be attributed to the omission of aeroacoustic and thermoacoustic gains in the model. These disparities have been observed in the literature such as [72], and [71]. In summary, the intensity of the peaks at distinct locations is influenced by the combined effects of the pure acoustic modes, aeroacoustic and thermoacoustic gains and losses that constitute the system's eigenmodes.

The plasma discharges are visualized in Figure 2.17. The images are obtained by removing the intensifier from the high-speed camera and the OH* filter from the lens. The plasma volume is calculated by counting the number of pixels whose intensity is greater than the background intensity. The images are phase-averaged with respect to the bandpass-filtered acoustic signals of the first microphone. As seen, during an oscillation cycle, when the acoustic pressure in the first stage combustor reaches the maximum point, the plasma bends more towards the outlet of the sequential burner. Whereas at the other phase angles, the discharge channels are relatively straight. The plasma bending effect is similar to the one observed in [57]. It was noted that plasma bending could become evident when the distance traveled by the plasma-heated fluid parcel during the inter-pulse time (d_{conv}) approaches the gap distance (d_{gap}). Their research showed that the bending occurred sporadically. However, in that study, there was no thermoacoustic instability and plasma bending occurred exclusively at a PRF of 40 kHz. In the present study, the thermoacoustic instability leads to the synchronization of the periodic plasma channel bending with the acoustic field. The time trace of the plasma volume variation and the acoustic pressure pulsation in the first stage also show a strong correlation.

Figure 2.18 shows the NO emissions of the combustor with different NRPD voltages and PRF, plotted against the mean plasma power. A measurement point without plasma, which is indicated by a red cross in Figure 2.18, is obtained by stabilizing the combustor by adjusting the outlet orifice. The maximum NO emission of approximately 17.65 ppmvd occurs at a generator voltage of 14 kV and a PRF of 40 kHz. It is worth noting that high PRF and voltage can cause early ignition inside the sequential burner mixing channel, leading to a reduction in mixing quality between the vitiated flow and the secondary fuel, and consequently a potential increase in NO emissions. A weak correlation between NO emissions and mean plasma power is observed at power levels ranging from 0.1 to 10 W. As the

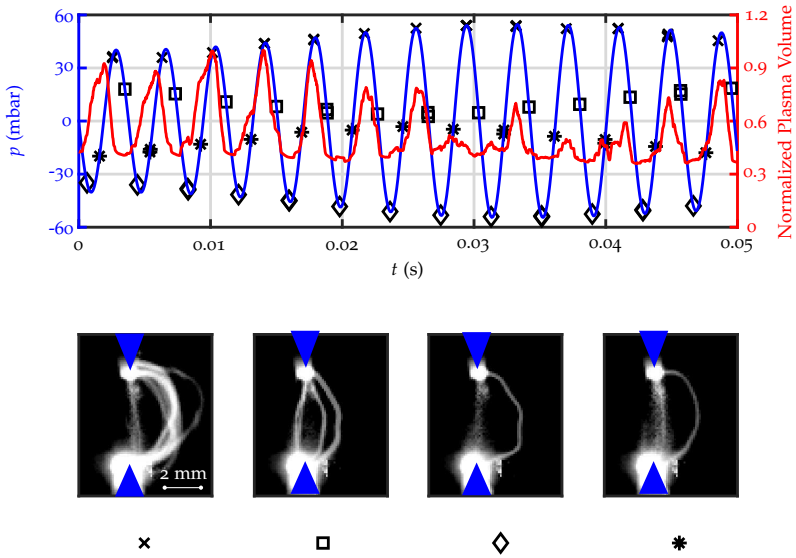


FIGURE 2.17: Phase average of the plasma discharge intensity at $V = 13.2$ kV and PRF = 40 kHz (second row). The minimum and maximum intensity are colored black and white, respectively. The reference signal for phase averaging is the microphone signal inside the first-stage combustion chamber, the normalized plasma volume is plotted in red (first row).

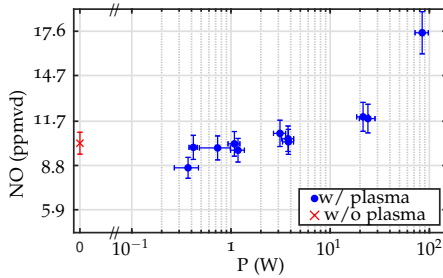


FIGURE 2.18: NO emissions as a function of the mean plasma power. The red cross is the NO measurement under thermoacoustically stable conditions without plasma, obtained by adjusting the orifice geometry of the outlet.

goal of the NRPD actuation in this work is to thermoacoustically stabilize the sequential combustor, a generator voltage of 11.7 kV and PRF of 10 kHz is obviously the optimum because the plasma does not lead to an increase of the NO emissions compared to the nonactuated operation. Furthermore, the present ultra-low-power NRPD-based control strategies for sequential combustors open up other possibilities such as thermoacoustic instability control during transient operation by employing a feedback loop control.

2.4 CONCLUSIONS AND OUTLOOK

This study demonstrates that ultra-low-power non-equilibrium plasma can effectively stabilize a thermoacoustically unstable sequential combustor. Indeed, the power of the plasma produced by the NRPD which can achieve thermoacoustic stabilization can be 5 orders of magnitude lower compared to the flame thermal power: with a mean plasma power of 1.1 W, which is 1.5×10^{-3} percent of the flame thermal power of 73.4 kW, the thermoacoustic limit cycle in the sequential combustor was successfully stabilized. At this condition, there is practically no additional NO emission compared to the situation where the thermoacoustic mode was stabilized by changing the outlet orifice geometry of the combustor with a motor-driven water-cooled piston. However, at PRF = 40 kHz and generator voltages of 12.5 kV, and 13.2 kV, another thermoacoustic mode at 260 Hz becomes self-excited. Therefore, now that an effective ultra-low-power actuator has been found for sequential combustors in the form of NRPD in the sequential burner, a significant part of the research efforts should concentrate on the development of feedback control for ensuring optimum trade-off between global thermoacoustic stability and NO emissions during steady and transient operation. Finally, further investigations are required to demonstrate the practicality of this NRPD actuation at elevated pressures, and to develop predicting tools of the interaction between plasma kinetics and combustion reactions in the thermochemical environment of the turbulent sequential burner.

ACKNOWLEDGEMENTS

This project is based on the paper *“Thermoacoustic Stabilization of a Sequential Combustor with Ultra-low-power Nanosecond Repetitively Pulsed Discharges”* by Bayu Dharmaputra, Sergey Shcherbaney, Bruno Schuermans, and Nicolas Noiray, published in *Combustion and Flame* in October 2023. This project

has received funding from the European Research Council (ERC) under the European Union's Horizon 2020 research and innovation program (grant agreement No [820091]) TORCH (2019-2024).

BOATS: BAYESIAN OPTIMIZATION FOR ACTIVE CONTROL OF THERMOACOUSTICS

If I have seen further, it is by standing on the shoulders of giants.

— Isaac Newton

This chapter presents the use of safe Bayesian optimization (safeOpt) algorithm and two adaptation of it for active control of thermoacoustic instabilities. The main objective of the algorithms is to optimize the control parameters while maintaining safety criteria. The proposed algorithms are data-driven and therefore in principle do not require a model. However, if a model is available, it could be added to the framework as a prior mean function. The performance of the algorithms is evaluated in a numerical simulation and in two experimental setups. The numerical simulation and the first experimental setup are the well-known active control of thermoacoustics with loudspeaker actuation. The controller is the classical phase-shifter or gain-delay ($n - \tau$) controller. The algorithms optimize control parameters iteratively. The second experiment employs nanosecond repetitively pulsed discharges (NRPDs) to control the thermoacoustics of a lab-scale sequential combustor. The proposed algorithms help to find regions with low NO emissions that are unstable without NRPDs actuation.

3.1 INTRODUCTION

Active and passive control strategies have been extensively studied in the context of thermoacoustic control. Due to their simplicity, passive control strategies have dominated the industrial gas turbine application. Passive control strategies can be grouped into two categories. The first category relies on the increase of the acoustic losses of the combustor [96]. Typical examples in this category are Helmholtz dampers and quarter-wave resonators. The second category deals with reducing the acoustic driving of the combustion process.

Quarter-wave and Helmholtz resonators are the most commonly used devices, which belong to the first category. Pandalai et al. [52] showed

an example of quarter-wave resonators placed in the cold section of the combustor upstream of the premixers in a GE aeroderivative engine. The authors noted that the resonator has logged more than 100000 hours of engine operations in factory testing and commercial operation. Quarter-wave resonators have the disadvantages of a typical narrowband response and a length requirement which can be prohibitive for typical frequencies in stationary engines [97]. Bellucci et al. [98] designed a Helmholtz damper that was later used in a Silo compressor (ALSTOM GT11N2) and also presented a nonlinear model to predict the loss coefficient and the natural frequency of the resonator.

Significant research has been conducted in the recent years to optimize the design of acoustic dampers for gas turbine combustors. For example, Bourquard and Noiray compared the volume and purge flow requirements of Helmholtz and quarter-wave resonators, and also showed that the optimum linear stability is achieved when these dampers are tuned to an exceptional point of the thermoacoustic system [99]. Later, Miniero et al. [73] studied the effect modelled and investigated experimentally the generic problem of periodic hot gas ingestion into Helmholtz dampers mounted on combustion chambers. They presented an analytical model for robust damper design, which can be used to limit the risk of passive control failure due to dynamic change of nonlinear damping and detuning.

Examples of the passive control strategy in the second category can be found in [100, 101]. In [100], burners with fuel injection at different axial locations are used to suppress acoustic pulsation. Such an axial staging leads to a bimodal distribution of the time delay corresponding to the convection of coherent equivalence ratio perturbations from the burner to the flame. The dynamic phase converter presented by Noiray et al. in [51] is also based on an axial staging principle, but it relies on the bimodal time delay distribution of another type of convective coherent perturbations between the burner and the flames: the hydrodynamic ones. In fact, it works by converting long-wavelength acoustic perturbations into short-wavelength hydrodynamic perturbations thanks to diaphragms in the injection channels. The positions of the diaphragms are staggered to cancel out the fluctuating response of one-half of the reaction zone with the other half. The stagger distance should be tuned to achieve effective cancelation at a target frequency. A more recent example is presented in [102] that is based on the alteration of flame transfer functions by modifying the geometry of the axial swirler and its position relative to the burner outlet.

One of the disadvantages of passive control strategies is that they require extensive engine testing to acquire accurate knowledge of the system. For example, the instability frequency for different operating conditions must be known in order to design the appropriate damper geometry. Modifications to the burner geometry, either by adding diaphragms or changing the swirler geometry, might lead to additional unwanted pressure head loss.

Active control strategies, on the other hand, could adapt to the changes in operating conditions. Seume et al. [79] presented an active control strategy with pilot fuel flow modulation for the V84.3A gas turbine model. The control parameters consisted of gain and phase change ($n - \tau$ controller), and the actuators were multiple direct drive valves (DDV). The system was applied to a Siemens V94.3A heavy duty gas turbine and logged 18000 operating hours [103]. However, the bandwidth of the actuator is limited to 400 Hz. Another notable application of adaptive control in the GE aero derivative engine is presented in [52], where the combustor pulsation was measured with piezo sensors, and the control actuation is achieved through the splitting of the fuel between the inner, pilot, and outer rings of the burner.

Active control algorithms have been extensively studied for thermoacoustic stabilization. Gelbert et al. [104] demonstrated for the first time the application of Model Predictive Control (MPC) to stabilize a turbulent swirl-stabilized combustor. The MPC requires a suitable model to work, in which the authors identified a priori. It was also noted that the system had to be in a stable state first, by adjusting their control parameters, for the MPC to work properly. There was no constraint implemented in both the states and the input variables; hence, the resulting Quadratic Programming (QP) problem can be solved in one step, enabling them to run the MPC algorithm with a sampling step of 1 ms. Adding input or state constraints might complicate optimization problems and increase the sampling time [105]. MPC algorithm can also be robust with respect to some uncertainties; however, it always trades off between robustness and optimality [105]. Nevertheless, the main drawback of model-based control is to find suitable models that can capture all the relevant operating conditions in gas turbines. The identification of the model parameters might be challenging and time consuming. Another control paradigm that addresses this issue is the adaptive control strategy.

An example of adaptive control is the Extremum Seeking Controller (ESC). The demonstration of ESC for thermoacoustic stabilization was presented in [106]. In that study, the actuator is a loudspeaker equipped

with a gain-delay controller. The ESC is used to adaptively tune the gain and delay parameters. ESC works by constantly perturbing the parameters with a low-amplitude sinusoidal function and subsequently computing the gradient of the objective function with respect to the control parameters. The gradient information is then used to drift the mean value of the parameters. The ESC algorithm was improved in [54] by encoding the slope information of the objective function so that the optimizer does not fall into a local maximum with zero gradient. However, there was no constraint encoded in the optimizer.

A more recent adaptive control method for thermoacoustic stabilization with a loudspeaker is presented in [107], where an active disturbance rejection control (ADRC) is implemented. The ADRC algorithm was originally introduced in [108] and works by treating the unknown plant dynamics as a disturbance that is tracked by an extended state observer (ESO). In principle, the ADRC algorithm is model-insensitive and can handle nonlinearities in the system. However, as demonstrated in [107], tuning its free parameters would require proper modeling of the thermoacoustic system to obtain reasonable values.

Most control synthesis methods, such as MPC, ARDC, and sliding mode controller (SMC) [109], typically assume that all states are observable. If some states are not observable, an observer-based method can be employed such as Extended Kalman Filter (EKF). However, such an observer would require a model to work, and if the system is nonlinear, the convergence of the estimator might be an issue. Furthermore, the input action is typically assumed to be affine to the system, and can be written in the form of:

$$\dot{\mathbf{x}} = F(\mathbf{x}) + G(\mathbf{u}), \quad (3.1)$$

where $\mathbf{x} \subset \mathbb{R}^n$ contains the state variables, $F : \mathbb{R}^n \rightarrow \mathbb{R}^n$ is some (non)-linear function of x and $G : \mathbb{R}^m \rightarrow \mathbb{R}^n$ is some (non)-linear function of the input forcing $\mathbf{u} \subset \mathbb{R}^m$.

Research in [90] has shown that the application of NRPD changes the flame response with respect to acoustic perturbations or, in other words, the flame transfer function (FTF). It is also demonstrated in [110] that NRPD can stabilize a sequential combustor with continuous forcing and hence without a feedback loop. Therefore, these results hint that the NRPD forcing is not affine to the dynamics of the system. Therefore, most of the control synthesis methods are not directly implementable in this case. In addition to that, the exact mechanism of thermoacoustic stabilization of a sequential combustor with NRPDs actuation is not yet well understood, making the

development of a simplified, low-order model a complex task. Therefore, adaptive control algorithms are more suitable for this application

To address the issues, this chapter proposes an adaptive control method that is based on safe Bayesian optimization (safeOpt) which was first presented in [111]. This method is fundamentally data-driven, employing Gaussian Process Regressions (GPR) to approximate both objective and constraint functions. In that study, the safeOpt algorithm was used to optimize the parameters of a proportional derivative (PD) controller of a quadcopter. They showed that an optimum parameter combination could be found while also satisfying the safety constraint. The algorithm is further detailed in [112], where they showed that, by using context, the knowledge about good control parameters obtained at low tracking speeds can be transferred to fast tracking speeds. Khosavi et al. [113] implement the same algorithm to optimize the gains of the PID cascade controller of a computer numerical control (CNC) grinding machine through both numerical and experimental tests. Their results showed that the algorithm performs 20% better than the nominal approach. Finally, it is worth mentioning the recent work of Reumschuessel et al. [114], who employed a Bayesian optimization-like strategy, albeit not based on the safeOpt algorithm, for experimental combustor design.

The present study introduces the safeOpt algorithm and two modified versions of the algorithm for active control of thermoacoustic instabilities in turbulent combustors. The algorithms are demonstrated in both numerical and experimental settings. The safeOpt algorithm will first be demonstrated in a numerical setup by employing a low-order thermoacoustic network model. Subsequently, the safeOpt algorithm and two additional modifications of it will be demonstrated in the experimental swirl-stabilized turbulent combustor setup. Finally, the safeOpt algorithm is demonstrated in a sequential combustor equipped with NRPD as the actuator.

The suitability of the safeOpt algorithm for thermoacoustic applications arises from its data-driven methodology (and hence does not require a model of the problem at hand), ability to adhere to constraints such as e.g. pollutant emission levels, input signal to actuators, turbine inlet temperature, etc., and straightforward implementation. Although the algorithm can incorporate information from a model into the prior mean function of the Gaussian Process Regression (GPR), our focus in this study is on scenarios where no such model is available, relying solely on measurements for optimization.

3.2 BACKGROUND THEORY

A detailed explanation of the safeOpt algorithm is outlined in [112]. Therefore, only a brief overview of the theoretical foundation is explained in this section. The problem statement is briefly outlined in Section 3.2.1. A brief overview of the Gaussian Process is discussed in Section 3.2.2. Afterward, the safeOpt algorithm and its modifications are explained in Section 3.2.3 and Section 3.2.4, respectively. Finally, the Bayesian context framework is discussed in Section 3.2.5.

3.2.1 Problem Statement

The goal of the proposed algorithm is to find control parameters \mathbf{p} which optimize a scalar objective function O , under a certain constraint condition which is described by a constraint function C . The control parameters belong to a domain $\mathcal{P} \subset \mathbb{R}^n$. The objective function is defined as a map from the control parameter space to a scalar value: $O(\mathbf{p}) : \mathcal{P} \rightarrow \mathbb{R}$. Similarly, the constraint function is defined as: $C(\mathbf{p}) : \mathcal{P} \rightarrow \mathbb{R}$. Furthermore, it is assumed that there is an upper threshold value $T \in \mathbb{R}$ in which the system can be classified as safe: $C(\mathbf{p}) \leq T$. Note that the framework can be extended to include multiple constraint functions as described in [112].

Both the objective function O and the constraint function C are not known a priori but can be approximated by measurements for a given combination of control parameters \mathbf{p} . The algorithm will perform iteration updates and try to find the optimum point(s) of the aforementioned constrained optimization problem while ensuring that the safety condition is satisfied at each iteration N . Note that the objective is to **minimize** the pressure pulsation; hence, this boils down to a minimization problem. Therefore, the optimization problem can be summarized as follows:

$$\min_{\mathbf{p} \in \mathcal{P}} O(\mathbf{p}) \text{ subject to } C(\mathbf{p}) \leq T \quad (3.2)$$

Since both the objective and constraint functions are not known a priori, an initial safe parameter set would need to be acquired. The set can be identified through simulations, expert domain knowledge, or some preliminary points evaluations. In this study, it is identified by performing multiple points evaluation in the domain \mathcal{P} to obtain the initial set of safe parameters $\mathcal{S}_i \subset \mathcal{P}$.

To expand knowledge of the safe parameter set beyond \mathcal{S}_i , the algorithm needs to infer whether some parameters p^* that have not been evaluated

are safe or unsafe. The Gaussian Process (GP) model is employed to approximate both the objective and constraint functions. Therefore, some regularity assumptions must be introduced for O and C [112]. By using GP, a reliable confidence interval over O and C can be constructed, thus enabling the satisfaction of the safety condition throughout the iterations with high probability. \hat{O} and \hat{C} denote the GP approximation of O and C , respectively. More precisely, since every measurement is contaminated by noise the GP approximations are defined as:

$$\begin{aligned}\hat{O}(\mathbf{p}) &= O(\mathbf{p}) + \epsilon_o, & \epsilon_o &\sim \mathcal{N}(0, \sigma_o^2) \\ \hat{C}(\mathbf{p}) &= C(\mathbf{p}) + \epsilon_c, & \epsilon_c &\sim \mathcal{N}(0, \sigma_c^2)\end{aligned}\quad (3.3)$$

where ϵ_o and ϵ_c are gaussian random noise with zero mean and variance σ_o and σ_c , respectively.

Note that due to the safety constraint condition, the algorithm might not be able to find the global optimum, however, it will aim to find the optimum parameters that are reachable from the initial safe set \mathcal{S}_i .

3.2.2 Gaussian Process

In this work, GPs are used to approximate the objective function $O(\mathbf{p})$ and constraint function $C(\mathbf{p})$. GPs are non-parametric regression models that assume that the function values of the approximated function are random variables that have a joint Gaussian distribution [115]. A GP is described by a prior mean function and covariance function. The latter describes a covariance between two different parameter values: $\mathbf{p}, \mathbf{p}' \in \mathcal{P}$. The most commonly used term for the covariance function is kernel. In this study, a constant $K \in \mathbb{R}$ is used as the prior mean function and squared exponential kernels or Gaussian kernels as the covariance function. Note that the choice of the kernels is problem-dependent, a detailed overview of possible kernels is available in [115]. The squared exponential kernel is defined as:

$$k(\mathbf{p}, \mathbf{p}') = \theta \exp\left(-\frac{d^2(\mathbf{p}, \mathbf{p}')}{2}\right) \quad (3.4)$$

$$d^2(\mathbf{p}, \mathbf{p}') = (\mathbf{p} - \mathbf{p}')^\top \mathbf{L}^{-2} (\mathbf{p} - \mathbf{p}') \quad (3.5)$$

where \mathbf{L} is a diagonal matrix of positive real numbers representing the length scales: $\mathbf{L} = \text{diag}(\mathbf{1})$, $\mathbf{1} \in \mathbb{R}_+^n$. Note that n is the dimension of the control parameter space. The parameter θ represents the range of expected values of the difference in the value of the function and the previous

mean function: $|K - O(\mathbf{p})| \leq 2\theta$ with 95% probability. The length scales \mathbf{I} represent how fast the covariance between neighboring points decays with respect to their distance in the control parameters space \mathcal{P} . The last set of hyperparameters is the variance of measurement noise σ_o^2 and σ_c^2 in eq. (3.3). In principle, the hyperparameters can also be optimized every time new data is acquired. However, as shown in [116], this can lead to a poor result when using the maximum likelihood estimate to update the hyperparameters. Therefore, in the framework of safeOpt, the kernel hyperparameters are fixed from the beginning and treated as prior over functions. Hence, this represents the user's knowledge about the functions that are modeled.

GPs can predict the function values $O(\mathbf{p}^*)$ and $C(\mathbf{p}^*)$, for any $\mathbf{p}^* \in \mathcal{P}$ based on the acquired data in the previous N measurements. Until the end of this section, the notation of N is shortened to n for brevity. Conditioned on the measurements, the posterior distribution of the objective function (and equivalently the constraint function) is also Gaussian with the mean and variance as follows:

$$\mu_n(\mathbf{p}^*) = \mathbf{k}_n(\mathbf{p}^*)(\mathbf{K}_n + \mathbf{I}_n\sigma_o^2)^{-1}\hat{\mathbf{O}}_n + K \quad (3.6)$$

$$\sigma_n^2(\mathbf{p}^*) = k(\mathbf{p}^*, \mathbf{p}^*) - \mathbf{k}_n(\mathbf{p}^*)(\mathbf{K}_n + \mathbf{I}_n\sigma_o^2)^{-1}\mathbf{k}_n^\top(a^*) \quad (3.7)$$

where $\hat{\mathbf{O}}_n$ is the vector n observed values, σ_o is the standard deviation of the observation noise, $\mathbf{k}_n(\mathbf{p}^*)$ is the covariance vector between the new point \mathbf{p}^* and the observed data points, and $\mathbf{K}_n \in \mathbb{R}^{n \times n}$ is the covariance matrix of the observed data points, and \mathbf{I}_n is an n by n identity matrix. It is worth mentioning that the kernel function k for the objective and constraint functions may not have the same hyperparameters. For the remainder of the text $k^o(\mathbf{p}, \mathbf{p}')$, and $k^c(\mathbf{p}, \mathbf{p}')$ denote the kernel function for the objective and constraint function respectively.

3.2.3 Safe Bayesian optimization (SafeOpt)

The SafeOpt algorithm, initially introduced in [117] and later extended in [111, 112], is visually represented in Figure 3.1. This algorithm operates by employing Gaussian Process Regressors (GPRs) to model the system's response in terms of objective and constraint function values. Utilizing uncertainty bounds, it calculates important sets, including the safe set $\mathcal{S} \subset \mathcal{P}$, the expander set $\mathcal{E} \subset \mathcal{P}$ and the minimizer set $\mathcal{M} \subset \mathcal{P}$. While fundamentally a Bayesian Optimization algorithm, safeOpt distinguishes itself by incorporating safety criteria throughout the entire iterative process.

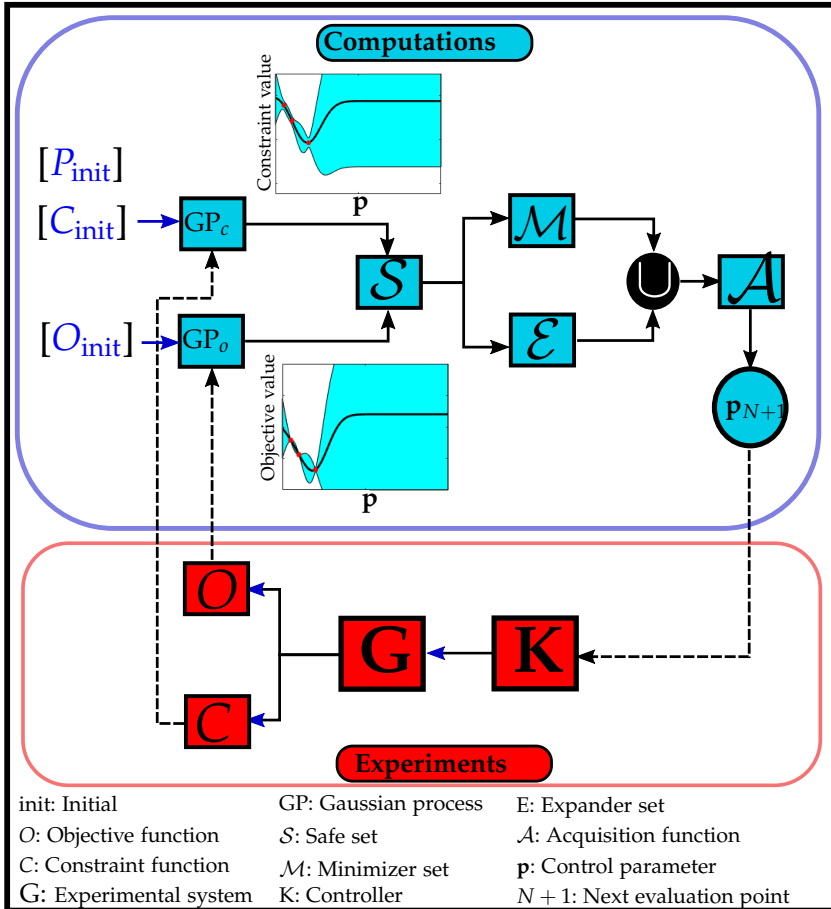


FIGURE 3.1: Visualization of the safeOpt algorithm: Gaussian process regressors model system responses at various control parameter values. Leveraging uncertainty bounds, the algorithm computes safe minimizer and expander sets. The union of these sets is input to an acquisition function, determining the next evaluation point. Objective and constraint function values are fed back to update the GPs.

During each iteration, the algorithm seeks to identify the optimum point within the current safe set or expand the size of the safe set. This trade-off between exploration and exploitation is managed by selecting the point with the highest uncertainty in the objective function value. This ensures

the adherence to additional safety criteria beyond optimizing the entire domain.

The safe set \mathcal{S} is obtained by looking at the upper confidence bound of the GP estimate of the constraint function $U_n^c = \mu_n^c + 2\sigma_n^c$, and taking the points which are below the threshold value T :

$$\mathcal{S}_n = \mathcal{S}_i \cup \{\mathbf{p}' \in \mathcal{P} \mid U_n^c(\mathbf{p}') < T\} \quad (3.8)$$

The choice of $2\sigma_n^c$ can be roughly interpreted as guaranteeing the safety with 95% probability per iteration.

The potential minimizers which compose the minimizer set \mathcal{E} is obtained by looking the upper bound of the objective function $U_n^o = \mu_n^o + 2\sigma_n^o$ and the lower bound of the objective function $L_n^o = \mu_n^o - 2\sigma_n^o$ which are inside the safe set \mathcal{S}_n that satisfies the following:

$$\mathcal{M}_n = \{\mathbf{p} \in \mathcal{S}_n \mid L_n^o(\mathbf{p}) < \min_{\mathbf{p}' \in \mathcal{S}_n} U_n^o(\mathbf{p}')\} \quad (3.9)$$

which implies that the potential minimizers are the points in the safe set whose current lower bound estimate of the objective function is lower than the best upper bound.

Following [111], in order to define the expander set \mathcal{E}_n , an indicator function e_n is first defined as follows:

$$e_n(\mathbf{p}) = |\{\mathbf{p}' \in \overline{\mathcal{S}_n} \mid U_{n,(\mathbf{p}, L_n^c(\mathbf{p}))}^c(\mathbf{p}') < T\}|, \quad (3.10)$$

where $U_{n,(\mathbf{p}, L_n^c(\mathbf{p}))}^c$ is the upper bound estimate of the constraint function based on the n measurement points and an artificial measurement of $(\mathbf{p}, L_n^c(\mathbf{p}))$. The indicator function $e_n(\mathbf{p})$ computing the size of the previously unsafe sets $\overline{\mathcal{S}_n}$ that could potentially become safe if one hypothetically evaluated the point \mathbf{p} and measured $L_n^c(\mathbf{p})$ as the constraint function value. The expander set is therefore defined as:

$$\mathcal{E}_n = \{\mathbf{p} \in \mathcal{S}_n \mid e_n(\mathbf{p}) > 0\}. \quad (3.11)$$

Essentially, the expander set comprises of the points that could potentially enlarge the current safe set.

The next evaluation point \mathbf{p}_{n+1} is acquired by taking the most uncertain point across the objective function which are inside the union of the potential minimizer set and the expander set:

$$\mathbf{p}_{n+1} = \arg \max_{\mathbf{p} \in \mathcal{E}_n \cup \mathcal{S}_n} U_n^o(\mathbf{p}) - L_n^o(\mathbf{p}). \quad (3.12)$$

The chosen acquisition function is widely known as "maximum uncertainty". The choice of the acquisition function will lead to a more exploratory behavior initially, which is caused by the fact that the most uncertain element typically lies on the boundaries of the safe region. Once the points close to the safety threshold T are evaluated, the algorithm will evaluate the points in the potential minimizer and potential expanders alternatively. The proposed safeOpt algorithm is summarized in Algorithm 1.

For demonstration purposes, the algorithm is tested by performing an optimization in a one-dimensional space $\mathcal{P} \subset [0, 10]$. The domain \mathcal{P} is discretized with 200 points, an objective function, featuring two minima and a constraint function containing one minimum, are selected as follows:

$$\begin{aligned} O &= 100(3 \sin(2(p+1)^{0.8}) - 0.4p + 7) \\ C &= \frac{10}{(p+2)^{0.4}} + 0.1(p-3)^2 - 4 \end{aligned} \quad (3.13)$$

The performance of the algorithm is depicted in figure 3.2. Note that the initial points for the algorithm are close to the first minimum point in

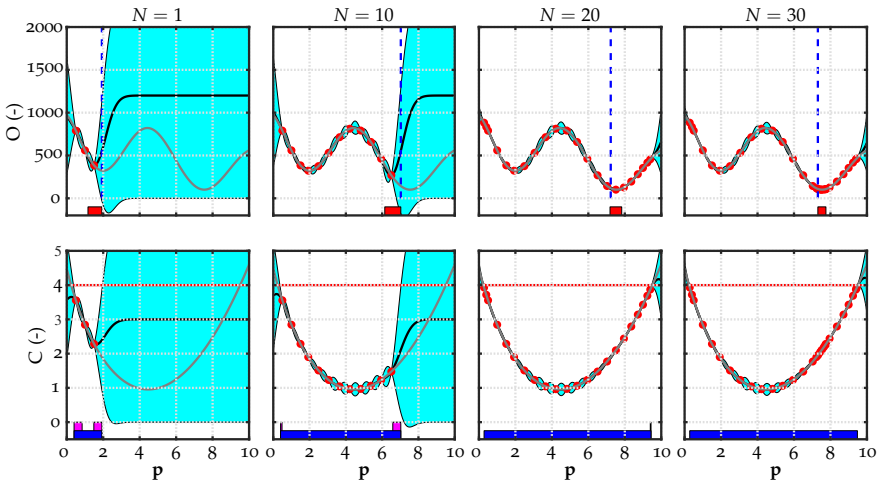


FIGURE 3.2: Demonstration Safe Optimization (safeOpt) algorithm after 1,10,20 and 30 iterations. (—): safe set, (—): minimizer, (—): expander, (—): mean prediction, (—): next evaluation point, (●): measurement points, (—): safety constraint, (—): real curve. The uncertainty of the prediction (2σ) is represented by the cyan shaded region.

the objective function which is not the global optimum. An optimization algorithm that relies on the local gradient of the function, such as the Extremum Seeking Controller (ESC), will easily be trapped in the first minimum. The algorithm spends the first 10 iterations to safely explore the parameter space. After about 20 iterations, the points with the constraint function value close to the threshold have been evaluated, and the algorithm starts evaluating a region around the global minimum within the domain.

Note that, as mentioned before, the algorithm will try to find the optimum location which is reachable from the initial safe set \mathcal{S}_i . Hence, the algorithm might encounter a problem when the safe set in the parameter space comprises of some disjoint sets and the initial safe set \mathcal{S}_i does not contain some of the disjoint sets. To illustrate this issue, the same objective function is kept and the constraint function in equation 3.13 is modified as follows:

$$\begin{aligned}
 O &= 100(3 \sin(2(p + 1)^{0.8}) - 0.4p + 7) \\
 C &= \frac{10}{(p + 2)^{0.4}} + 0.1(p - 4)^2(1 - 0.7 \sin(0.55p)) - 4
 \end{aligned}
 \tag{3.14}$$

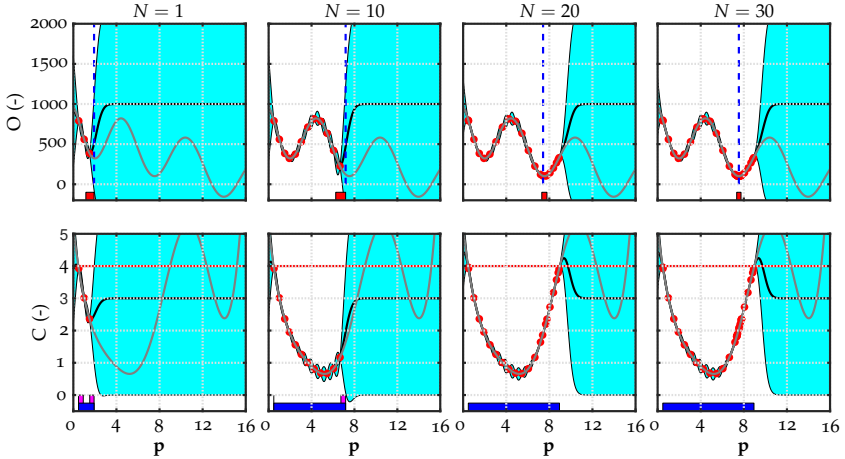


FIGURE 3.3: Demonstration Safe Optimization (safeOpt) algorithm with disjoint safe sets (see equation 3.14) after 1,10,20 and 30 iterations. (—): safe set, (—): minimizer, (—): expander, (—): mean prediction, (—): next evaluation point, (•): measurement points, (—): safety constraint, (—): real curve. The uncertainty of the prediction (2σ) is depicted by the cyan shaded region.

Algorithm 1 safeOpt Algorithm

Require:

- Control parameters domain \mathcal{P}
 - GP kernel for the objective and constraint functions
 - GP prior mean constants K^o and K^c
 - Safety threshold T
 - Initial safe set \mathcal{S}_i \triangleright In this study, it is generated by evaluating N_{init} initial points
- for** $N = 1, \dots, N_{max}$ **do**
- Find \mathcal{S}_n (eq. 3.8)
 - Get potential minimizer set (eq. 3.9)
 - Get possible expander set (eq. 3.11)
 - Get the next evaluation point \mathbf{p}_{n+1} (eq. 3.12)
 - Obtain $\hat{O}(\mathbf{p}_{n+1})$ and $\hat{C}(\mathbf{p}_{n+1})$ through measurement
 - Update GPs with the new measurement data.
- end for**
- Select the best evaluated points \mathbf{p}^*
-

The parameter space is now from 0 to 16, $\mathcal{P} \subset [0, 16]$. The constraint function is slightly modified so that there are two disjoint safe sets in the whole domain. The performance of the safeOpt algorithm in this situation is shown in Figure 3.3. As can be seen, there are two safe regions in the domain $\mathcal{S} \subset [0.5, 9], [12.5, 15]$. Using the same initial safe set and hyperparameters, the algorithm is able to find the same minimum point safely. However, because the global minimum at $\mathbf{p} = 14$, is located in the second safe region, which is not reachable from the initial information in \mathcal{S}_i , the algorithm cannot reach it. However, if \mathcal{S}_i included some points in the neighborhood of the global minimum, then the algorithm could have found the global minimum. Such a situation could indeed occur in an experimental setting; unless the algorithm is allowed to explore some unsafe point during the iterations or the initial safe set includes some points in all disjoint safe sets, the global minimum in the domain may not be uncovered. Nevertheless, the safeOpt algorithm will optimize the control parameter safely.

3.2.4 Modifications of safeOpt

Two types of modifications are proposed to adapt the algorithm to be more suited for thermoacoustic control. The modifications are named stageOpt

and the shrinkAlgo. The stageOpt algorithm follows the one presented in [118]. It works by splitting the exploration and exploitation parts separately. In this study, the safeOpt algorithm is set to work until n_s iterations. The superiority of SafeOpt is used initially to minimize and explore the objective function safely; afterwards, the acquisition function in iteration $n_s + 1$ is changed to the minimum lower confidence bound (LCB):

$$\mathbf{p}_{n+1} = \min_{\mathbf{p} \in \mathcal{S}_i} \mu(\mathbf{p}) - 2\sigma(\mathbf{p}) \quad (3.15)$$

The second modification involves incorporating a threshold in the objective function itself to give a second constraint. For the first n_s iterations, safeOpt with a single constraint on the constraint function will be employed, afterwards a second constraint on the objective function T_o is applied. The additional constraint would change the safe set and shrink its size. Therefore, it is named "Shrinking" algorithm and abbreviate it as shrinkAlgo. More formally, the safe set after n_s iterations is defined as:

$$\mathcal{S}_n = \{\mathbf{p}' \in \mathcal{P} | U_n^c(\mathbf{p}') < T \cap U_n^o(\mathbf{p}') < T_o\}. \quad (3.16)$$

The motivation behind this is due to the fact that during the exploration phase, the algorithm could still evaluate points with high objective function values to enlarge the safe set. This situation could be undesirable if one wants to minimize the pressure pulsation as this will lead to the operating the system under high pulsation condition for long duration. Additionally, the computation of the expander set could be skipped to restrict the exploration of the points in the minimizer set, hence the choice of the next evaluation points can be written as follows:

$$\mathbf{p}_{n+1} = \arg \max_{\mathbf{p} \in \mathcal{S}_n} U_n^o(\mathbf{p}) - L_n^o(\mathbf{p}). \quad (3.17)$$

The choice of skipping the computation of the expander is optional, it could be done if the user is confidence that the current minimizer set could perform well and only fine exploration is required. The two proposed modifications are summarized in Algorithms 2 and 3.

3.2.5 Bayesian Context

Bayesian context is a framework that allows us to model the dependency of the approximated functions with respect to additional external parameter(s) which are called context variables \mathbf{z} [119]. The idea is to include

Algorithm 2 stageOpt Algorithm

```

for  $N = 1, \dots, N_s$  do
  Follow algorithm 1
end for

for  $N = N_{s+1}, \dots, N_{max}$  do
  Find  $\mathcal{S}_n$  (eq. 3.8)
  Get potential minimizer set (eq. 3.9)
  Get possible expander set (eq. 3.11)
  Get the next evaluation point  $\mathbf{p}_{n+1}$  (eq. 3.15)
  Obtain  $\hat{O}(\mathbf{p}_{n+1})$  and  $\hat{C}(\mathbf{p}_{n+1})$  through measurement
  Update GPs with the new measurement data.

end for
Select the best evaluated points  $\mathbf{p}^*$ 

```

Algorithm 3 shrinkAlgo Algorithm

```

for  $N = 1, \dots, N_s$  do
  Follow algorithm 1
end for

for  $N = N_{s+1}, \dots, N_{max}$  do
  Find  $\mathcal{S}_n$  (eq. 3.16)  $\triangleright$  Safe set shrinks due to additional constraint
  Get potential minimizer set (eq. 3.9)
  if Use Expander is TRUE then
    Get possible expander set (eq. 3.11)
    Get the next evaluation point  $\mathbf{p}_{n+1}$  (eq. 3.12)
  else
    Get the next evaluation point  $\mathbf{p}_{n+1}$  (eq. 3.17)
  end if
  Obtain  $\hat{O}(\mathbf{p}_{n+1})$  and  $\hat{C}(\mathbf{p}_{n+1})$  through measurement
  Update GPs with the new measurement data.

end for
Select the best evaluated points  $\mathbf{p}^*$ 

```

the functional dependence and to keep it fixed when selecting the next

points to evaluate [112]. In the thermoacoustic context, this could be a small change in operating points such as fuel flow, air flow, and hydrogen blending level. Assuming that the frequency of the oscillation does not change significantly, the information from the previously optimized parameters in another condition can be transferred to the current one. This could speed up the optimization process as the previously information can be seen as measurement points with enlarged uncertainties. The dependence on the external parameter is modeled by creating a new kernel $k_c(\mathbf{z}, \mathbf{z}')$ which will be multiplied by the kernel over the parameters defined in eq. (3). The total kernel is then defined as follows:

$$k([\mathbf{p}, \mathbf{z}], [\mathbf{p}', \mathbf{z}']) = k(\mathbf{p}, \mathbf{p}') \times k_\phi(\mathbf{z}, \mathbf{z}'). \quad (3.18)$$

Hence, assuming one has evaluated the objective and constraint functions and approximated them with GP at the context variable \mathbf{z} , the information can be carried out to the next context variable \mathbf{z}' . The uncertainty will be enlarged depending on the kernel values of $k_\phi(\mathbf{z}, \mathbf{z}')$.

3.3 EXPERIMENTAL SETUP

3.3.1 Single stage combustor

The cut view of the experimental setup can be seen in Figure 3.4. The experimental setup is similar to that in chapter 4. The experimental setup consists of an inlet plenum, adjustable inlet orifice, a loudspeaker, an axial swirler, and an adjustable piston at the end of the test rig. The ducts are made up of $250 \text{ mm} \times 62 \text{ mm} \times 62 \text{ mm}$ modules which are connected in

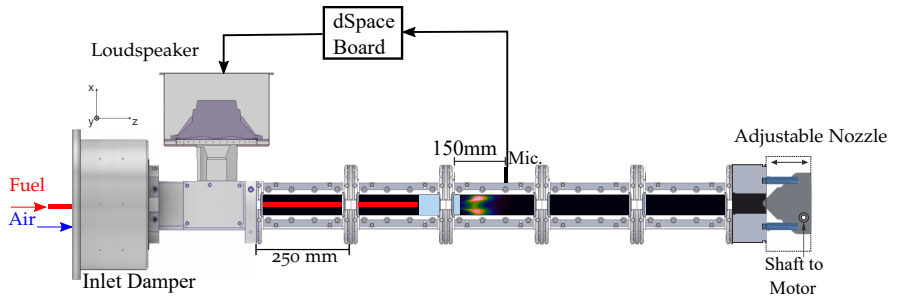


FIGURE 3.4: Side view of the experimental setup. A loudspeaker is placed inside of an enclosure upstream of the burner.

OP	\dot{m}_{CH_4} [g/s]	\dot{m}_{H_2} [g/s]	\dot{m}_{air} [g/s]	ϕ [-]	f_o [Hz]
1	0.57	0.02	15.35	0.684	200
2	0.64	0.01	15	0.753	180
3	0.44	0.05	16	0.575	230

TABLE 3.1: Operating conditions for single stage combustor setup. f_o denotes the instability frequency.

series. The adjustable piston at the end of the test rig allows for a variation of the outlet orifice area. The presence of both inlet and outlet adjustable orifices allows the adjustment of the nominal thermoacoustic stability of the setup. A microphone is placed inside a water-cooled flush mounted plate in the combustion chamber module. In the technically premixed mode, the air is injected from the inlet plenum module whereas the fuel, which is a mixture of H_2 and CH_4 , is injected from the lance and delivered through 8 small holes downstream of the axial swirler inside the burner.

The signal from the microphone is connected to a dSpace board (DS1104) where the controller is programmed to give an output voltage signal for the loudspeaker. In this study, the gain delay controller is employed; hence, the manipulation consists of delaying the microphone by τ milliseconds and multiplying the signal by a gain n .

Three different operating conditions are considered, and they are enumerated as OP₁, OP₂, and OP₃. The summary of important quantities for each operating condition is summarized in table 3.1. The instability frequencies for all operating conditions are around 200 Hz.

3.3.2 Sequential combustor

The lab-scale sequential combustor is depicted in figure 3.5. The setup consists of a plenum, a 4×4 array of jet flames anchored on a matrix burner, a combustion chamber with a cross section of $62 \times 62 \text{ mm}^2$, a dilution air section, a sequential burner featuring a mixing channel with a cross section of $25 \times 38 \text{ mm}^2$, a sequential or second-stage combustion chamber equipped with a motor-driven adjustable outlet orifice. This variable outlet geometry enables an online tuning of the acoustic reflection coefficient, and thus an independent control of the thermoacoustic instabilities, which is key for validating the NRPD-based control.

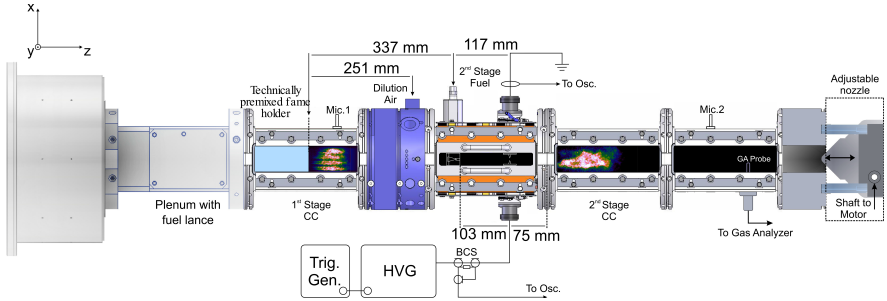


FIGURE 3.5: Lab-scale sequential combustor test-rig. CC- Combustion chamber, HVG- High Voltage Generator, BCS- Back Current Shunt.

The first stage combustor is fed with a mixture of natural gas and air, with the air preheated to 230°C and supplied from the plenum. A piezo sensor is placed on a flush mounted plate to monitor the acoustic pressure inside the first stage and denoted as Mic. 1 in the figure. A massflow of 18 g/s of dilution air at 25 C is introduced from the dilution air port and mixes with the hot gases from the first stage. A mixture of hydrogen and natural gas is injected into the sequential injector. The sequential injector features an X-shaped vortex generator to enhance the mixing process. The total thermal power of the two flames is 73.4 kW . A pin-to-pin electrode configuration, with an inter-electrode distance of 5 mm , is located 10.3 cm downstream from the sequential fuel injector, and a gas analyzer probe is placed at 45 cm from the outlet of the second-stage burner to monitor the NO emissions. Another piezo sensor is placed downstream of the sequential flame to monitor the acoustic pressure pulsation in the second combustion chamber. The exhaust gas analysis is conducted using an ABB EL3040 gas analyzer equipped with an Uras26 infrared photometer, operating at a sampling rate of 1 Hz . Automatic calibration with integrated calibration cells and sealing tests of the propagation line were performed before the start of each measuring set. The device exhibits a relative extended uncertainty of 7.9% for NO measurements within the range of $0\text{--}200\text{ mg/m}^3$.

3.4 THERMOACOUSTIC NETWORK MODEL

The safeOpt algorithm is first tested in a numerical setup, where the lab scale single stage combustor in figure 3.4 is modeled with low order thermoacoustic network model. The network diagram is shown in figure 3.6. The

purpose of this study is not to model exactly each subsystem, the acoustic boundaries, flame transfer functions, and the pressure losses across the area expansions are tuned so that the system becomes unstable at around 200 Hz, which is the instability frequency of the setup. The network formulation follows the one presented in [42, 120].

Each duct element is modeled as a perfect one-dimensional acoustic wave guide with velocity perturbations, u' , as input, and normalized acoustic pressure fluctuations $p'/(\rho c)$ as output. The acoustic perturbations can then be decomposed as forward- and backward-propagating waves, and expressed as follows:

$$\frac{p'}{\rho c} = f + g \quad (3.19)$$

$$u' = f - g, \quad (3.20)$$

where ρ and c are the gas density and the speed of sound, respectively.

The area jumps are modeled as compact area discontinuities with an equivalent length of L_{eq} and a mean flow velocity in the orifice \bar{U}_n . By denoting $(\cdot)_d$, $(\cdot)_u$, $(\cdot)_n$ as the acoustic quantities downstream, upstream of the area jump element, and inside the orifice, respectively, the governing equations can be written as:

$$A_d u'_d = A_u u'_u = A_n u'_n \quad (3.21)$$

$$\frac{p'_d - p'_u}{\rho c} - \frac{\bar{U}_n}{c} \zeta u'_n = \frac{L_{eq}}{c} \frac{du'_n}{dt}. \quad (3.22)$$

The equations above are widely known as $L - \zeta$ model.

The flame is modeled as a compact element and isentropic assumption is employed for the components upstream and downstream of the flame. By using the Rankine-Hugoniot relation and linearizing to get the acoustic perturbations, the resulting flame transfer matrix can be written as:

$$\begin{bmatrix} (\frac{p'}{\rho c})_d \\ u'_d \end{bmatrix} = \begin{bmatrix} \frac{(\rho c)_d}{(\rho c)_u} & 0 \\ 0 & 1 + (\frac{T_d}{T_u} - 1)FTF(\omega) \end{bmatrix} \begin{bmatrix} (\frac{p'}{\rho c})_u \\ u'_u \end{bmatrix} \quad (3.23)$$

where T_d and T_u are the temperature downstream and upstream of the flame respectively. Note that the T_{12} and T_{21} elements above are equated to zero due to the low Mach number assumption. The Flame Transfer Function $FTF(\omega)$ is modeled with a first-order low-pass filter with a delay τ_f :

$$FTF(\omega) = \frac{\exp(-i\omega\tau_f)}{i\frac{\omega}{\omega_b} + 1}, \quad (3.24)$$

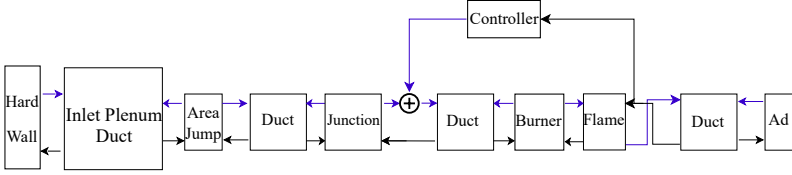


FIGURE 3.6: The thermoacoustic network model diagram. The blue arrow denotes the acoustic velocity perturbation u' , and the black arrow denotes the normalized acoustic pressure perturbation $p' / (\rho c)$. Ad is the downstream admittance boundary. The network model is implemented in MATLAB Simulink.

where $\omega = 2\pi f$ is the angular frequency, and ω_b the bandwidth of the low pass filter. For the time domain simulation, a tangent hyperbolic saturation function on the velocity perturbations upstream of the flame is utilized to saturate the amplitude of the downstream acoustic pressure fluctuations.

The loudspeaker is modeled as a velocity perturbation located on the plenum side. Utilizing the pressure continuity in the junction element and the mass conservation, the relation between the acoustic quantities upstream and downstream of the junction is written as follows:

$$p'_u = p'_d \quad (3.25)$$

$$u'_u = u'_d + u'_{LS}, \quad (3.26)$$

where u'_{LS} is the acoustic velocity perturbations generated by the loudspeaker. Note that, the loudspeaker cavity and the electro-acoustic properties of the loudspeaker need to be taken into account if one wants to properly simulate the loudspeaker response as demonstrated in [121, 122]. However, it is not done in the numerical experiment performed in this section of the paper since this study does not aim to quantitatively reproducing the dynamics observed experimentally.

The controller takes the signal of the normalized acoustic pressure perturbations $p' / (\rho c)$ downstream of the flame and then delays it by τ milliseconds and multiplies it by a gain n , the signal is then placed into a saturation block, $L[a] = a$ for $|a| < 5$ and $L[a] = \text{sgn}(a) \times 5$ when $|a| \geq 5$, so that the final output is bounded between -5 and 5 . This saturation function represents the threshold voltage that is applied in the experiments to protect the loudspeakers from breaking due to high voltage values. The voltage output is then converted to u'_{LS} by multiplying by a static gain,

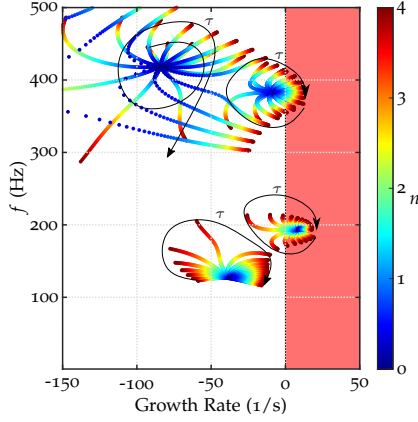


FIGURE 3.7: Maps of the eigenvalues of the system with varying gain (n) and the time delay (τ) of the gain-delay controller. The red shaded region indicates the linearly unstable region.

K_{LS} , of -0.6 . More precisely, the voltage and velocity perturbations of the loudspeaker are expressed as:

$$V_{LS} = L \left[n \times \left(\frac{p'(t - \tau)}{\rho c} \right)_d \right] \quad (3.27)$$

$$u'_{LS} = K_{LS} V_{LS} \quad (3.28)$$

It is worth mentioning that real loudspeakers will always have an effective frequency bandwidth in which the membrane will vibrate most efficiently. Since this behavior is not modeled in our case, all frequencies will pass through the loudspeaker without any attenuation. Hence it will be more probable in this numerical experiment that another acoustic mode is excited. By varying both parameters (n and τ), the system eigenvalues can be changed and will eventually shift all eigenvalues to the stable region. Figure 3.7 shows the eigenvalues variation with respect to changes in both n and τ of the controller. As seen, the unstable poles are around $f = 200$ Hz and 400 Hz.

3.5 RESULTS

In this section, the applications of the proposed algorithms are presented in both numerical and experimental settings. Section 3.5.1 discusses the

results obtained in the numerical setup, while Section 3.5.2 shows the results from the experiments. In the numerical setup, only the safeOpt algorithm (Algorithm 1) is employed, while, in the experimental setup with loudspeakers, all algorithms are employed. For both setups, optimization starts first with one parameter and then with two parameters.

3.5.1 Numerical validation

For the gain-delay controller, the associated length scale L in eq. (3.5) can be cast into the following form:

$$\mathbf{L} = \begin{bmatrix} l_n & 0 \\ 0 & l_\tau \end{bmatrix} \quad (3.29)$$

where l_n is the length scale of the gain parameter and l_τ is the length scale of the time delay parameter.

First, only one parameter is optimized, which in this case is the gain n . The time delay of the controller is fixed at 1.55 ms. The objective function is the root mean square of the pressure pulsation after the flame, and the constraint function is the root mean square of the loudspeaker voltage. Both quantities are computed over a period of five seconds. Three initial points are fed to the algorithm, the initial points are $n = \{-1.5, 0, 3.5\}$, the initial safe set \mathcal{S}_i is then obtained by fitting a Gaussian Process Regressor (GPR) to both the objective and the constraint function values. The domain of control parameters \mathcal{P} , which in this case contains only the n , is discretized by 100 uniform grid points from -1.5 to 4. The hyperparameters are listed in table 3.2. The length scale and the prior variance of the kernel of the

Hyperparameters	O	C	O	C
	(n Opt)	(n Opt)	($n - \tau$ Opt)	($n - \tau$ Opt)
θ [Pa - V]	450	0.65	450	0.65
l_n [-]	0.2	0.4	0.2	0.4
l_τ [ms]	-	-	0.75	0.75
σ [Pa - V]	15	0.05	30	0.05

TABLE 3.2: Hyperparameters of the Gaussian Process Regressors. Opt: optimization, O: objective function, C: constraint function

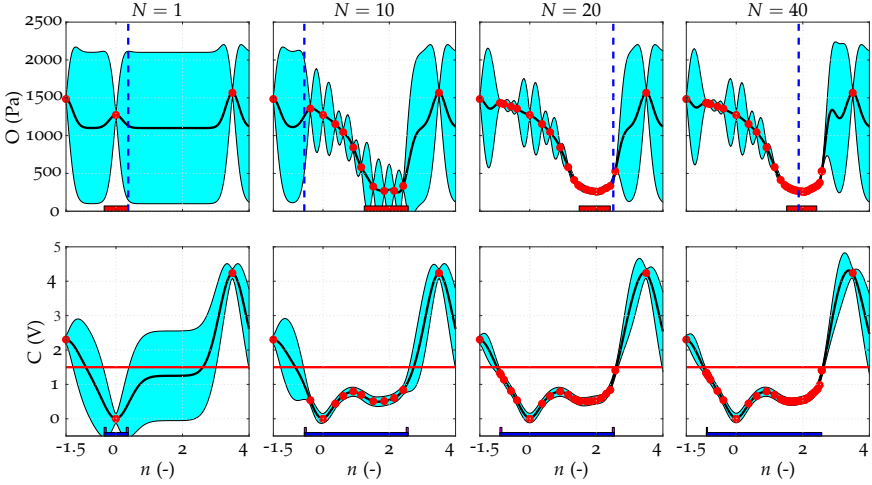


FIGURE 3.8: Controller n optimization with safeOpt after 1,10,20 and 40 iterations, the time delay, τ , is fixed at 1.55 ms. (■): safe set, (—): minimizer, (—): expander, (—): mean prediction, (---): next evaluation point, (●): measurement points, (—): safety constraint. The cyan-shaded region represents the uncertainty of the prediction (2σ). The global optimum of the objective function is already found within 10 iterations.

objective function $k^o(n, n')$ are set to 0.2 and 450 respectively. This can be interpreted that a distance of gain around 0.2-0.4 would yield completely different behavior, and the expected deviations from the mean value are 900 Pa. Whereas, the length scale and the prior variance of the kernel of the constraint function $k^c(n, n')$ are set to 0.4 and 0.65V, respectively. Noise variances σ_o and σ_c are set to 15 Pa and 0.05V, respectively.

The gain optimization of the $(n - \tau)$ controller from the thermoacoustic network model is shown in Figure 3.8. As seen, the algorithm can safely find the global optimum in 10 iterations. After 20 iterations, more points close to the optimal location are evaluated. Additionally, the algorithm also tries to expand the safe set during the process. The size of the safe set, as shown by the blue rectangle in the bottom plot, increases throughout the iterations until the 20th iteration. Subsequently, until the 40th iterations, the algorithm evaluates almost exclusively the region close to the minimum. In the simulation, the modes at 200 Hz and at 400 Hz can be excited depending on the value of n . Figure 3.9 shows the time trace, frequency spectra, and the histogram of the filtered acoustic pressure pulsation around

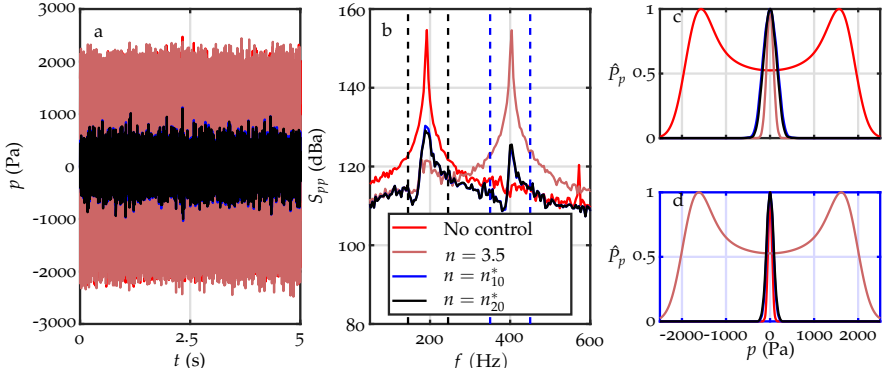


FIGURE 3.9: a) Simulated pressure time-trace and b) Power spectral density at four different gain values. $n = 3.5$ is the highest gain evaluated for the initial point. n_{10}^* and n_{20}^* denote the best evaluated n after 10 and 20 iterations. c) and d) The pressure histogram of the bandpass filtered acoustic signal around 200 and 400 Hz respectively, the bandwidth of the filtering is indicated by the dashed line in b).

the instability frequencies. Without any control action, the system is unstable and the instability frequency is 200 Hz. When the gain is equal to 3.5, the higher mode at around 400 Hz becomes self-excited. The best evaluated n after 10 and 20 iterations, denoted by n_{10}^* and n_{20}^* exhibit almost the same performance in terms of pressure pulsation. This indicates that, in principle, 10 iterations are enough to optimize the gain safely.

The optimization of the two control parameters optimization is shown in Figure 3.10. The domain of control parameters is a 50×50 uniform grid points with n spanning from 0 to 2.5 and the τ ranges from 0.5 ms to 7 ms, $\mathcal{P} \subset \mathbb{R}^{[0, 2.5] \times [0.5, 7]}$. All kernel parameters are set the same as in the case with n only optimization, with the addition of the length scale for τ . The length scale for τ in $k^0(\mathbf{p}, \mathbf{p}')$ is set to 0.4 ms, whereas for the $k^c(\mathbf{p}, \mathbf{p}')$ they are set to 1 ms. Because the mode at around 400 Hz could be excited and the number of control parameters is now two, more initial points are required to initialize the algorithm for the computation of \mathcal{S}_i . Note that, as previously mentioned, the initial safe set could be given directly by the user if the user has some preliminary information. Eleven initial points are given to the algorithm, six points are on the left and right boundaries of the domain, and five points are around the middle of the domain. The number of iterations is set to 34 iterations which then amounts to 45 evaluated points in the domain. The algorithm spends the first 17 iterations to expand

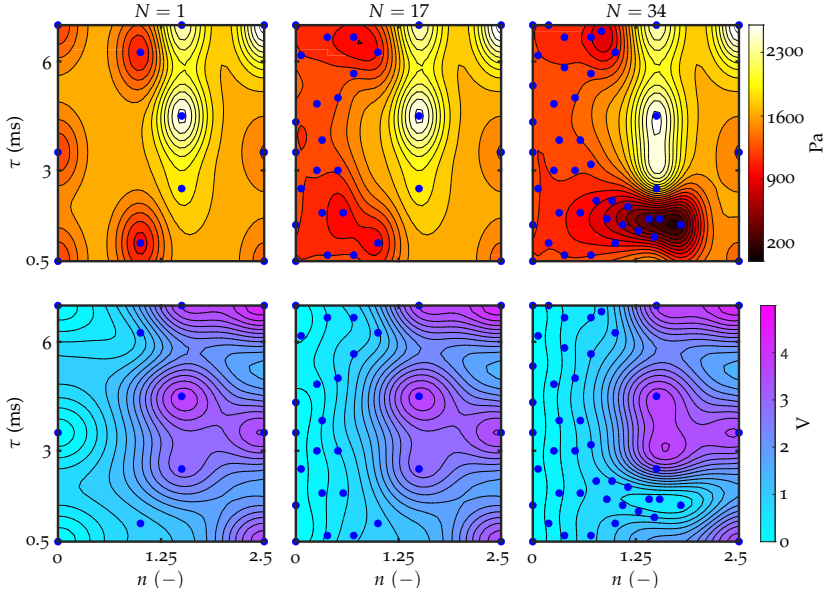


FIGURE 3.10: $n - \tau$ optimization with safeOpt algorithm after 1, 17, and 34 iterations. The mean prediction of the surface map of the objective function (top) and constraint function (bottom). (●): evaluation points.

the safe set and essentially evaluate the left half-plane of the domain. After reaching 17 iterations, the algorithm starts to evaluate points with low pulsations. The best evaluated point after 34 iterations is $(n, \tau) = (1.8, 1.5)$.

Despite the simplification of the thermoacoustic network model, the performance of the algorithm gives a preliminary indication that it could potentially work in the real system. The algorithm is applied to the experimental setup shown in figure 3.4 in the next section.

3.5.2 Experimental validation

3.5.2.1 Single-stage combustor with loudspeaker actuation

It is worth mentioning that, in contrast to the numerical simulation in Section 3.5.1, the experimental setup shown in Figure 3.4 only has one unstable acoustic mode over the whole control parameter space. Three operating conditions with different instability frequencies are considered and summarized in table 3.1. The three algorithms explained in Section

Hyperparameters	O	C	O	C
	(n Opt)	(n Opt)	($n - \tau$ Opt)	($n - \tau$ Opt)
θ [Pa - V]	450	0.65	450	0.65
l_n [-]	0.2	0.4	0.2	0.4
l_τ [ms]	-	-	0.3	1
σ [Pa - V]	15	0.05	30	0.075

TABLE 3.3: Hyperparameters of the Gaussian Process Regressors. Opt: optimization, O: objective function, C: constraint function

3.2 are employed and compared with each other. Similarly to Section 3.5.1, the algorithms are first tested with one parameter optimization and continue with two parameters optimization. Additionally, the Bayesian context algorithm in Section 3.2.5 is applied to transfer the knowledge between different operating conditions to enhance the convergence speed of the algorithm.

The hyperparameters for the Gaussian Process Regression (GPR) are detailed in Table 3.3. Notably, all values closely align with those employed in the numerical test cases. A specific adjustment is made for l_τ in the constraint function, where it is now configured to be 1 ms. This adjustment is made because of the presence of a single unstable mode, allowing for an expectation of a larger correlation distance. Furthermore, σ^c is set to 0.075 V intentionally to induce greater uncertainty in the measurements. This deliberate increase in uncertainty promotes a more conservative algorithmic behavior, thereby ensuring that the safety criterion is not violated.

The gain optimization of the gain-delay controller with safeOpt algorithm is shown in figure 3.11. Similarly to the numerical simulation, the control parameter space domain is discretized with 100 uniform grid points with n ranging from -1.5 to 4 . Three initial points are given at $n = \{-1.5, 0, 4.5\}$. Note that in this case, one of the initial points is not inside the considered domain. As the purpose of the initial points is only to construct the initial safe set \mathcal{S}_i , this will not create any problem. The root mean square of the acoustic pulsation and the loudspeaker voltage are calculated by recording both signals for five seconds and then applying the RMS operator. The safety threshold for the constraint function is $T = 1V$.

Similar to the numerical simulation, the algorithm initially spends the first 10 iterations expanding the safe set, as evident from the growth in

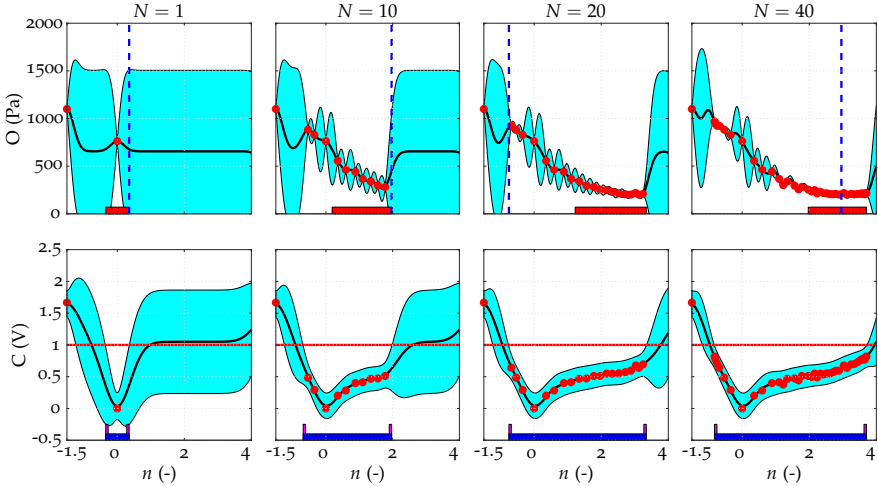


FIGURE 3.11: Controller n optimization at OP1 (see table 3.1) with safeOpt algorithm after 1,10,20 and 40 iterations, the time delay, τ , is fixed at 1.5 ms. (■): safe set, (●): minimizer, (■): expander, (—): mean prediction, (—): next evaluation point, (●): measurement points, (—): safety constraint. The cyan-shaded region depicts the uncertainty of the prediction (2σ).

its size. After these initial 10 iterations, the algorithm shifts its focus to evaluating points with low pulsation. It is worth noting that, in contrast to the numerical simulation, when the gain values fall within the range of 1.5 to 3.5, the resulting pressure root mean square (RMS) values are nearly identical. Figure 3.12 provides visual representations of the time trace, frequency spectra, and the scaled probability density function of the acoustic pressure signal. Specifically, Figure 3.12c illustrates that the system stabilizes after just 10 iterations with the best-evaluated value of “ n ”. However, after 20 iterations, a more favorable “ n ” in terms of pressure RMS is found.

As the iterations progress beyond 20, there is no improvement in pressure RMS. The algorithm continues to evaluate different values of “ n ”, but the pressure RMS remains the same, as indicated in Figure 3.11.

The inherent nature of the safeOpt algorithm involves a continuous trade-off between exploring or expanding the safe set and minimizing the objective function throughout all iterations. Consequently, the algorithm occasionally evaluates points with high RMS values, even when the optimal

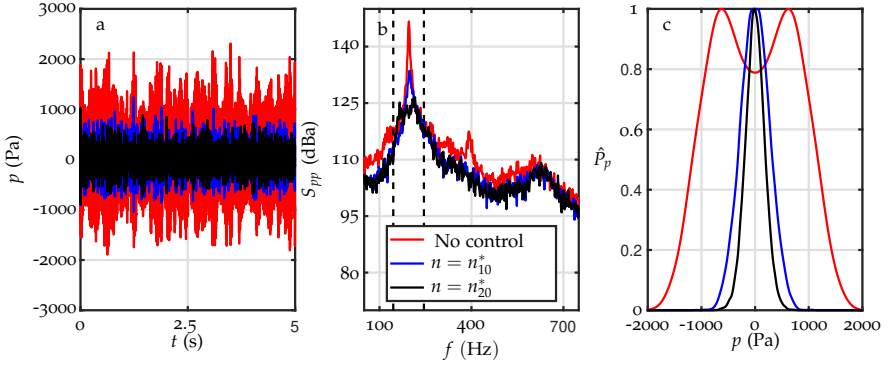


FIGURE 3.12: a) The pressure time-trace and b) Power spectral density at three different gain values. n_{10}^* and n_{20}^* denote the best evaluated n after 10 and 20 iterations, respectively. c) The pressure histogram of the bandpass filtered acoustic signal around 200 Hz, the filtering bandwidth is indicated by the dashed line in b).

point is unlikely to be found in this region. For example, in Figure 3.11, at the 20th iteration, the algorithm chooses a safe value of n which is likely to have a high objective function value. This characteristic can be advantageous in escaping local optima if they exist. However, it may be undesirable when such local optima are absent, resulting in the combustor operating with high pulsation with no tangible benefits. Therefore, to solve this issue, stageOpt and the shrinking algorithm, which are explained in Algorithm 2, and Algorithm 3, respectively, are used.

Figure 3.13 shows the results of the gain optimization with the shrinking algorithm. Following Algorithm 3, the first 10 iterations employ the regular safeOpt algorithm, at iteration $N_s = 11$, an additional constraint T_o is added to the objective function itself with a value of 450 Pa. Note that, in Figure 3.13, N is restarted to 1 once the additional constraint is applied. As seen, the additional constraint leads to a shrinkage of the safe set. Additionally, the expander is not used; however, as iterations progress, the safety set is still growing because the acquisition function is the maximum uncertainty as described in eq 3.17. In this case, the benefit is clear, the algorithm does not evaluate points with high pressure pulsations since these points are now classified as unsafe. Note that, if the additional constraint is applied too early in the iterations, it may not be able to find a safety set, as the points with pressure RMS value below the threshold T_o have not yet been found. These results highlight the flexibility of algorithms to incorporate

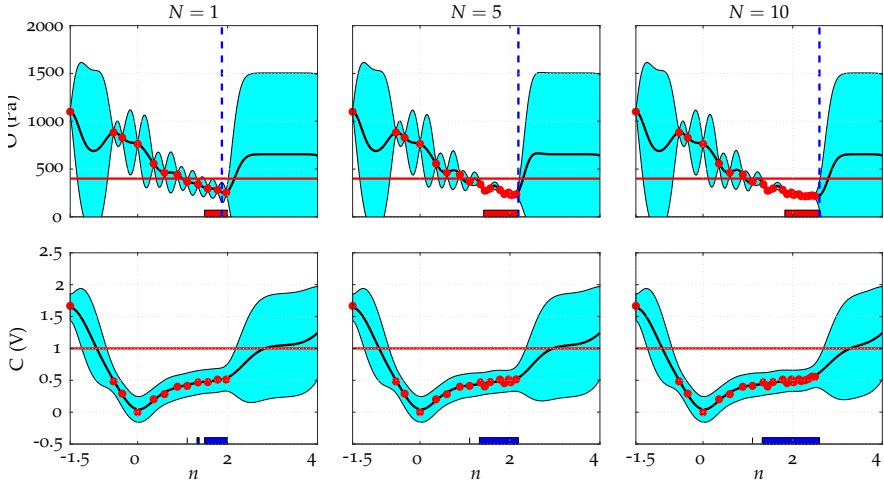


FIGURE 3.13: Controller n optimization at OP1 (see table 3.1) with shrinkAlgo after 1, 5, and 10 iterations. Note that N displayed has been restarted to 1 once the additional constrain was activated after the 11th iteration. The time delay, τ , is fixed at 1.5 ms. (■): safe set (the safe set fulfills both constraints on O and C), (■): minimizer, (—): mean prediction, (- -): next evaluation point, (●): measurement points, (—): safety constraint. Expander computation is excluded. The shrinking algorithm was activated after 10 iterations of SafeOpt. The safe set immediately shrinks after a secondary constraint on the objective function is applied.

additional constraints. In principle, multiple constraints can be used, the only modifications would be to add additional Gaussian process regressors and incorporate them in the calculation of the safe set.

The application of the stageOpt algorithm is shown in figure 3.14. Similarly to the shrinking algorithm, the first 10 iterations employ the safeOpt algorithm and then the acquisition function is switched to the minimum lower confidence bound of the objective function as described in eq. 3.15. After the switch of the acquisition function, it is clear that the algorithm always evaluates points with the lowest lower confidence bound, thereby, points with high pulsation values are not evaluated.

The evolution of the values of the objective function, the gain, and the constraint function, with the application of the three algorithms, is shown in Figure 3.15. Note that the safe constraints are indicated by the dashed

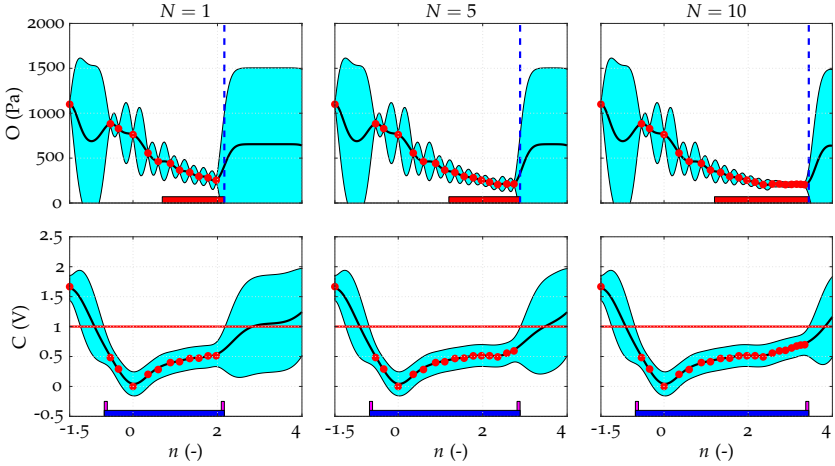


FIGURE 3.14: Controller n optimization with stageOpt algorithm after 1, 5, and 10 iterations. Note that N displayed has been restarted to 1 once the additional constrain was activated after the 11th iteration. The time delay, τ , is fixed at 1.5 ms. (—): safe set, (—): minimizer, (—): expander, (—): mean prediction, (—): next evaluation point, (●): measurement points, (—): safety constraint. The StageOpt algorithm was activated after ten iterations of SafeOpt. The algorithm always chooses the minimum of the lower confidence bound of the objective function for the next evaluation point.

line, and the constraint on the objective function is only applicable to the shrinking algorithm. As seen, in the 18th iteration, the safeOpt algorithm evaluates points with high pulsation. On the contrary, both the stageOpt and shrinking algorithms do not have this behavior. Due to the removal of the expander, the shrinking algorithm slowly expands the safe set, as can be seen by the slowly increasing gain after the 11th iteration. The choice of algorithms might depend on the system of interest and the user’s preference.

The Bayesian context is applied to transfer the knowledge obtained from OP2 to OP1. The safeOpt algorithm was first performed on OP2 for 15 iterations. Afterwards, the combustor is operated to OP1 and by adding a context variable, which in this case the equivalence ratio, $\mathbf{z} = \phi$, the information from OP2 can be transferred to OP1. The length scale for the kernel k_ϕ is set to 0.1, which implies that a 0.1 difference in the equivalence ratio will lead to completely different behaviors. Figure 3.16 shows the

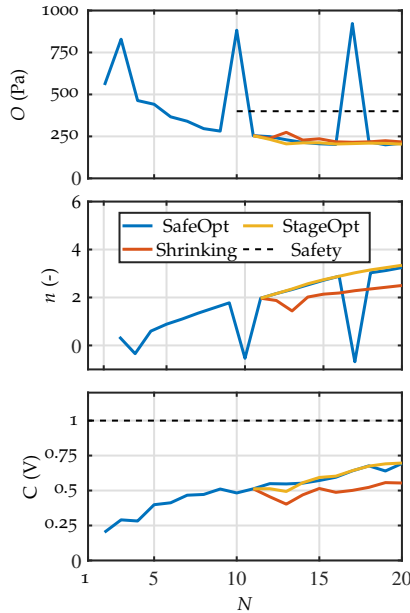


FIGURE 3.15: The evolution of the objective function, gain, and the constraint function with respect to the number of iterations. The safety constraint on the objective function is only applied to the shrinking algorithm. The first iteration contains no evaluation point.

results of the Bayesian context. The shrinking algorithm is used, and the threshold values are the same as in Figure 3.13. As seen, in the first iteration, the uncertainties in the objective and constraint function are scaled up. The algorithms are now more uncertain about the information collected from OP2, which is indicated by the (+) sign. This is due to the introduction of k_ϕ in the kernel function of both objective and constraint functions. Because of the possibility of transferring the information, the algorithm is now more sample-efficient as the points with low pulsation values are now known. This is a clear advantage as small changes in the operating conditions of the combustor will not require the algorithm to restart again from zero.

The framework is now extended to optimize both the n and τ parameters. The control parameter space is discretized uniformly with 50×50 grid points, with n ranging from 0 to 3.5 and τ ranging from 0.5 to 6 ms, $\mathcal{P} \subset \mathbb{R}^{[0 \ 3.5] \times [0.5 \ 3.5]}$. As a result of the increased number of parameters,

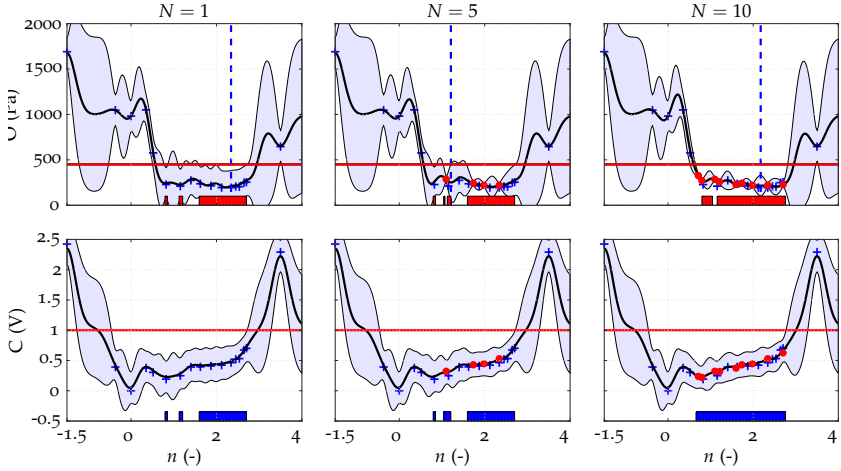


FIGURE 3.16: Context with shrinkAlgo after 1, 5, and 10 iterations. The algorithm makes use of the information obtained at OP2 to optimize the n at OP1. The time delay, τ , is fixed at 1.5 ms. (■): safe set, (■): minimizer, (—): mean prediction, (---): next evaluation point, (+): data points from OP2, (●): evaluation points, (—): safety constraint.

a greater number of initial points is required, similar to the case of the numerical simulation. Since there is only one unstable mode observed in the experiment, only six initial points are given. Figure 3.17 shows the mean prediction of the objective function \bar{u}_o and the constraint function \bar{c} . The initial points are shown in the first column of Figure 3.17. The safety threshold values T and T_o are the same as those in the one parameter optimization case. The total number of iterations is set at 30. For the first 15 iterations, the algorithm safely explores the parameter space and finds the two regions with low pulsations, as shown in the third column of Figure 3.17. The first safe region is located on the bottom left region, and the second one is on the top left region. This is possible because for a single-mode instability at a frequency of f_0 , two different time delays τ_2 and τ_1 that are related as $\tau_2 = \tau_1 + 1/f_0$ would give similar results because the phase of the controller is the same for these two delays. The algorithm evaluates more points in the bottom left region and the best evaluated point is located at $(n, \tau) = (1.25, 1.7)$.

The results obtained through the use of the shrinking algorithm to optimize the two parameters are presented in figure 3.18. In the initial 15 iterations, the algorithm employs the safeOpt approach, followed by the

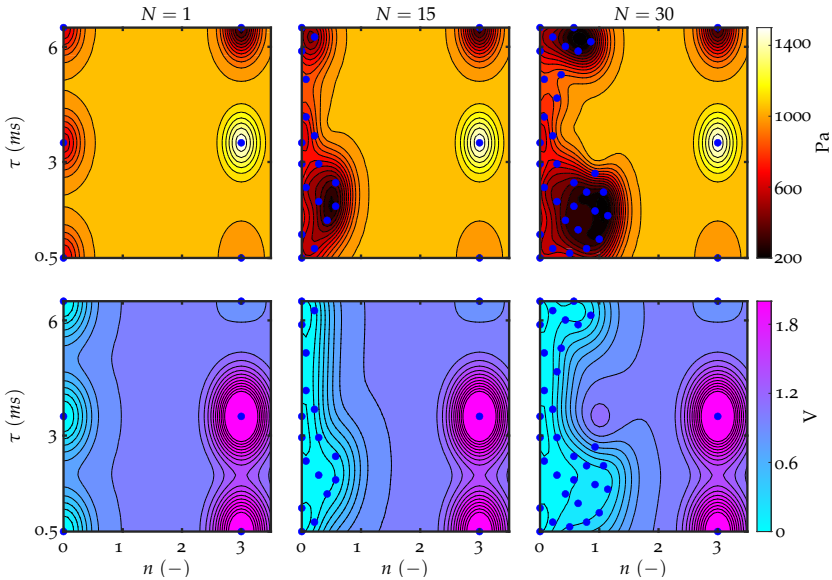


FIGURE 3.17: $n - \tau$ optimization with safeOpt algorithm after 1, 15, and 30 iterations. The mean prediction of the surface map of the objective function (top) and constraint function (bottom). (●): evaluation points. (OP₁)

introduction of an additional constraint applied to the objective function. Similarly to the previous scenario that involves single-parameter optimization, the expander is eliminated. This change results in a more constrained focus on evaluating points in the bottom-left region. Due to the absence of expanders, the assessed points in the lower left region are positioned closely together, significantly limiting the algorithm's ability to expand. Nevertheless, the safe-set region continues to grow throughout the iterations. It is important to note that the majority of the evaluated points exhibit thermoacoustic stability. However, they tend to have slightly higher root mean square (RMS) values compared to the best-evaluated point obtained with the safeOpt algorithm. One potential approach to enable more aggressive exploration would involve reintroducing the expander into the decision-making process for the next point evaluation. Nevertheless, the primary objective here is to illustrate that there can be drawbacks when the exploratory aspect is curtailed.

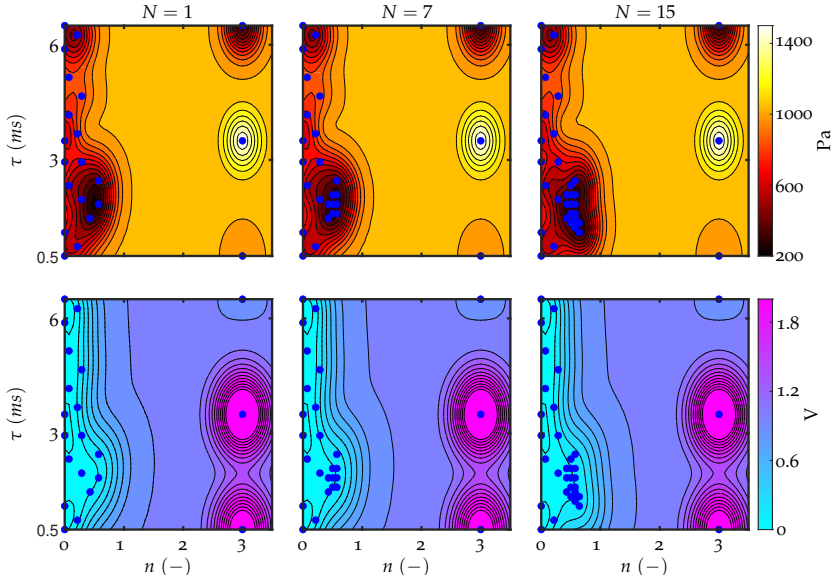


FIGURE 3.18: $n - \tau$ optimization with shrinkAlgo after 1, 7, and 15 iterations. The first iteration is taken from the 15th iteration of the safeOpt. The mean prediction of the surface map of the objective function (top) and constraint function (bottom). (●): evaluation points. The expansion of the parameter space becomes more restricted due to an additional constraint on the objective function.

The results obtained using the stageOpt algorithm are depicted in figure 3.19. Similarly to the shrinking algorithm, the initial 15 iterations employ the safeOpt algorithm for a cautious exploration of the parameter space. Similarly to the scenario involving single-parameter optimization, following the transition to a different acquisition function, the algorithm refrains from assessing points associated with high pulsation values. The stageOpt algorithm, however, evaluates regions with τ values akin to those targeted by the safeOpt algorithm, falling within the range of 0.5 to 2 milliseconds. Notably, the stageOpt algorithm extends its evaluations to higher gain values. This expanded exploration of the parameter space is facilitated because the alternative safe region, characterized by low pulsation values at τ around 6 milliseconds, remains unexplored. As a result, with an equal number of total iterations, the stageOpt algorithm efficiently allocates more iterations to the assessment of points in the lower left region of the domain.

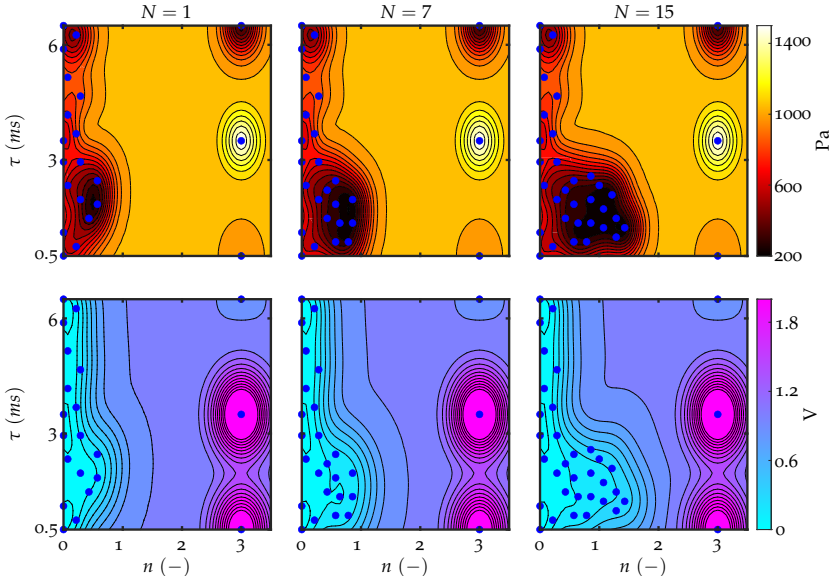


FIGURE 3.19: $n - \tau$ optimization with stageOpt algorithm after 1, 7, and 15 iterations. The first iteration is taken from the 15th iteration of the safeOpt. The mean prediction of the surface map of the objective function (top) and constraint function (bottom). (●) evaluation points. The algorithm picks more points on the lower left plane of the parameter space. (OP₁)

The figure 3.20 presents the progression of various parameters, including the objective function, gain n , delay τ , and the constraint function. It's evident from the graph that the safeOpt algorithm explores a region where τ is approximately 6.2 milliseconds, from iteration N 22 to 27. In contrast, both the stageOpt and shrinking algorithms consistently assess regions where τ is less than 2.5 milliseconds. This difference arises because, as mentioned earlier, within the first 15 iterations of the safeOpt algorithm, the region characterized by low objective function values with τ around 6.2 milliseconds has not yet been discovered. Consequently, both the stageOpt and shrinking algorithms remain unaware of this particular region. However, it's worth noting that the region with τ around 6.2 milliseconds is expected to yield performance similar to that of τ around 1.5 milliseconds. As a result, the stageOpt and shrinking algorithms do not suffer any disadvantages

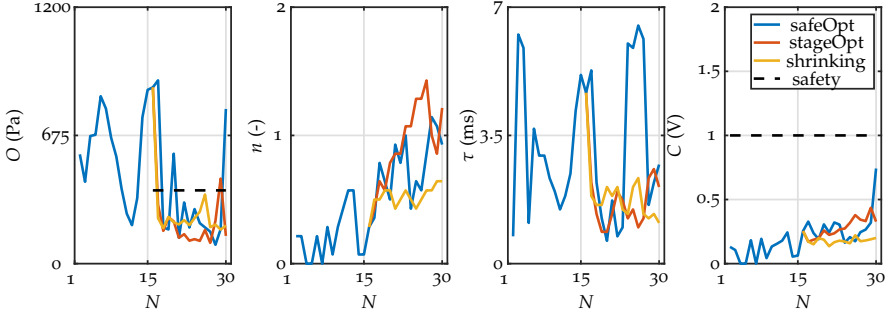


FIGURE 3.20: The evolution of the objective function, gain, and the constraint function with respect to the number of iterations. The safety constraint on the objective function is only applied to the shrinking algorithm. The first iteration does not contain an evaluation point.

in terms of failing to identify the global minimum, given that this region eventually provides equivalent performance.

In different scenarios, increasing the value of N_s in both Algorithm 3 and Algorithm 2 could provide a more comprehensive overview of the parameter space for the algorithm. However, it is important to emphasize that the choice of N_s is problem-specific and contingent on the particular case at hand. Consequently, users should establish their expectations before initiating the optimization process.

Bayesian context is applied for two-parameter optimization, and three operating conditions are considered. The shrinking algorithm is applied first to OP2 with the number of iterations equal to 30 and $N_s = 15$, the expander is used to acquire the next point evaluation. Subsequently, the information obtained from both OP2 and OP1 is transferred to OP3, and the shrinking algorithm with the total number of iterations set to 8 and $N_s = 1$ is applied. The kernel parameters of the objective and constraint functions, as well as the safety threshold values, are the same as in the previous case. The mean prediction of the objective function for the three operating conditions is shown in figure 3.21, whereas the normalized uncertainty of the objective function is shown in figure 3.22.

As can be seen from the first row of Figure 3.21, the algorithm can safely explore the parameter space and the evaluation points are less closely packed compared to the result in Figure 3.18. This is due to the inclusion of the expander in the shrinking algorithm which allows the algorithm to explore more aggressively while still respecting the safety threshold

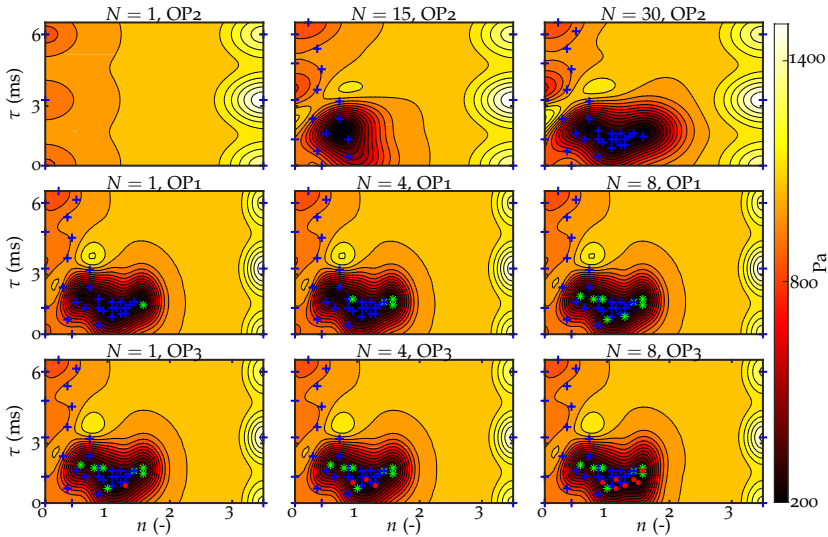


FIGURE 3.21: $n - \tau$ optimization with context. The algorithm uses the context variable to transfer the knowledge between each operating point. The mean predictions of the objective function from OP2, OP1, and OP3 are displayed in the second, first, and third rows, respectively. +: evaluation points from OP1, *: evaluation points from OP2, (●): evaluation points from OP3.

in both the objective and constraint functions. Because the frequency of the instability at OP2 is lower than at OP1, the other region with low pulsation values as in figure 3.17 lies outside the domain. After completing 30 iterations at OP2, the information is carried out to OP1 with the Bayesian context. As clearly seen from the second row of figure 3.21, the algorithm evaluates points in the vicinity where the previous operating point exhibits low pulsation and is safe.

Following the completion of eight iterations at OP2, the combustor transitions to OP3, with information from both OP2 and OP1 being carried over to OP3. In the graph displayed in figure 3.22, it becomes evident that, at OP3, the algorithm exhibits increased uncertainty regarding the information derived from OP2 in comparison to that from OP1. This heightened uncertainty is attributed to the fact that the context variable of OP1 is closer to OP2 than it is to OP3. A similar pattern emerges at OP3, where the algorithm now recognizes the safe region with low pulsations and consistently evaluates points within this low-pulsation region. While it is possible that

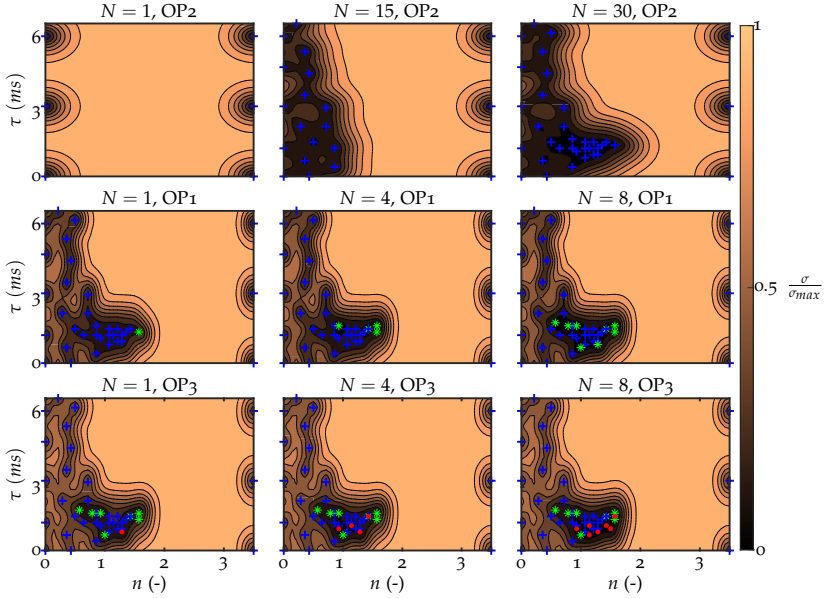


FIGURE 3.22: Map of the normalized uncertainty of the objective function for $n - \tau$ optimization with context. The algorithm uses the context variable to transfer the knowledge between each operating point. The mean predictions of the objective function from OP₁, OP₂, and OP₃ are displayed in the first, second, and third rows, respectively. $+$: evaluation points from OP₁, $*$: evaluation points from OP₂, \bullet : evaluation points from OP₃.

eight iterations may be insufficient for the algorithm to thoroughly explore the parameter space, the primary aim here is to illustrate that with the aid of Bayesian context, direct access to a safe region with low pulsation values can be achieved without the necessity of restarting the algorithm from scratch.

3.5.2.2 Sequential combustor with NRPD

In the sequential combustor configuration, the sequential flame is stabilized with the help of NRPD. The objective function is the NO emission in parts per million by volume, dry (ppmvd), and the constraint function is the RMS pressure in the sequential combustion chamber, measured by the mic. 2 in figure 3.5. The two control parameters are the voltage output of the high

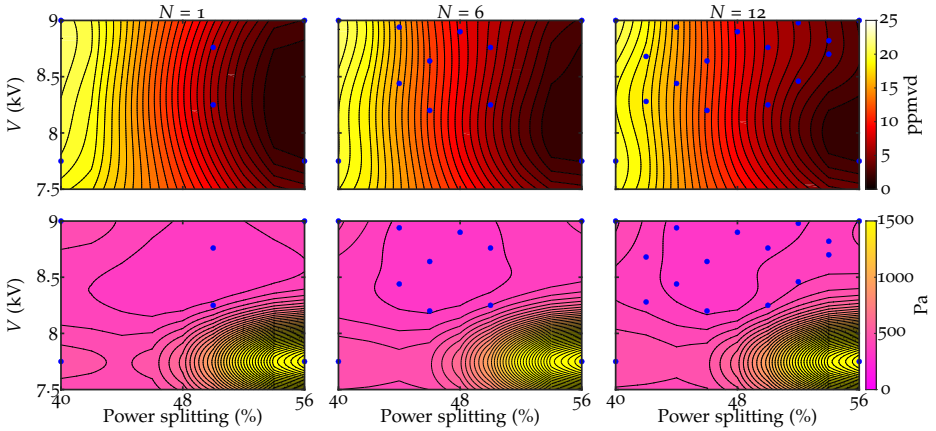


FIGURE 3.23: Bayesian optimization using shrinkAlgo. The objective function is the NO emissions, and the constraint function is the RMS pressure. (top) The mean prediction of the objective function. (bottom) The mean prediction of the constraint function. The blue dots show the evaluation points.

voltage generator and the allocation of power between both flames. It is important to note that the overall thermal power of the flames remains at a constant value of 73.4 kW, and the mass flow rates for both the first-stage air and dilution air are also maintained at a consistent level. The term "power splitting" is defined as the percentage representing the proportion of the total power directed towards the second stage flame. For example, if the power splitting is set to 60 %, this means that the second stage flame thermal power is 60% of the whole thermal power, which equates to 44.04 kW. Regarding the fuel composition, it is important to note that the first stage exclusively uses 100% natural gas, while the second stage employs a mixture consisting of 10.45% hydrogen and 89.55% natural gas by mass. The emission analyzer requires a continuous operation of about 100 seconds to converge, whereas, the RMS pressure is computed after recording the pressure signal for five seconds.

The control parameter space is discretized with the power splitting ranging from 40% to 56% with a step of 2%, whereas the generator voltage is from 7.5 kV to 9 kV, with 100 points in between. The length scale matrix L is now written as:

Hyperparameters	O	C
θ [ppmvd - Pa]	15	300
l_V [kV]	0.5	0.5
l_{PS} [%]	2	2
σ [ppmvd - Pa]	1.2	20

TABLE 3.4: Hyperparameters of the Gaussian Process Regressors.

$$\mathbf{L} = \begin{bmatrix} l_V & 0 \\ 0 & l_{PS} \end{bmatrix} \quad (3.30)$$

where l_V is the length scale of the plasma generator voltage and l_{PS} is the power splitting. The hyperparameters are listed in Table 3.4.

The shrinkAlgo algorithm is utilized and six initial points are used to get the initial safe set for the algorithm. The initial points can be seen in the first column of figure 3.23. The safety threshold for the pressure RMS is set at 500 Pa, and the safety threshold for the NO emission, which is active only after 8 iterations ($N_s = 8$), is 10 ppmvd. As can be seen, a power splitting of 56% with a voltage of 7.75 kV exhibits low NO emissions but high amplitude acoustic pressure. Therefore, this point is classified as unsafe. As the iteration progresses, the algorithm safely explores the control parameter space by evaluating the region in the middle of the domain. Afterward, the algorithm evaluates the region on the top right part of the domain. After 12 iterations, the optimization process is terminated, and the safe minimum point is found at a power split of 56% and voltage of 9 kV. As mentioned in [110], the application of NRPD can significantly alter the mean sequential flame position and its heat release rate response to acoustic perturbations, which subsequently affect the thermoacoustic stability of the whole system. However, the main objective of this study is to optimize the control parameters solely, and the discussion about the stabilization mechanism will be investigated in a separate study.

These results highlight the flexibility of the algorithm in optimizing different control parameters for thermoacoustic control. The control structure does not have to be affine feedback control based; as demonstrated here, the NRPD is operated in a continuous fashion without feeding the pressure signal to the controller as in the previous section. Moreover, the versatility of the algorithm extends to the straightforward inclusion of addi-

tional constraint variables, such as exhaust temperature, carbon monoxide (CO) emissions, and so on. These variables can be readily incorporated as constraint functions by configuring Gaussian Process Regression with appropriately tuned kernel parameters. Furthermore, NRPD equipped with the proposed algorithms is shown to be an effective actuator for controlling both the pulsation of a sequential combustor and accessing operating conditions with low NO emissions.

3.6 CONCLUSIONS AND OUTLOOK

This study has effectively showcased the practicality of employing safe Bayesian optimization algorithms for thermoacoustic control. Three distinct algorithms, specifically tailored for thermoacoustic systems, were introduced and implemented, demonstrating their efficacy through numerical simulations and experimental applications. In all setups, the algorithm does not employ any model and relies on the obtained measurements to update the regressors.

In the first phase, encompassing both numerical simulations and the first experimental setup, the adaptive optimization of feedback control parameters within a single-stage combustor utilizing loudspeaker actuation is illustrated. These proposed algorithms facilitate the transfer of knowledge between varying operating conditions, resulting in a significant acceleration of the optimization process.

In the second experimental scenario, the same algorithm was applied to a sequential combustor using nanosecond repetitive pulsed discharges (NRPD). This setup differs significantly from the previous one in terms of combustor architecture, control actuation, and safety criteria, yet the proposed algorithms proved to be versatile and effective across these diverse contexts.

ACKNOWLEDGMENTS

This chapter is based on the paper “*BOATS: Bayesian Optimization for Active control of ThermoacousticS*”, by Bayu Dharmaputra, Pit Reckinger, Bruno Schuermans, and Nicolas Noiray, submitted to the Journal of Sound and Vibration in December 2023. This project has received funding from the European Research Council (ERC) under the European Union’s Horizon 2020 research and innovation program (grant agreement No [820091]) TORCH (2019-2024).

ENTROPY TRANSFER FUNCTION MEASUREMENT WITH TUNABLE DIODE LASER ABSORPTION SPECTROSCOPY

Do not stop to think about the reasons for what you are doing, about why you are questioning. The important thing is not to stop questioning. Curiosity has its own reason for existence.

— Albert Einstein

Tunable diode laser absorption spectroscopy (TDLAS) combined with wavelength modulation spectroscopy (WMS) is a proven method for measuring gas temperature and species concentration in combustion environments, making it ideal for assessing temperature fluctuations in the mixing section of a sequential burner. In this chapter, the TDLAS-WMS is studied and developed. This chapter employs TDLAS-WMS to measure coherent temperature fluctuations in a turbulent swirled flame, a setup less complex than that of the sequential combustor. Two distributed feedback (DFB) lasers target H₂O absorption near 7185.59 cm⁻¹ and 6806.03 cm⁻¹. The absorption signal is converted to temperature at a rate of 5 kHz. The focus of this chapter is on the Entropy Transfer Function (ETF), which at low Mach numbers links upstream acoustic perturbations to downstream temperature fluctuations, at three different operating conditions. This chapter presented novel results on the peculiar entropic response of a turbulent swirled frame at high frequencies.

4.1 INTRODUCTION

Unsteady processes in the reactive flow of turbulent combustors give rise to the generation of entropy fluctuations in the hot combustion products [123]. Along with vorticity and compositional perturbations, they are responsible for the generation of indirect combustion noise [123, 124]. Indirect noise has been a significant concern in modern jet engines since it contributes to the noise emission of the engines [125]. Furthermore, when entropy fluctuations result from coherent flame dynamics due to the thermoacoustic interaction, coherent temperature fluctuations, known as entropy waves, can be generated [126]. If the waves do not significantly disperse in the turbulent flow of the hot products and survive until the combustion chamber outlet,

and if this outlet exhibits a high Mach number, acoustic energy is produced at the corresponding frequency [127], which can substantially enhance the coherent flame dynamics. This phenomenon can constitute a key feedback mechanism for some thermoacoustic instabilities [33]. The presence of entropy waves might stabilize and destabilize the thermoacoustic dynamics of a combustor, as demonstrated in [128]. Therefore, understanding the principle of the generation and transport of entropy waves is essential.

Some experimental studies have recently been published concerning the transport and dispersion of entropy waves. Giusti et al. [129] measured the entropy waves generated by a turbulent flame with thermocouples placed in the combustion chamber. However, the thermocouples could only measure the coherent fluctuations up until 80 Hz. Wassmer et al. [130] measured the temperature fluctuations of a swirled flame with an acoustic time of flight approach by employing a spark plug protruding the combustor's wall and seven microphones equally distributed along the circumference of the can combustor wall. De Domenico et al. [131] measured entropy waves propagation using Laser-Induced Thermal Grating Spectroscopy. More recently, Weilenmann et al. [126] performed an experimental study on the linear and non-linear ETF in a turbulent combustor with OH laser-induced fluorescence (LIF) thermometry. However, in that case, the temperature measurement method is unsuitable for analysing a wide range of operating conditions since the data are cross-sectional; hence, it consumes a large amount of storage and requires tedious post-processing treatment. Wang et al. [132] measured the entropy waves of a turbulent swirled flame with tunable diode laser absorption spectroscopy (TDLAS) using the direct absorption spectroscopy (DAS) method. However, the DAS method is less sensitive than the wavelength modulation spectroscopy (WMS) method [133], and it will be further explained in the remaining of this paper.

This study aims at introducing the TDLAS-WMS for entropy waves measurements which offers several advantages: (i) TDLAS is a pointwise line-of-sight thermometry, and hence the data size is compact; (ii) the temperature can be inferred from the absorbance data in an accurate manner; (iii) the measurement rate in the order of kHz and MHz can be achieved; (iv) in contrast to the DAS method, the WMS does not require a baseline fitting, provides higher sensitivity and is more robust against non-absorption losses [133, 134].

The TDLAS-WMS method has been widely applied to combustion diagnostics to measure temperature, species concentration, pressure, and velocity in practical combustors [133, 134, 135, 136]. It has been proven to be

robust for in-situ combustion diagnostics with high accuracy and sensitivity. More recently, Mathews et al. [137] demonstrated that the measurement rate of TDLAS-WMS can be tuned to the MHz level and enables precise measurements in particle laden combustion environments.

The TDLAS's ability to measure time-resolved temperature fluctuations is exploited in this work. We record coherent temperature fluctuations of a turbulent swirled flame. The flame is acoustically perturbed by actuating a loudspeaker, which generates equivalence ratio fluctuations and induces temperature fluctuations downstream of the flame. By relating the temperature fluctuations to the acoustic perturbation input, the entropy transfer function (ETF) is obtained.

Key objectives of this study are to measure ETF with the TDLAS-WMS technique and to show that the measured entropy transfer functions do not decrease monotonically with respect to the forcing frequency.

4.2 EXPERIMENTAL SET-UP

4.2.1 *Turbulent Combustor*

The schematic of the turbulent combustor setup is shown in Figure 4.1a. The setup consists of 1) a plenum section composed of three modules whose dimensions are $250 \times 62 \times 62 \text{ mm}^3$, 2) a burner with axial swirler and central lance for flame anchoring, 3) a combustion chamber comprising four modules of the same kind as for the plenum, some of them featuring quartz windows, others water-cooled aluminium walls, two of them being equipped with special optical ports for TDLAS measurements, 4) two loudspeakers mounted on the walls of the most upstream and downstream combustor modules, and 5) 14 flush-mounted water-cooled GRAS microphones distributed upstream and downstream of the burner and the flame. The combustor outlet is equipped with an adjustable orifice to ensure thermoacoustically stable conditions. The optical access for the laser beam, which is denoted as TDLAS-LOS (Line-of-Sight) and sketched in Figure 4.1, is enabled through two wedged windows mounted on the sidewalls and located 28 cm downstream of the burner outlet. This distance corresponds to approximately four times the flame height.

A sketch of the burner block is shown in Figure 4.1b, it consists of a central lance with a diameter of 20 mm with an axial swirler inserted in cylindrical section of diameter 34.5 mm, creating an annular section into which swirled air and gaseous fuel are mixed. The fuel, which consists

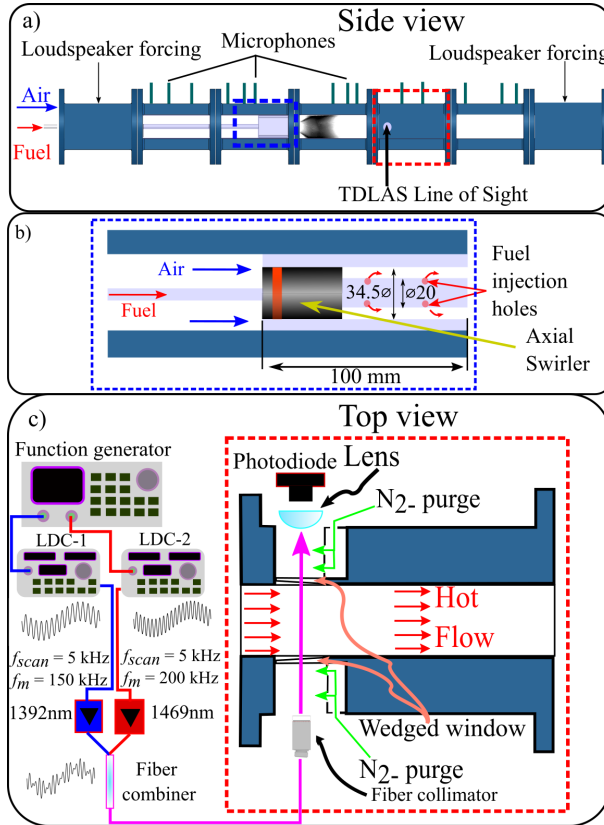


FIGURE 4.1: a) Schematic of the turbulent flame experimental setup for ETF and FTF measurements. b) Sketch of the swirler block. All dimensions are in mm. Stiff-injection of the fuel and mixing are done inside the block. c) Schematical arrangement of the optical setup for TDLAS.

of a mixture of natural gas and hydrogen, is delivered through the lance and injected from 8 small holes which are axially staged at two different locations (4 at 50 mm and 4 at 22 mm from the burner outlet). The diameter of each hole is 0.8 mm, creating an acoustically stiff injection for the gas mass flows considered in this work. The air is injected at the plenum inlet and mixes with the fuel inside the burner.

The flame of this technically premixed configuration is forced with the loudspeakers in order to measure the ETF and the FTF. For ETF measurements, only the upstream loudspeaker is actuated. The acoustic velocity

perturbation at the burner inlet is reconstructed from the microphones upstream of the flame. For FTF measurements, both the upstream and downstream loudspeakers are used to actuate the flame. The flame transfer matrix is then reconstructed from the multi-microphone method (MMM), with six microphones upstream and eight microphones downstream of the flame.

4.2.2 Optical Setup

The optical system for TDLAS is sketched in Figure 4.1c. Two infrared diode lasers (DFB-NEL) centered at 1392 nm and 1469 nm are used to probe the absorption spectra of water vapour around 7185.59 cm^{-1} and 6806.03 cm^{-1} , respectively. The current is supplied by laser diode controllers (LDC 501m), which are modulated by a function generator (Tektronix AFG31000). The laser emitting near 1392 nm and 1469 nm are sinusoidally scanned at 5kHz and modulated at 150 kHz and 200 kHz with modulation depths of 0.09 cm^{-1} and 0.092 cm^{-1} , respectively. The combinations of the two wavelengths have been widely used in the literature to infer the temperature of gases, see [133, 137, 138]. The laser beam from both lasers is then combined with a fiber combiner and subsequently collimated to a beam diameter of 3 mm with a fiber collimator (Thorlabs F280APC-C). Two optical windows with a wedge angle of 2° enable the emitted beam to probe the hot products of the flame. It is worth mentioning that the wedge angle is required to eliminate etalon interference. The gap (4 cm) between the fiber collimator and the optical window is purged with N_2 to minimize background absorptions from the water vapour under room conditions. The partially absorbed beam then goes through another N_2 -purged gap and is then collimated further with a convex lens and detected by a photodiode (Thorlabs PDA05CF2). The signal of the photodiode is sampled at 20 MS/s with a 16-bit data acquisition card (GaGe).

4.3 METHODOLOGY

4.3.1 Laser Absorption Spectroscopy (LAS)

LAS is based on the absorption spectrum of the chemical species under investigation at particular wavelengths [139]. When a laser light passes through a gas sample, a fraction of it is absorbed by the absorbing species. If the laser's wavelength is modulated (by modulating the supplied current

to the laser), typically, several transition lines will be covered. As a result, the contributions of different absorption lines have to be taken into account. The absorption can be modeled using Beer-Lambert's law:

$$\begin{aligned}\tau[\nu(t)] &= \exp\left(-\int_0^L \sum_{j=1}^N S_j(T)\phi_j[\nu(t)]PX_a dl\right) \\ &= \exp\left(-\alpha[\nu(t)]\right)\end{aligned}\quad (4.1)$$

where $\tau[\nu(t)]$ is the ratio between the transmitted laser intensity I_t and the incident laser intensity I_o , $S_j(T)$ is the j^{th} transition linestrength at temperature T , ϕ is the transition lineshape, L is the absorption path length, ν is the wavenumber, P is the pressure and X_a is the mole fraction of the absorbing species, and α is the absorbance. The lineshape ϕ is modeled by a voigt function that considers two broadening types: collisional broadening and Doppler broadening. Note that the dependencies of ϕ with respect to T , P and X_a are not explicitly defined in equation (4.1).

4.3.2 Wavelength Modulation Spectroscopy (WMS)

In the WMS method, the laser light is modulated with a modulation frequency f_m , thereby encoding the absorption information to f_m and its harmonics. In this work, we employ the same calibration-free WMS strategy as in [133]; therefore, only a brief summary of WMS is presented here.

When the laser current is sinusoidally modulated, both the wavelength emitted by the laser as well as the incident laser intensity will vary with respect to time. The wavelength variation is modeled as:

$$\nu(t) = \bar{\nu} + a_m \cos(\omega_m t) \quad (4.2)$$

where a_m is the modulation depth, $\bar{\nu}$ is the mean laser wavelength, and $\omega_m = 2\pi f_m$ is the angular frequency of the modulation signal. The parameters are a priori identified with a Fabry-Perot interferometer (Thorlabs SA30-144). The laser intensity is modeled by taking into account the fundamental and the first harmonic component of the sinusoidal signal:

$$\begin{aligned}I_o(t) &= \bar{I}_o [1 + i_1 \cos(\omega_m t + \delta_1) \\ &\quad + i_2 \cos(2\omega_m t + \delta_2)]\end{aligned}\quad (4.3)$$

where \bar{I}_o is the average laser intensity, i_1 and i_2 are the amplitude of the fundamental and first harmonic of the nonlinear intensity modulation (normalized by the average laser intensity \bar{I}_o), respectively. δ_1 and δ_2 are the

phase shifts between the wavelength modulation and the fundamental and first harmonic component of the nonlinear intensity modulation, respectively. The parameters are also identified a priori by passing the laser beam into a nitrogen purged duct and fit the measured intensity signal with equation (4.3).

The absorption process can be modeled by expressing the transmission coefficient $\tau(t)$ in terms of Fourier cosine series spanned by the harmonics of the modulation frequency as:

$$\tau[v(t)] = \sum_{k=0}^{\infty} H_k(\bar{v}, a_m) \cos(k\omega_m t) \quad (4.4)$$

where the H terms can be numerically calculated by projecting the simulated transmission coefficient to the corresponding cosine basis.

As a result, the transmitted laser intensity, $I_t = I_o(t)\tau[v(t)]$, will also contain the higher harmonics. By multiplying the transmitted laser intensity with a reference cosine, $\cos(k\omega_m t)$, and subsequently applying a low-pass filter, the in-phase component, X_{kf} , of the signal can be obtained. Similarly, multiplication with a reference sine, $\sin(k\omega_m t)$, would recover the quadrature component, Y_{kf} , of the signal.

Using Eqs. (4.3) and (4.4), the X_{1f} and Y_{1f} components can be derived analytically:

$$\begin{aligned} X_{1f} = G \frac{\bar{I}_o}{2} & \left[H_1 + i_1 \left(H_0 + \frac{H_2}{2} \right) \cos(\delta_1) \right. \\ & \left. + \frac{i_2}{2} \left(H_1 + H_3 \right) \cos(\delta_2) \right] \end{aligned} \quad (4.5)$$

$$\begin{aligned} Y_{1f} = -G \frac{\bar{I}_o}{2} & \left[i_1 \left(H_0 - \frac{H_2}{2} \right) \sin(\delta_1) \right. \\ & \left. + \frac{i_2}{2} \left(H_1 - H_3 \right) \sin(\delta_2) \right], \end{aligned} \quad (4.6)$$

where G is the electro-optical gain of the system, which does not have to be measured or known, as a normalisation procedure will be done in the next step. Similarly, by changing the reference cosine and sine into $\cos(2\omega_m t)$ and $\sin(2\omega_m t)$, the X_{2f} and Y_{2f} can be obtained:

$$\begin{aligned} X_{2f} = G \frac{\bar{I}_o}{2} & \left[H_2 + \frac{i_1}{2} \left(H_1 + H_3 \right) \cos(\delta_1) \right. \\ & \left. + i_2 \left(H_0 + \frac{H_4}{2} \right) \cos(\delta_2) \right] \end{aligned} \quad (4.7)$$

$$Y_{2f} = -G \frac{\bar{I}_0}{2} \left[\frac{i_1}{2} \left(H_1 - H_3 \right) \sin(\delta_1) + i_2 \left(H_0 - \frac{H_4}{2} \right) \sin(\delta_2) \right] \quad (4.8)$$

The magnitude of the nf component of the transmitted laser intensity is then obtained by taking the root sum-square between X_{nf} and Y_{nf} :

$$R_{nf} = \sqrt{X_{nf}^2 + Y_{nf}^2}. \quad (4.9)$$

By taking the ratio between R_{2f} and R_{1f} , the dependency on G is canceled out. Note that the background signals due to nonlinear intensity modulation and/or background absorption have to be subtracted from the absorption signals:

$$R_{2f/1f} = \left(\left[\left(\frac{X_{2f}}{R_{1f}} \right)_{\text{raw}} - \left(\frac{X_{2f}}{R_{1f}} \right)_{\text{bg}} \right]^2 + \left[\left(\frac{Y_{2f}}{R_{1f}} \right)_{\text{raw}} - \left(\frac{Y_{2f}}{R_{1f}} \right)_{\text{bg}} \right]^2 \right)^{\frac{1}{2}} \quad (4.10)$$

where the sub-script “raw” and “bg” denote the corresponding filtered signal obtained from the raw absorption signal with and without the presence of the absorbance, respectively. In the simulation step, the “bg” terms are obtained by simulating zero absorption signal. The “raw” terms are obtained by simulating the absorption signal at relevant gas conditions.

In order to increase the robustness of the method against wavelength drift of the laser [137], an additional sinusoidal signal with a lower frequency than the modulation signal is supplied to the laser. The additional frequency is denoted as scanning frequency, f_{scan} . Therefore, the laser intensity parameters \bar{I}_0 , i_1 , and i_2 in equation (4.3) will also vary in time. Hence, they have to be measured at the point where the peak of R_{2f} occurs. The laser’s wavelength will have an additive component due to the sinusoidal scan, however, the a_m is assumed to be unaffected.

The simulated $R_{2f/1f}$ spectra of water vapour with uniform gas composition and at relevant gas conditions for wavenumber around 7185.59 cm^{-1} and 6806.03 cm^{-1} are shown in Figure 4.2a and 4.2b, respectively. The simulation requires some spectroscopic parameters (e.g., linestrengths at reference temperature, broadening coefficients, temperature exponents), which have been experimentally determined in [138]. The simulation takes

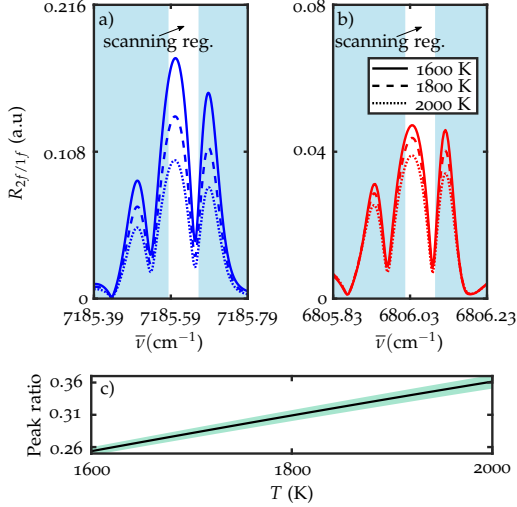


FIGURE 4.2: Simulated WMS($2f/1f$) spectra of H_2O for transitions centered around a) 7185.59 cm^{-1} and b) 6806.03 cm^{-1} at a relevant gas condition for the current study with $X_{\text{H}_2\text{O}} = 0.185$, $P = 1 \text{ atm}$, and $L = 6.2 \text{ cm}$. The unshaded regions depict the scanning region swept by the laser. c) The ratio between the peak of $R_{2f/1f}$ at around 6806.03 cm^{-1} and 7185.59 cm^{-1} . The shaded region corresponds to the uncertainty due to the uncertainties in the spectroscopic parameters from the database.

into account different laser's center wavelength $\bar{\nu}$ to emulate the effect of the scanning signal. The scanning range of the lasers are depicted in the unshaded region in Figure 4.2. Note that since the scanning signal used in this study is sinusoidal, the same wavelength range will be swept during the upward and downward direction of the scan denoted as upscan and downscan, respectively.

The $R_{2f/1f}$ ratio of the two different peaks are then computed and shown in Fig 4.2c. As seen, the peak ratio varies linearly in this case. Note that the linearity depends on the temperature range and the laser's parameters.

The uncertainties in the spectroscopic parameters, which are indicated in the database, propagate further to the final peak ratio and hence to the inferred temperature. The uncertainty region is plotted in Fig 4.2c. This information will be used in the subsequent analysis to quantify the error in the temperature inference.

The gas temperature can be inferred by taking the ratio between the peak of $R_{2f/1f}$ at around 6806.03 cm^{-1} and 7185.59 cm^{-1} from the measurement and then comparing it to that of the model. Although the $R_{2f/1f}$ peak ratio is insensitive to the mole fraction of water vapour, the individual $R_{2f/1f}$ of each laser varies proportionally with the mole fraction of water vapour. Therefore, for the temperature inference process, an iterative procedure is applied by providing an initial guess of the mole fraction to the model, calculating the temperature with the simulation, updating the mole fraction, and repeating the process not more than twice. The TDLAS-WMS method has been validated with plasma emission spectroscopy measurement in [68].

4.3.3 Entropy Transfer Function

Through the linearized thermodynamic relations and a low Mach number assumption, which is valid in the present configuration, the temperature fluctuations are linked to the entropy perturbations as follows, provided that the acoustic-induced (isentropic) temperature fluctuations are negligible [47, 140]:

$$\frac{T'}{\bar{T}} = \frac{s'}{c_p'} \quad (4.11)$$

where the $(\cdot)'$ and $\overline{(\cdot)}$ denote the small perturbation and the mean value of the quantities. In the case of technically premixed flame, temperature fluctuations downstream of the flame are generated by the equivalence ratio fluctuations produced upstream of the flame front [141].

The resulting equivalence ratio fluctuations at the fuel injection location are a function of the acoustic velocity perturbations at the burner inlet:

$$\frac{\phi'}{\bar{\phi}} = F\left(\frac{u'}{\bar{u}}\right) \quad (4.12)$$

If the region of the fuel injection is convectively compact, that is, the resulting fluctuations are uniform with respect to the distance at the relevant frequency range, the right-hand side simplifies to $-u'/\bar{u}$. In our setup, although the injection holes are distributed at two different axial positions, the distance between them can still be considered as convectively compact for the operating conditions and the frequency range of interest. The equivalence ratio perturbations are then convected to the burner outlet and might exhibit a complex frequency dependency as described in [142].

Nevertheless, we are interested in the relation between the temperature fluctuations downstream of the flame to the acoustics perturbation input at the inlet of the burner. We then define the ETF as:

$$\text{ETF}(\omega) = \frac{T'/\bar{T}}{u'/\bar{u}} \quad (4.13)$$

where $\omega = 2\pi f$ is the angular frequency. T' and \bar{T} are measured at 28 cm from the burner outlet. The choice of this location is motivated by the following reasons: First, it must be sufficiently far from the recirculation zone. Second, it should give enough temperature fluctuations such that they can be measured. Third, the contribution of entropy waves to the indirect and direct noise is significant only if they survive until the end of the combustor. The measurement location is approximately four flame heights which is close to the typical gas turbine combustors.

4.3.4 Flame Transfer Function

The FTF linearly relates the heat release rate fluctuations to the incoming flow perturbations:

$$\text{FTF}(\omega) = \frac{Q'/\bar{Q}}{u'_{up}/\bar{u}_{up}} \quad (4.14)$$

where Q' , \bar{Q} , u'_{up} , \bar{u}_{up} , and ω are the heat release rate fluctuations, the mean heat release rate, the velocity fluctuations upstream of the flame, the mean bulk velocity upstream of the flame, and the angular frequency, respectively.

In this work, the FTF is obtained from the flame transfer matrix, denoted as T , which is reconstructed with the MMM [143]. The T_{22} element describes the relation between the velocity perturbations downstream (u'_{do}) and upstream (u'_{up}) of the flame. For low Mach numbers it can be expressed as:

$$T_{22} = \frac{u'_{do}}{u'_{up}} = 1 + \left(\frac{\bar{T}_{do}}{\bar{T}_{up}} - 1 \right) \text{FTF} \quad (4.15)$$

where, \bar{T}_{do} and \bar{T}_{up} are the mean temperature upstream and downstream of the flame, respectively.

4.4 RESULTS AND DISCUSSION

For all cases, the fuel blend ratio between hydrogen and natural gas is constant at 0.45 by volume. This ratio allows us to operate the combustor

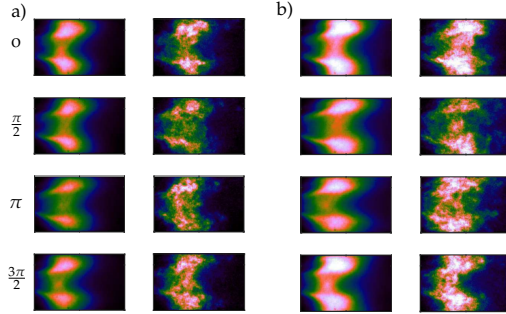


FIGURE 4.3: averaged and instantaneous OH^* flame chemiluminescence at acoustic forcing frequency = 220 Hz at different thermal powers: a) Power = 34 kW, b) Power = 51 kW. The mixture equivalence ratio is kept constant in all operating conditions. White and black corresponds to the maximum and minimum intensity, respectively.

without thermoacoustic instability. The mean equivalence ratio is also kept constant at 0.86. The thermal power of the combustor is varied and results in three different operating conditions, namely 34 kW, 43 kW, and 51 kW.

The phase averaged and instantaneous OH^* chemiluminescence images of the flame are shown in Fig 4.3. As expected, the flame becomes more elongated as the power increases due to the increase of mean bulk velocity. The maximum emission intensity value also increases with power due to the increase of heat release rate.

The raw signals from the photodiode are pre-multiplied with reference cosine and sine and then fed into a Butterworth fourth order infinite impulse response (IIR) low-pass filter. The cut-off frequency is set to 20kHz and 30kHz to recover the $2f$ and $1f$ signals, respectively. Because the laser emitting near 1392 nm is modulated with $f_m = 150 \text{ kHz}$, the frequencies of the reference cosine and sine for the spectra around 7185.59 cm^{-1} have to be set to 150 kHz and 300 kHz to get the $2f$ and $1f$ component, respectively. Similarly, for the spectra at around 6806.03 cm^{-1} the frequencies are set to 200 kHz and 400 kHz. This highlights the benefit of the TDLAS-WMS method: it allows frequency-multiplexing of the two different absorption peaks. Thereby, only one detector is needed to recover the WMS spectra at two different wavelengths.

A short snapshot of the $R_{2f/1f}$ and the raw signal from the photodiode is shown from the measurement is shown in Figure 4.4. In principle, the laser's temperature and current can be tuned to make the downscan

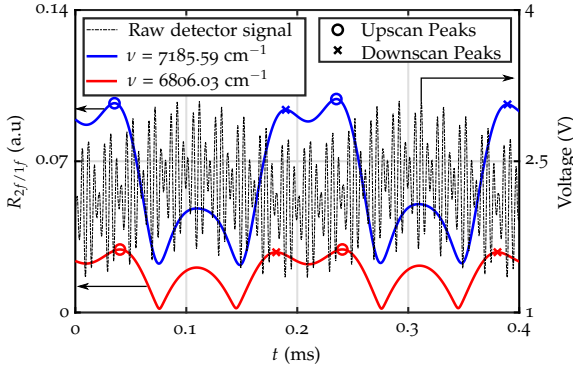


FIGURE 4.4: Time trace of the WMS-2f/1f signals of an acoustically perturbed flame at 43 kW thermal power and 120 Hz acoustic frequency. Only the upscan peaks are used to infer the temperature.

and upscan peaks to be further apart, and separated by close to half of scanning period. However, we decided not to do it because this results in a lower number of etalon peaks during the identification procedure, thereby, sacrificing the accuracy of a_m determination. Since the detector signal is stronger at the upscan section, only the $R_{2f/1f}$ peak ratio at the upscan section is used to infer the temperature.

The inferred temperature and its Fourier transform are shown in Figure 4.5. A snapshot of the temperature time trace and its filtered component around the forcing frequency are plotted in the inset. As seen, the coherent temperature fluctuations are buried in the noise. However, the Fourier transform shows a distinct peak at $f = 120$ Hz which corresponds to the acoustic forcing frequency of the upstream loudspeaker.

The perturbations amplitude at each forcing frequency is then divided by the mean temperature to get the percentage level of perturbation as shown in Figure 4.6 a. The error bars of each temperature measurement correspond to 95% Confidence Interval (CI). They are obtained by considering the uncertainties in the spectroscopic database and the amplitude error due to the measurement noise. The induced temperature fluctuations are in the order of 1% and down to 0.3 % for all operating conditions. The lowest measured coherent temperature fluctuation is 5 K and this highlights the capability of TDLAS in measuring small amplitude coherent temperature fluctuations.

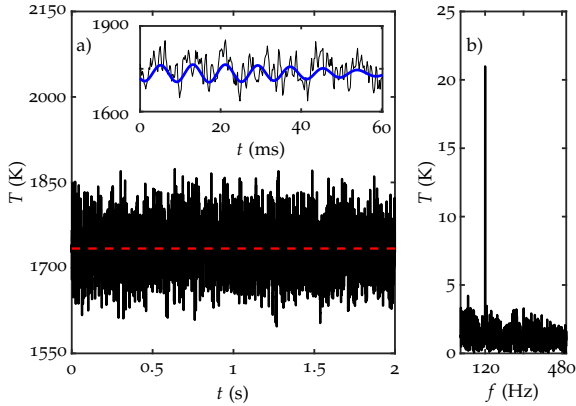


FIGURE 4.5: Inferred temperature of an acoustically perturbed flame at 43 kW thermal power and 120 Hz acoustic frequency. a) Time-resolved temperature, dashed line shows the mean temperature \bar{T} . The inset shows the first 60 ms of the raw temperature time trace (black) and its narrowband-filtered content around the forcing frequency (blue). b). Fourier transform of the inferred temperature.

The amplitude of acoustic velocity perturbations obtained from MMM are shown in Figure 4.6 b. These velocity perturbations are kept to be around 8% to ensure the same signal quality and linearity of the response.

The ETF's gain and its error bars are shown in Fig 4.6c. The error bars of ETF gains are obtained by propagating the error in the temperature fluctuations as this is the largest contributor of the error in ETF. The gains of the ETFs at frequencies between 40-90Hz are similar to the one measured in [126] with a very similar flame and setup but with the data-heavy LIF thermometry. The phase information at $P = 51$ kW and $P = 43$ kW are available, but not at $P = 34$ kW due to synchronization error during the measurements. The phase of ETFs and their linear fit are shown in Figure 4.6d. The error bars of the phase are vanishingly small and thus not represented. The linear fit matches well with the measurement for the first half of the frequencies. The slope of each line corresponds to the time delay between the temperature and the acoustics perturbation, and they match well with the expected convective time delay. As expected, the slope of the red curve is less steep than that of the blue curve because the mean bulk velocity is higher at $P = 51$ kW.

In contrast to the previous numerical and experimental investigations of the ETF (e.g. [129, 130, 144]), the measured temperature fluctuations and

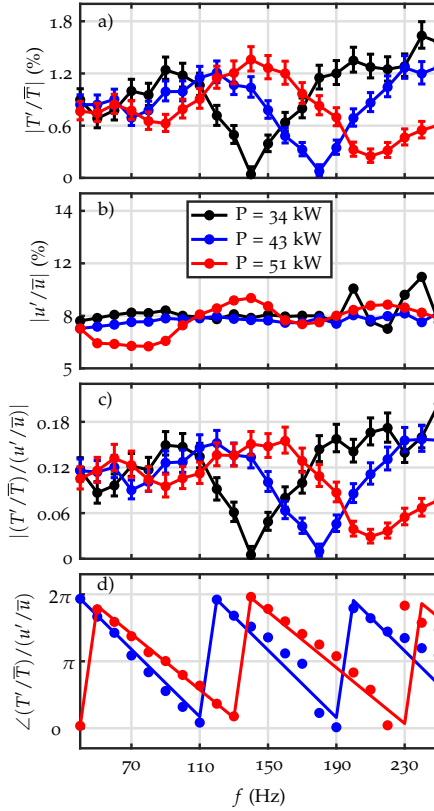


FIGURE 4.6: a) Coherent temperature fluctuation amplitudes, and errorbars correspond to 95% CI. b) acoustic velocity obtained using the MMM. c) ETF gain, errorbars correspond to 95% CI. d) ETF phase and its linear fit (only $P = 43$ kW and $P = 51$ kW are shown due to synchronization error at $P = 34$ kW).

the ETFs do not decrease monotonically with respect to the frequency. It is worth mentioning that the acoustic frequency range in this work is wider and reaches a significantly higher frequency than the one measured in [126, 129, 130] thanks to the higher bandwidth of the method. Because higher frequencies can be reached, peculiar phenomena, which are manifested by the minimum of ETF, are uncovered. This behavior is similar to the FTF of a technically premixed swirled flame. To remove the velocity dependency

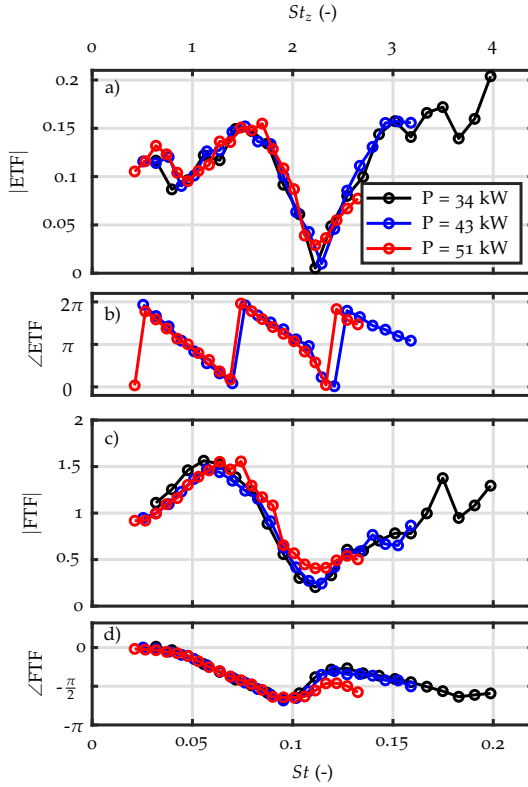


FIGURE 4.7: a) Strouhal number dependence of ETF gain and b) phase. c) The corresponding FTF gain and d) phase at the considered cases.

of the ETF, the gain and phase are plotted against the Strouhal number in Fig .4.7. We employ two different definitions of the Strouhal number. The first is $St = fL/\bar{U}$, where f is the frequency, L is the reference length which is the hydraulic diameter inside the swirler block (14.5 mm), and \bar{U} is the mean bulk velocity inside the swirler block which differs for all operating conditions. This definition is the same as in [145]. The second Strouhal number is $St_z = fz/\overline{U_{d0}}$, where z is the axial distance of the measurement location from the burner outlet, and $\overline{U_{d0}}$ is the mean bulk velocity downstream of the flame. St_z essentially compares the convective wavelength to the axial distance from the burner [130]. The measured FTF are also plotted against the Strouhal numbers for the same reason.

The collapse of the ETFs gain and phase in the Strouhal number space indicates that the mechanism of entropy generation and transport scales well with Strouhal number. The same observations were also reported in [130] and [129].

The minimum location of each ETF curve collapses at the same Strouhal number, which strongly suggests a physical mechanism behind this non-monotonous behavior rather than measurement error or quality issues. Moreover, the measured flame transfer functions exhibit low response at the same Strouhal number. This might seem obvious because entropy fluctuations are due to heat release rate fluctuations. However, entropy fluctuations are predominantly caused by the part of the heat release fluctuations that is caused by equivalence ratio fluctuations. The part of the FTF caused by equivalence ratio fluctuations (FTF_ϕ) typically does not feature pronounced minima or maxima [146].

Indeed, if one considers a dispersion of entropy waves due to turbulence, one would expect a monotonic decline of temperature amplitude with respect to frequency. The convective wavelength in all cases and frequencies varies from 9 cm to 60 cm. However, the turbulent length scale is in the order of the duct height which is 6.2 cm. Indeed, it was shown in [47] that in addition to shear dispersion associated with the transverse gradient of mean axial velocity [129, 140], the distortion of entropy waves by large turbulent structures significantly contributes to the monotonic decay of their amplitude.

It is thus suspected that the non-monotonic behavior of ETFs and the similarity between the FTFs and ETFs is caused by a different mechanism. Some possible mechanisms are outlined as follows. First, the system is not adiabatic due to heat losses across the combustor walls. The effect of heat loss on the entropy waves propagation has been studied in [147] and [148]. Both studies showed that thermal boundary condition at the walls has a significant effect on the decay of the entropy waves. In our case, the velocity fluctuations downstream of the flame will follow the same trend as the FTF as described in equation (4.14). Because the heat transfer to the wall is strongly dependent on the velocity, a fluctuation of velocity will cause a varying heat loss hence leading to temperature fluctuations. Second, additional hydrodynamic perturbations might be generated right after the swirler and can subsequently interact with the equivalence ratio perturbations at the injection holes. The net effect of these perturbations can alter constructively and destructively the equivalence ratio fluctuations at the burner outlet depending on the convective delay of each perturbation.

This is similar to the investigation done in [142]. Third, the existence of large coherent structures in swirling flows can favor a specific frequency which scales with the Strouhal number as reported in [145]. They can subsequently disperse the entropy waves and affect the flame transfer function at the same frequency.

The TDLAS-WMS method developed in this chapter has initiated a research collaboration to further investigate, by means of numerical simulation, the generation of entropy waves for the nonadiabatic combustor [149]. For that study, the combustor is operated in a fully premixed mode and the flame thermal power is set to 51 kW with the same hydrogen mixing as in this study. It is indeed confirmed that the generation of entropy waves in the fully premixed combustor is caused by the heat loss to the combustor wall. An additional mechanism that plays a non-negligible role is preferential diffusion, which is relevant in this case due to the high level of hydrogen blending (in volume).

Furthermore, the TDLAS-WMS method is also employed to measure the temperature fluctuations inside the mixing channel of an atmospheric sequential combustor operated with full hydrogen as sequential fuel, as demonstrated in [150]. However, in that study, the flame transfer function of the sequential flame was not investigated. In that study, the focus was on the quantification of the effect of temperature fluctuations on the ignition kernel generation of the sequential hydrogen flame under stationary and transient operations.

4.5 CONCLUSION

Entropy transfer functions (ETFs) of a technically premixed swirled flame are measured with the TDLAS-WMS method. The method is able to capture coherent low-temperature fluctuations at a measurement rate of 5kHz accurately, highlighting its applicability for ETF measurements. This is the first time that TDLAS-WMS is applied for ETF measurements. Due to the high frequency range and the sensitivity of the method, peculiar features of the ETF could be uncovered. Hence, the method could be considered for future experimental studies on ETF investigations. It was demonstrated that the ETF's gain does not decrease monotonically with respect to the acoustic forcing frequency in contrast to the previous studies in the literature that were limited to a lower frequency range. Moreover, it is observed that the ETFs measured at different operating conditions collapse to each other when

plotted against Strouhal number. The developed TDLAS-WMS method in this chapter has initiated further follow-up studies.

ACKNOWLEDGMENTS

This chapter is based on the paper “*Entropy Transfer Function Measurement with Tunable Diode Laser Absorption Spectroscopy*”, by Bayu Dharmaputra, Sergey Shcherbanev, Audrey Blondé, Bruno Schuermans, and Nicolas Noiray, published in the Proceedings of The Combustion Institute in October 2022. This study was supported by the European Research Council under the ERC Consolidator Grant (No: 820091) TORCH (2019-2024) and by the ETH foundation. Professors Fei Qi and Yuan Xiong are also acknowledged for their assistance during the initial development phase of the TDLAS system.

PLASMA ASSISTED THERMOACOUSTIC STABILIZATION OF A TRANSIENTLY OPERATED SEQUENTIAL COMBUSTOR AT HIGH PRESSURE

*Shall I refuse my dinner because I do not fully
understand the process of digestion?*

— Oliver Heaviside

In this chapter, the nanosecond repetitively pulsed discharges with pin-to-pin configuration is employed to stabilize the constant pressure sequential combustor at high pressure. This study demonstrates the control of thermoacoustic instabilities with NRPD up to 6 bar, in both stationary and transient modes of operation. Two types of transient scenarios are considered. In the first transient scenario, the combustor pressure is linearly increased from 4 to 5 bar, which corresponds to an increase of the overall thermal power from 273 kW to 341 kW, while continuously employing NRPD to stabilize the system. In the second transient case, the tunable outlet orifice of the sequential combustor is progressively swept from 91.6 % to 100 % of its maximum area. In both cases, the NRPD shows remarkable performance in suppressing the thermoacoustic instability at ultra-low plasma power compared to the thermal power of the combustor, down to about $1 \times 10^{-2}\%$. This achievement opens the way for further developments toward the commercial application of NRPD-based plasma assisted combustion in sequential combustors.

5.1 INTRODUCTION

Similarly to traditional single stage combustors, constant pressure sequential combustor (CPSC) is susceptible to thermoacoustic instabilities, which constitute a key challenge in the development of gas turbines for power and propulsion systems [26]. These instabilities can cause pressure fluctuations that reach a significant fraction of the mean pressure, and can cause structural damage due to induced vibrations [33]. Their mitigation is still based nowadays on passive solutions and expensive trial-and-error testing during the combustor development phase. Therefore, developing cost-effective actuators to control them would have a pivotal effect on the

development and operation flexibility of gas turbines. Furthermore, to meet the fluctuating energy demand resulting from the intermittent production of renewable sources, modern gas turbines need a fast reaction time [67], and during transient operation, they can be temporarily brought to conditions leading to thermoacoustic instabilities. Therefore, it is not surprising that such problematic instabilities during transient operation have recently drawn attention in the research community [151, 152, 153, 154].

Active control strategies can adapt to changing operating conditions, but their implementation in real gas turbines faces challenges due to the lack of robust and swift actuators [76]. Approximately three decades ago, a successful active control approach involving rapid adjustments to fuel mass flow was developed, which proved to be effective for liquid spray systems [78] and natural gas setups [79]. The latter innovation was validated in heavy duty gas turbines and entered commercial usage. However, this mechanical solution with moving parts was not sufficiently cost-effective to become a standard equipment on the gas turbine market, and today's turbines rely on less flexible, but more robust passive solutions. In this context, the demonstration of an effective actuation system, without moving parts, could change the control approach paradigm.

Consequently, several studies have explored the impact of nanosecond repetitively pulsed discharges (NRPD) on the fluctuations of the flame heat release rate [62] and on the lean blow-out extension of the flame [82, 155, 156], recognizing its significant influence on the kinetics of reactive mixtures. In a single-stage swirled stabilized combustor, Lacoste et al. [62] observed substantial effects of NRPD on the gain and phase of the flame transfer function (FTF), hinting at potential implications for thermoacoustic stability. A more recent study on the effect of NRPD to flame transfer function of a turbulent swirled burner at elevated pressure was presented in [90]. In that study, it was shown that the NRPD affects the flame dynamic by creating a region where the heat release rate fluctuations of half of the flame are in phase opposition with the other half, rendering a global reduction in the heat release rate fluctuation. Besides, Moeck et al. [54] successfully used nanosecond plasma discharges for active feedback control to stabilize a linearly unstable combustor. They utilized the extended Kalman filter (EKF) to estimate the instantaneous phase of acoustic pulsation, modulating the plasma generator's gate signal accordingly. In that study, the atmospheric combustor was operated only in steady-state manner. Following the same control architecture, Khalifa et al. [86] showed that glow discharge with a plasma power of around 1 W could stabilize a laminar methane flame.

Recently, Shcherbanev et al. [57] demonstrated the effectiveness of plasma discharges in igniting a lean mixture of hydrogen and natural gas blending in a sequential combustor. Another notable application of NRPD in an atmospheric sequential combustion is presented in [110]. The study used NRPD to stabilize the combustor in steady-state operation, extensively examining the influence of two plasma parameters, pulse repetition frequency (PRF) and generator voltage, on acoustic pulsation and NO emissions. The minimum plasma power that can effectively stabilize the combustor was $1.5 \times 10^{-3}\%$ of the thermal power of the flames, which is ultra low and attractive for practical application in real gas turbines.

The thermoacoustic stabilization of combustors under transient operation remains unexplored in the literature. Moeck et al. [157] showed the thermoacoustic stabilization of a lab scale combustor under transient preheating temperature variations by using loudspeakers. However, such actuators are not applicable in a real engine. In this study, our objective is to demonstrate and assess the performance of NRPD in stabilizing a sequential combustor under high-pressure conditions and during transient scenarios. Two distinct transient scenarios are investigated. In the first scenario, modifications to the outlet acoustic end area are achieved using the motor-driven piston. In the second scenario, there is a simultaneous ramp-up of combustor pressure and power.

5.2 EXPERIMENTAL SET-UP

The lab-scale sequential combustor setup is depicted in Fig. 5.1. The setup consists of a plenum, a matrix burner for anchoring 4×4 turbulent jet flames, a combustion chamber which also exhibits a $62 \times 62 \text{ mm}^2$ cross-section, a dilution section, a mixing channel with $25 \times 38 \text{ mm}^2$ cross-section, a secondary fuel injection, a sequential or second-stage combustion chamber, and an adjustable orifice. The first-stage combustion chamber uses a mixture of natural gas and air, with preheated air of $270 \text{ }^\circ\text{C}$ and introduced from the plenum, while natural gas is added through the matrix burner, creating a technically premixed mixture. A piezosensor is placed on a flush-mounted plate to monitor the pressure pulsations inside the first stage combustor denoted as Mic. 1 in the figure. Dilution air at temperature of $80 \text{ }^\circ\text{C}$ is introduced from the dilution air port and mixes with the hot gases from the first stage flame. A mixture of 11 % hydrogen and 89 % natural gas, by mass, is injected through the sequential injector. The sequential injector features an X lobe-shaped vortex generator to introduce rotational move-

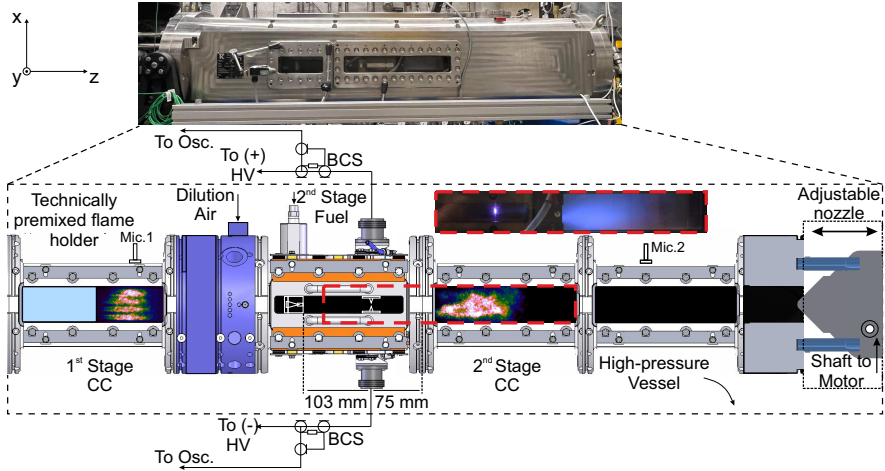


FIGURE 5.1: Sketch of the lab-scale sequential combustor operated in the ETH high pressure test rig shown above in the image. CC - Combustion chamber, BCS - Back Current Shunt, HV - high-voltage generator. The inset in the dashed rectangle display an image of the sequential flame with plasma actuation in the mixing channel.

ment to the vitiated flow, which enhances the mixing process. A pin-to-pin electrode configuration, with an inter-electrode distance of 5 mm, is located downstream of the sequential fuel injector. Another piezo sensor is placed downstream of the sequential flame to monitor the pressure pulsations of the second combustion chamber. As indicated above, the outlet of this chamber has an adjustable orifice to control the thermoacoustic stability of the system. The outlet orifice is composed of a conical piston which is connected to a DC motor. Adjusting the position of the piston horizontally enables the variation of the exit area, and therefore a variatio of the outlet reflection coefficient, which has a key influence on the thermoacoustic stability. The sequential combustor is inserted in a large pressure vessel equipped with a water-based heat exchanger, which cools the combustion products before the large back-pressure that is used to control the operating pressure of the combustor.

The optical access to the flames is enabled through wall-mounted quartz windows on the combustor which are cooled with air jets and another set of thick quartz windows on the high pressure vessel. Chemiluminescence

from the OH* is used to analyze the sequential flame, with a camera that captures a segment of the mixing channel located downstream of the electrodes. An optical obstruction conceals the intense light emitted by the plasma discharges. The recording configuration includes a LaVision Star X high-speed CMOS Camera and a LaVision HS-IRO high-speed intensifier, both fitted with a 45 mm CERCO UV lens (F/1.8 Cerco) and an Edmund Optics optical bandpass filter (centered at 310 nm, FWHM 10 nm).

The plasma generator (FID) initiates the high voltage pulses with a 2-3 ns rise time and a pulsed width of 10 ns. In this study, the pulse repetition frequency (PRF) is fixed at 10 kHz. Back current shunts (BCS) are implemented into the outer shield of the transmission lines, positioned both on the anode and cathode, each 7 m away from the electrode system. These shunts serve to capture the incident and reflected pulses from each source polarity. A mixed signal digital oscilloscope (Tektronix MSO54B) was used to record the current and voltage signals at 1 GHz bandwidth and 6.25 GHz sampling rate.

5.3 METHODOLOGY

5.3.1 Plasma energy deposition

Fig. 5.2 presents the signals recorded by the BCS for the positive polarity voltage waveform, with and without plasma ($V_{\text{gen}} = 10$ kV) at $\bar{P} = 4.5$ bar. The instantaneous cumulative energy of the pulse is:

$$E(t) = \int_{t_0}^t \frac{V^2(t') \times \text{sign}(V(t'))}{Z_c} dt', \quad (5.1)$$

where V is the recorded voltage time trace, Z_c is the impedance of the cable which in our case equals to 50 Ω . In equation 5.1, the voltage sign distinguishes between incoming (positive) and reflected (negative) energy. The deposited energy, denoted as E_D , is the cumulative energy at the end of each time instance, specifically $E_D = E(t_e)$, where t_e is the total duration of the recorded signal. In an ideal scenario without plasma breakdown, incident and reflected energy are equal. In practical cases, where losses occur, a baseline measurement with the combustor off yields the energy loss E_{D_c} . For plasma breakdown situations, the energy E_{D_h} is obtained through the same procedure. Accounting for losses, the energy deposited in the plasma, $E_{D_{pl}}$, is then:

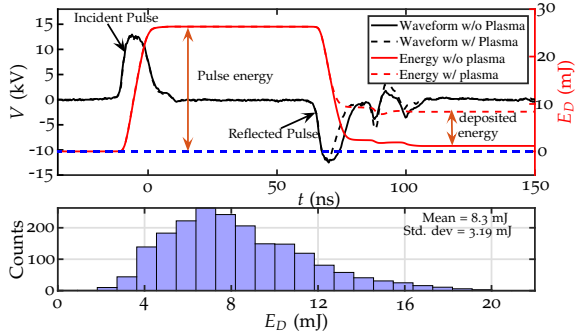


FIGURE 5.2: Waveform of the signals obtained with BCS for positive polarity 10 kV, $P = 4.5$ bar (top) and the resulting distribution of 2000 consecutively measured energy deposition (bottom).

$$E_{D_{pl}} = E_{D_h} - E_{D_c}. \quad (5.2)$$

In this study, both polarities contribute to the total energy deposition. In order to obtain enough statistics, 2000 consecutive pulses are obtained in every measurement. The histogram in Fig. 5.2 shows the characteristic distribution of the deposited energies. In the following paragraphs, $E_{D_{pl}}$ is abbreviated as E_D for brevity. The mean plasma power is computed as the product of the mean energy deposition and a fixed PRF of 10 kHz. The ratio of the mean plasma power to flame thermal power is represented by η_p .

5.3.2 Operation of the sequential combustor

The operation of the setup is enabled through a control software which regulates all the mass flow controllers for the air, fuel, and cooling water, and monitors the temperature and static pressure probes at different locations in the setup. The piston position for the adjustable acoustic end boundary is also controlled by the same software in real-time. The variability of the outlet allows us to stabilize or destabilize the combustor on demand. Adjusting the outlet area does not significantly change the pressure level of the combustor. The combustor pressure is mainly regulated through a back pressure valve, strategically positioned outside the high pressure vessel and downstream of a water-based heat exchanger for cooling the hot gas. It serves as a pivotal component in maintaining pressure equilibrium. In addition, the

operating pressure can be finely adjusted by regulating the flow of cooling air employed for the optical quartz windows of the combustion chamber. The interplay of these two mechanisms ensures precise control, allowing a comprehensive investigation into the intricacies of combustion under varying conditions. In this study, the back pressure valve is set to a specific value and the pressure can be linearly tuned simply by increasing the mass flow of the air, fuel, and the cooling air simultaneously. Therefore, the volumetric flow rates are the same for different combustor pressures.

In this study, the thermal power of the second stage flame amounts to 52% of the total thermal power of the flame. The combustor pressure and the total thermal power of the flames, W_{th} , are related as:

$$W_{th}[\text{kW}] = K[\text{kW}/\text{bar}] \times \bar{P}[\text{bar}], \quad (5.3)$$

where K is a constant and equals to 68.25. The combustors are operated from $\bar{p}= 4$ to 6 bar, hence, the total thermal power of the flames ranges linearly from 273 to 409.5 kW, whereas, the equivalence ratios of the first stage and sequential flame remain constant at 0.7 and 0.55, respectively.

Two microphones are used to characterize the thermoacoustic stability of the combustor. The definition of the acoustic power spectrum of the signal is:

$$S_{pp}(\omega) = 20 \log_{10} \left(\frac{\hat{p}_{\text{rms}}(\omega)}{2 \times 10^{-5} \text{Pa}} \right), \quad (5.4)$$

where ω is the angular frequency, p'_{rms} is the root mean squared (RMS) of the acoustic pressure p' , $\hat{\cdot}$ denotes the Fourier transform and $S_{pp}(\omega)$ is the power spectrum. The main instability frequency occurs at around 400 Hz for all cases.

5.4 RESULTS AND DISCUSSION

5.4.1 Steady-state mapping

As stated previously, the ultimate objective is to achieve thermoacoustic stabilization of the combustor under conditions of transient combustor pressure increase and outlet area variation. Therefore, the acoustic pulsations of the sequential combustor are initially analyzed across different combustor operating pressure and outlet area during steady-state operation.

The outlet area undergoes a gradual sweep, ranging from 86% to 100% of its maximum value in 5% increments, while the combustor pressure

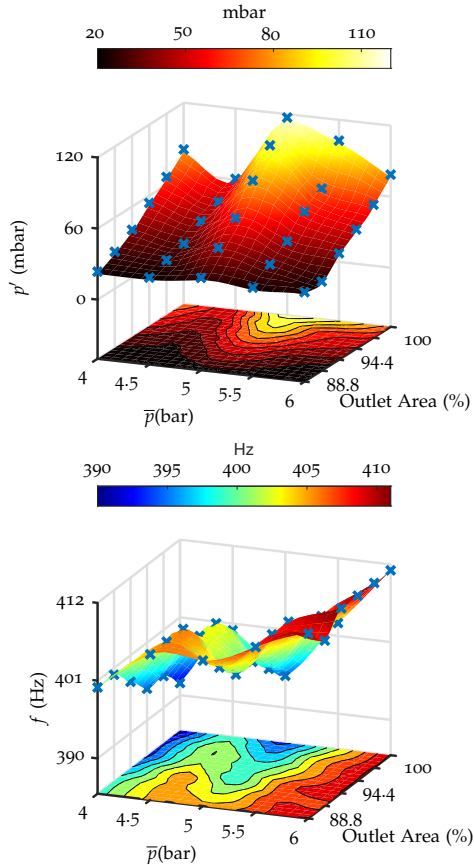


FIGURE 5.3: Surface maps of the RMS acoustic pressure pulsations in the first stage combustion chamber as a function of the combustor pressure and outlet orifice area (Top) and the associated peak frequency (bottom). The blue crosses show the measurement points.

is systematically varied from 4 to 6 bars with 0.5 bar increments. They all amount to 25 grid points. For each point, the signal is recorded for 30 seconds to ensure statistically converged values. The surface maps of p'_{rms} , and the peak frequency of the signal are shown in Fig. 5.3. As observed, the acoustic pulsation amplitude increases monotonically with the outlet orifice area for each \bar{p} . Conversely, for a constant outlet orifice area, an increase in \bar{p} results in a non-monotonic behavior of p'_{rms} . The maximum p'_{rms} occurs at $\bar{p} = 5$ bar with an outlet area of 100%. However, the peak frequency exhibits

the opposite trend. Under fixed operating conditions, the acoustic pulsation amplitude and peak frequency show a negative correlation. This could be attributed to a correlation between acoustic pulsation and the mean flame length (not shown here). When the acoustic pulsation is high, the mean flame length also increases, thus increasing the characteristic time delay τ of the acoustic perturbations to the flame front. The increase in time delay would result in a lower frequency of instability. However, it is not the focus of this study to analyze possible mechanisms to fully explain the trends.

As the highest pulsation is observed at $\bar{p}=5$ bar, the selected path for the transient scenario involves a trajectory from $\bar{P}=4$ bar to $\bar{p}=5$ bar, with the outlet area set at a constant 100%. In the alternate transient case, \bar{p} remains fixed at 5 bar, while the outlet area undergoes a transient sweep, ranging from 91.6% to 100%.

The performance of NRPD at high pressure is first evaluated at $\bar{p}=5.5$ bar and $V_{\text{gen}}=10$ kV. In this condition, the plasma power equals to 29 W, and hence $\eta_p = 7.7 \times 10^{-3}\%$. The results are shown in Fig. 5.4. The discharge is initiated at $t = 500$ ms. Before the initiation, the combustion chamber exhibits high acoustic pulsations, and both the flame length and intensity change dramatically within half of the acoustic cycle. After the plasma actuation starts, the amplitude of the acoustic pressure starts to decay, and the instability disappears within 50 ms. Consequently, the sequential flame becomes more steady, and due to the presence of the discharge, some ignition kernels appear in the mixing channel (see Fig. 5.4f and 5.4g).

The most interesting regime in terms of characterization of plasma effect on acoustic pulsations is at $\bar{p} \sim 5$ bar, which will be the focal point of this study. The same procedure is performed at lower \bar{p} 's, and the power spectrum of the acoustic pulsation inside the second stage combustion chamber without and with NRPD are plotted in Fig. 5.5 a) and b). Without plasma discharge, the combustor exhibits a limit cycle with a high amplitude and narrow spectral peak around the frequency of 400 Hz. Notably, the higher harmonics are also pronounced. The scaled probability density functions (pdf) are plotted in the inset and show bimodal distributions, which is a typical feature of a system in the limit cycle (see e.g. [158]). The spectra with the plasma discharge actuation look rather different; the higher harmonics are not present anymore, and the main peak is at lower power and becomes wider. The scaled pdf has a quasi-Gaussian distribution, which is a typical feature of a stochastically forced linear stable system.

The energy deposition measurements under various conditions are plotted in Fig. 5.6, together with p'_{rms} and η_p . Figure 5.6a shows the energy

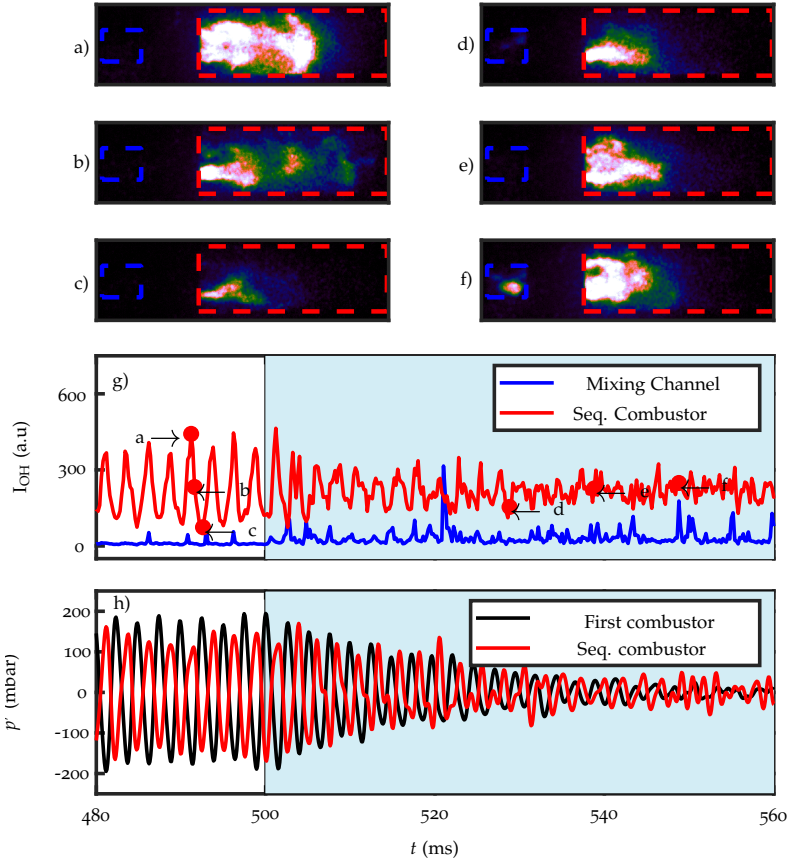


FIGURE 5.4: Thermoacoustic stabilization at $\bar{p} = 5.5$ bar $V_{gen} = 10.0$ kV, $\eta_p = 7.7 \times 10^{-3}\%$. (a-f) OH chemiluminescence of the sequential combustor at 6 different time instances with the time instances shown in g). Plasma is initiated at $t = 500$ ms. g) Mean OH* intensity within the mixing channel and sequential combustor. h) The acoustic pressure signal within the first and sequential combustor.

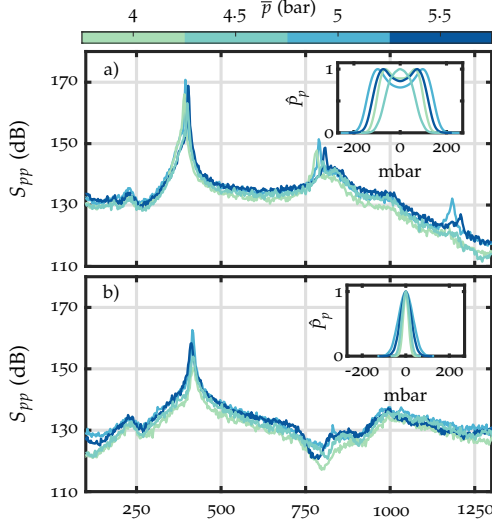


FIGURE 5.5: The power spectra of the second stage microphone at the 4 considered combustor pressures without a) and with b) NRPD actuation at the generator voltage of 10kV. The outlet area is fixed at 100%.The insets show the corresponding normalized probability density function of the bandpass-filtered microphone signal around the instability frequency.

deposition at constant $V_{\text{gen}} = 10$ kV for different combustor pressures. As seen, at a fixed voltage, the energy deposition decreases with pressure due to the corresponding increase in the gas density, ρ , resulting in reduction of the specific electric field values (E/ρ). At this generator voltage, the energy deposition exponentially decays from 22.62 mJ at $\bar{p} = 4$ bar to 2.91 mJ at $\bar{p} = 5.5$ bar. Consequently, η_p varies from $8 \times 10^{-2}\%$ down to $7.7 \times 10^{-3}\%$. Note that as the pressure of the combustion chamber increases, the thermal power of the flame also increases; therefore, the reduction η_p is caused by both a reduction in E_D and an increase in W_{th} . To study the effect of generator voltages, further energy deposition measurements are performed at $\bar{p} = 4$ bar and $\bar{p} = 5$ bar and are plotted in Fig. 5.6b) and c). In both cases, the generator voltage is progressively lowered from 10 kV until there is no discharge initiated. As expected, for both \bar{p} , the energy deposition increases monotonically with respect to V_{gen} , while p'_{rms} decreases monotonically with respect to the generator voltage.

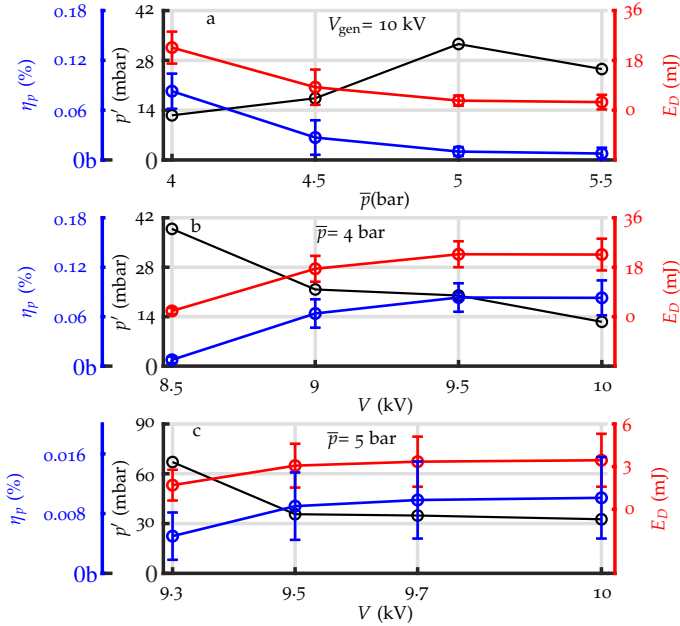


FIGURE 5.6: a) The energy deposition (red), rms pressure in the sequential combustion chamber (black), and the ratio between the mean plasma power and the thermal power of the flames (depicted in blue) $V_{gen}=10$ kV at different \bar{p} . The same quantities are illustrated at a fixed pressure of b) $\bar{p}=4$ bar and c) $\bar{p}=5$ bar with variations in generator voltage. The error bars represent uncertainties at a 2σ interval.

5.4.2 Transient operation

The first transient operation involves a linear increase in the combustor pressure from four to five bars and, consequently, in the thermal power of the flames from 273 kW to 341 kW. This is done by locking the proportion of air and fuel mass flows at $\bar{p}=4$ bar and then entering the total mass flows at $\bar{p}=5$ bar as the set point. The control software automatically creates a linear ramp whose rate is limited to ensure safety operations. The outlet area of the adjustable orifice is set to 100% in this transient case.

The results of the first transient thermoacoustic stabilization are shown in Fig. 5.7. In the first five seconds of the recording, the setup is operated without any discharge, the system is unstable and can be confirmed by

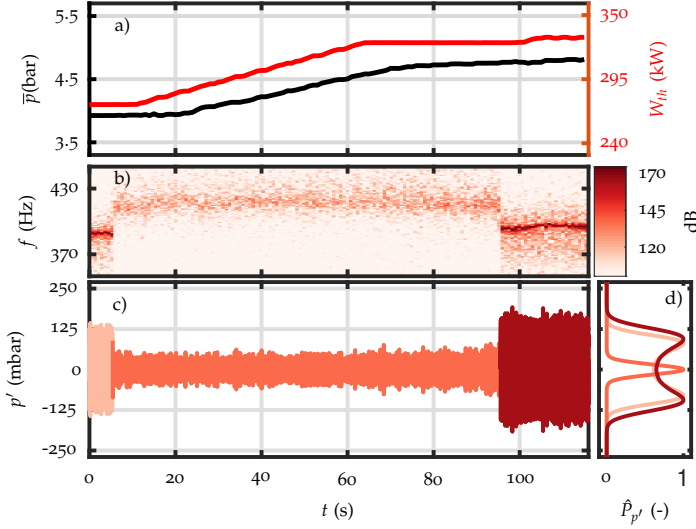


FIGURE 5.7: a) The time trace of combustor pressure and the thermal power of the flames during the transient operation, the outlet area is fixed at 100%. b) Spectrogram of the acoustic signal of the sequential combustion chamber within the bandwidth of the main instability frequencies. c) The time trace of the acoustic pressure pulsation within the sequential combustor (Mic 2 in figure 5.1). The pulsations are colored with three different colors, indicating three different regimes. d) The scaled probability density function (pdf) of the corresponding acoustic pressure pulsation in c).

looking at the corresponding scaled pdf in Fig. 5.7d). At $t = 5$ s, the plasma discharge is initiated with $V_{gen} = 10$ kV, resulting in $\eta_p = 0.08\%$. As can be seen from Fig. 5.7c), the acoustic pulsation amplitude decreases instantly. The signal spectrogram shown in Fig. 5.7 shows an intense peak at a frequency of around 395 Hz for $t \leq 5$ s. Subsequently, after the plasma initiation, the peak frequency of the signal jumps to a higher value of around 420 Hz. However, the spectra become more spread across the frequency space. So far, the behavior is in good agreement with the steady operation experiments shown in Fig. 5.5. At $t = 10$ s, the set point that corresponds to the state at $\bar{p} = 5$ bar is entered into the control software. As seen in Fig. 5.7a), the thermal power of the flame starts to increase earlier than the combustor pressure. This is due to the faster response time of the fuel mass flow controller compared to air. During the initial moments of the transient

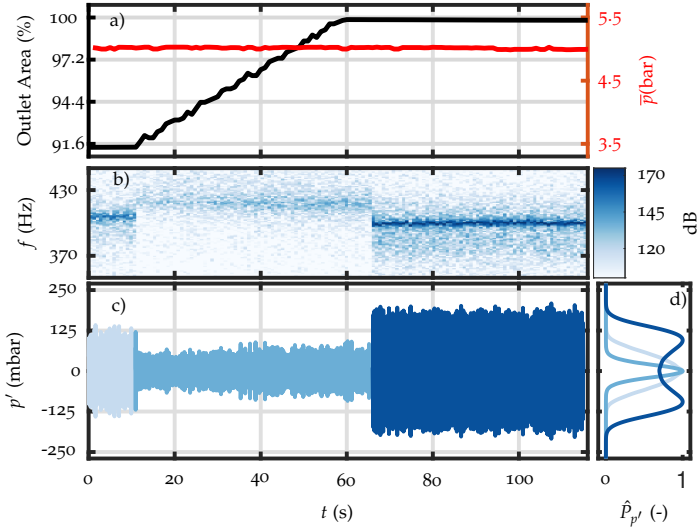


FIGURE 5.8: Outlet area variation at $\bar{p} = 5$ bar. a) Time trace of the outlet area of the combustor during transient operation. b) Time trace of the acoustic pressure pulsation inside the sequential combustion chamber (Mic 2 in Fig. 5.1). The pulsations are colored with three different colors, indicating three distinct regimes. c) Scaled probability density function (pdf) of the corresponding acoustic pressure pulsation in b).

phase, the combustor operates with a slight variation in equivalence ratio. However, plasma actuation is still effective in suppressing instability during transient operation. Looking at the scaled pdf of the signal within the corresponding transient regime in Fig. 5.7, one can see that the combustor is indeed thermoacoustically stable. At $\bar{p} = 5$ bar, η_p equals to 0.01%. At $t = 95$ s, the NRPD is turned off, and the system immediately becomes unstable again, and the instability frequency is very similar to the one at the beginning of the recording. This outcome serves as a compelling proof of concept, demonstrating that NRPD enables the seamless operation of a sequential combustor during power ramp-up conditions with a very low plasma power.

In the second transient case, the adjustable outlet orifice is linearly increased from 91.6% to 100% of the maximum area while maintaining the combustor pressure at five bars. The principle operation is the same as before, the dedicated software regulates the rate of ramping of the outlet orifice piston. Changes in the outlet orifice area affect consequently acoustic

losses. Such a change in acoustic losses could occur in a real system, for example, in a situation where the installed Helmholtz damper in a gas turbine fails due to periodic hot gas ingestion [73]

The results of the second transient study are shown in Fig. 5.8. Similar to the previous condition, prior to plasma actuation, the system exhibits pronounced acoustic pulsation. Looking at the scaled pdf of the corresponding regime in Fig. 5.8d), intermittent instability is evident in the system [158]. The intermittency is also confirmed by looking at the magnified time trace data (not shown here). The signal spectrogram, shown in Fig. 5.8, shows a relatively intense peak at around 410 Hz for $t < 10$ s. Plasma discharges with the same parameter as the first transient case are initiated at $t = 10$ s. As seen, the pulsation immediately drops, and, similarly to the previous case, the peak frequency also goes up to around 420 Hz, also with a broader distribution over the frequency space. After the initiation of plasma, the area of the outlet orifice area is immediately increased, as shown in Fig. 5.8. Additionally, it can be seen that the combustor pressure remains unaffected by the value of the outlet orifice area in the considered range. The setpoint is reached within 50 s. As seen on the scaled pdf curve during the ramp up, the system is indeed linearly stable. At $t = 65$ s, the control is turned off and the system immediately becomes unstable with a pulsation higher than that of the starting point, and a decrease in the peak frequency value can be observed. The changes in pulsation amplitude and frequency are consistent with the maps in Fig. 5.3. This result further strengthens our claim that NRPD is a suitable tool to cope with changes in the combustor parameters.

5.5 CONCLUSION

This study demonstrates the capability of NRPD as an actuator for suppressing thermoacoustic instabilities in a high-pressure sequential combustor at plasma power that is about 4 orders of magnitude lower than the combustor thermal power. Indeed, successful stabilization is achieved at a maximum combustor pressure of 5.5 bar, with NRPD exhibiting effective control at a mean plasma power of $7.7 \times 10^{-3}\%$ relative to the thermal power of the flames. Notably, this marks the first application of NRPD for stabilizing thermoacoustic instabilities at pressures exceeding four bar. Furthermore, the study demonstrates the ability of NRPD to effectively stabilize the combustor under transient operations, which is highly relevant for gas turbines, yet it has remained uncharted in the literature. Using a voltage set at the maximum attainable value of 10 kV during transient pressure increases,

the mean plasma power relative to the thermal power of the flames varies from 0.08% at 4 bar to 0.01% at 5 bar. Although there is potential for further optimization of electrode geometry and positioning, the presented results highlight the promising performance of NRPD, suggesting its potential applicability in real systems.

ACKNOWLEDGMENTS

This chapter is based on the paper "*Plasma Assisted Thermoacoustic Stabilization of a Transiently Operated Sequential Combustor at High Pressure*", by Bayu Dharmaputra, Sergey Shcherbanev, and Nicolas Noiray, submitted to the Proceedings of The Combustion Institute in December 2023. This study was supported by the European Research Council under the ERC Consolidator Grant (No: 820091) TORCH (2019-2024).

SUMMARY AND OUTLOOK.

Nothing in life is to be feared, it is only to be understood. Now is the time to understand more, so that we may fear less.

— Marie Curie

This thesis presents a multifaceted study on the use of nanosecond repetitive pulsed discharges (NRPD) to control the thermoacoustics of a constant-pressure sequential combustor (CPSC). This study includes performing experiments under atmospheric and elevated pressure up to 6 bar. Thermoacoustic stabilization with NRPDs is studied under stationary and transient operation of the combustor. Another key component of this research is the development and meticulous study of novel safe Bayesian optimization algorithms. This algorithm is designed for real-time optimization of NRPD and combustor parameters to effectively reduce NO_x emissions while maintaining stability. In parallel, the thesis delves into the development of an advanced temperature probe sensor based on tunable diode laser absorption spectroscopy with wavelength modulation spectroscopy (TDLAS-WMS). This sensor is specifically designed to measure coherent temperature fluctuations, a critical quantity in characterizing the response of the sequential flame.

Thus, this thesis presents a comprehensive approach, tackling both the practical demonstration of actuators and control algorithms, as well as the development of a fast laser-based temperature sensor to experimentally quantify the temperature fluctuations.

The experimental setup features a pin-to-pin electrode arrangement positioned within the mixing channel of the sequential combustor. Chapter 2 focuses on the **thermoacoustic stabilization of the atmospheric CPSC using NRPD**. It examines the impact of various NRPD parameters, such as voltage and pulse repetition frequency (PRF), on both the morphology of the sequential flame and the thermoacoustic stability of the combustor under atmospheric pressure condition. The study uncovers several novel results that are important for further research. The main findings in chapter 2 are listed as follows:

- *NRPDs actuator with ultra-low-power requirement.* The research uncovers that a mean plasma power, amounting to just 1.5×10^{-3} percent of the flame's thermal power, is sufficient to effectively stabilize the thermoacoustics in the sequential combustor, while causing only a minimal increase in NO emissions.
- *Trade-off between acoustic pulsation and NO emission.* Increasing the mean plasma power slightly reduces the root mean squared of the acoustic pressure and accelerates the thermoacoustic decay rate, but at the expense of higher NO emissions.
- *Destabilizing effect of NRPDs.* An intriguing finding is that certain NRPD parameter settings cause the combustor to switch modes, moving from around 330Hz to 260Hz. After this switch, the pressure pulsations at 260Hz are notably higher than those at 330Hz. During the instability cycle, the plasma discharges are periodically bent in the direction of the stream, in synchronization with the acoustic pulsations. Additionally, the plasma volume also varies with the acoustic pulsations.

As a follow-up study described in chapter 2, novel optimization algorithms based on the safe Bayesian optimization (safeOpt) algorithm are developed and outlined in detail in Chapter 3. The algorithms are data-driven, thereby, could work without models. The main purpose of the algorithms is to find the optimum combination of control parameters in the system while satisfying the safety criteria throughout the iterations. The framework allows the transfer of knowledge between operating conditions, which then reduces the number of iterations required to find the optimum location or region. The main findings of chapter 3 are as follows:

- *Two adaptations of safeOpt algorithm: shrinkAlgo and stageOpt.* The safeOpt algorithm works by approximating the objective and constraint function with Gaussian process regressors (GPRs). At each iteration, three different sets are considered: safe set, potential minimizer set, and possible expander set. The shrinkAlgo algorithm and stageOpt algorithm are based on the safeOpt algorithm. For the first few chosen number of iterations, the framework is the same as the safeOpt algorithm, then, the optimization process is modified such that the optimizer becomes less exploratory. These modifications enable efficient identification of optimum regions within the control parameter space without necessitating the incorporation of models, although model integration is

feasible and can potentially further reduce the number of required iterations.

- *Exploration of control parameter space for low NO emissions.* It is a well-known fact that plasma discharges could enhance the production of NO. However, there could also be a situation where certain fuel splitting values between the first and second-stage flame of a sequential combustor emit low NO but are thermoacoustically unstable. By optimizing two control parameters, the power division between the flames and the generator voltage of NRPDs, the algorithms could find the optimum regions. It was found that without the help of NRPDs, putting more power on the second-stage flame would increase the acoustic pulsation. However, by increasing the generator voltage while keeping the PRF at 10 kHz, the pulsation was reduced. The region with low NO emissions and low acoustic pulsations was located where the power of the second stage was higher than 52% and the generator voltage was higher than 8.5 kV. Therefore, the application of NRPDs in a sequential combustor can help to find regions with low NO emissions.

Characterizing the response of the sequential flame requires the measurement of acoustic pressure, acoustic velocity, and temperature fluctuations. Both acoustic pressure and acoustic velocity could be reconstructed using the multi-microphone method. However, measuring temperature fluctuations with a frequency in the range of 100 to 600 Hz requires an advanced method. This issue is addressed in Chapter 4 by introducing tunable diode laser absorption spectroscopy with wavelength modulation spectroscopy (TDLAS-WMS) for measuring coherent temperature fluctuations. The method is employed to measure the entropy transfer function of a technically premixed turbulent swirled flame. The main findings of chapter 4 are listed as follows:

- *Measurement of low-amplitude coherent temperature fluctuations down to 5K.* The method employs fast modulation, on the order of 100 kHz, of the current powering the diode lasers. This modulation approach improves the ability to reject noise, as it shifts absorption information to higher frequencies where non-absorption related noise is significantly lower. The absorption information is then converted to temperature in the post-processing step at 5 kHz rate. Coherent temperature fluctuations were generated by forcing the flame with an upstream loudspeaker with frequencies ranging from 40 to 250 Hz. The lowest

measured amplitude of the coherent temperature fluctuations was around 5 K. High confidence in the accuracy of the method was achieved by measuring multiple operating conditions and comparing the consistency of the results.

- *The gain of the entropy transfer function does not decay monotonically with respect to frequency.* In contrast to studies in the literature, it was found that, for all the operating conditions considered, the measured entropy transfer functions do not decrease monotonically with respect to frequency. The trends resemble those of the flame transfer functions (FTFs) which are also measured simultaneously. The ETF curves collapse to each other when plotted against the Strouhal number, and the slope of the phase matches the convective time delay.

In practice, gas turbines often operate under varying load conditions. This motivated the study of the effectiveness of NRPDs in controlling thermoacoustics under transient operation at high pressure, which is explained in Chapter 5. The experiments were carried out in the high-pressure laboratory at CAPS LAB. The same CPSC configuration as that in the atmospheric study was placed inside a high pressure vessel. The main findings of chapter 5 are listed as follows:

- *Effective control of thermoacoustics under high-pressure and stationary operations.* The first part of the study involved the investigation of NRPDs under stationary conditions. The combustor pressure considered for the actuation of the NRPD ranges from 4 to 5.5 bar. In all combustor pressures, NRPDs can effectively stabilize the thermoacoustics. Remarkably, at the combustor pressure of 5.5, a mean plasma power of around 7.7×10^{-3} percent of the total thermal power of the flame is sufficient to effectively stabilize the thermoacoustics.
- *NRPDs allow smooth transient operation of the CPSC.* Two different transient scenarios are considered. In the first transient scenario, the combustor pressure is linearly increased from 4 to 5 bar, which corresponds to an increase in thermal power from 273 kW to 341 kW, while continuously employing NRPD to stabilize the system. In the second transient case, the combustor is operated at 5 bar, and the tunable outlet orifice of the sequential combustor progressively swept from 91.6 % to 100 % of its maximum area. In both cases the thermoacoustics are successfully stabilized. It was found that after NRPD actuation, the peak frequency of the acoustic spectra shifted to higher

frequency. This could be attributed to changes in the mean flame length.

This thesis has covered different aspects of thermoacoustic control in sequential combustor. However, there is scope for improvement and refinement. Future research could explore the following potential topics:

- *Entropy and flame transfer function of the sequential flame.* Measuring the entropy and flame transfer function of the sequential flame is essential to predict the thermoacoustic instabilities of the system. The TDLAS-WMS method developed in this thesis has demonstrated adequate capability to measure temperature fluctuations. As a result, it is principally possible to measure all relevant quantities. Experimental campaigns in this area are currently being planned.
- *Improvement of the safe Bayesian optimization algorithms.* The ability of the developed safe Bayesian optimization algorithms to find the global optimization depends on the choice of initial information. This problem could be tackled by adding an additional framework to allow algorithms to quickly assess unsafe regions. Upon evaluation of these unsafe regions, it is imperative that the algorithms rapidly analyze the objective and constraint functions, subsequently returning to the safe region. Consequently, the uncertainty associated with acquired information must be adjusted, considering the reduced duration of data collection. This approach may require more hyperparameters to be introduced; however, this will make the algorithm to be more independent of the initial safe set. Alternatively, if the measurement of the flame transfer function of the sequential flame is available, a low-order model could be constructed and incorporated into the algorithms.
- *The influence of fuel composition on NRPD effectiveness.* During experimental campaigns, NRPDs were observed to become less effective in controlling thermoacoustics under some fuel mixture conditions. In particular, when the sequential fuel is richer in natural gas. It would be valuable to meticulously study this effect through experiments and possibly plasma kinetic modeling.
- *Optimization of the electrodes geometry and location.* This study only considers electrodes with a pin-to-pin configuration. It would be interesting to investigate the configuration of different electrodes and

analyze their effectiveness. Furthermore, the location of the electrodes could be optimized as in the current configuration the sequential could be partially entering the mixing channel close to where the electrodes are. In addition, it would be interesting to place the electrode pairs at different locations to allow further adaptation to changes in operational conditions.

FEEDBACK CONTROL OF THERMOACOUSTIC IN A SEQUENTIAL COMBUSTOR WITH NRPD

This appendix discusses some preliminary findings of a feedback control implementation to control the acoustic pulsations of the sequential combustor described in Chapter 5 with NRPD. The combustor is operated at a mean pressure of 2 bar. The controller is similar to the gain-delay controller described in Chapter 3. An extended Kalman filter (EKF) is employed to estimate the instantaneous phase of the acoustic signal at the main frequency. The effect of the NRPD duty cycle and actuation delay on acoustic pressure pulsations and NO emissions is investigated.

A.1 INTRODUCTION

In this Appendix, a feedback-based controller, which is similar to the phase shifter controller in Chapter 3, is employed to actuate the NRPD in the high pressure sequential compressor. The two control parameters of the controller are the duty cycle and the actuation delay. In short, duty cycle refers to the percentage duration of the actuation signal compared to the reference acoustic cycle; e.g. duty cycle of 50 % means that the NRPD is actuated 50 % of the time within one acoustic cycle. In this implementation, the actuation delay or phase shift is expressed in degrees. Therefore, it is relative to the main frequency present in the system. The implementation is based on [54, 86] in which an extended Kalman filter (EKF) is used to estimate the instantaneous phase of the acoustic cycle, $\theta(t)$, from the microphone. When the value $\theta(t)$ is equal to the predefined phase shift ψ , a square wave with the width corresponding to the predefined duty cycle DC is generated. The square wave then acts as a gate signal for the plasma generator, i.e. plasma discharges will be initiated if the gate signal value is above zero.

In this study, the effect of both control parameters, DC and ψ , on the acoustic pressure pulsation and NO emissions is investigated. Because the emission analyzer requires about two minutes to converge, the NO emission mapping procedure with respect to the control parameters is aided by the Bayesian optimization algorithm described in Chapter 3. The

hyperparameters of the algorithm is tuned such that the goal is to optimize the information.

A.2 SETUP

A.2.1 Experimental setup

The experimental setup is similar to the one described in Chapter 5, hence, it will not be explained in detail in this section. The fuel of the first stage flame is pure natural gas with fuel and air massflows of 1.67 g/s and 35.9 g/s, respectively. The air is preheated up to 338 °C. The fuel for the second stage flame is a blend of hydrogen and natural gas with mass flows of 0.094 g/s and 1.29 g/s, respectively. The mass flow of the dilution air is 36.2 g/s.

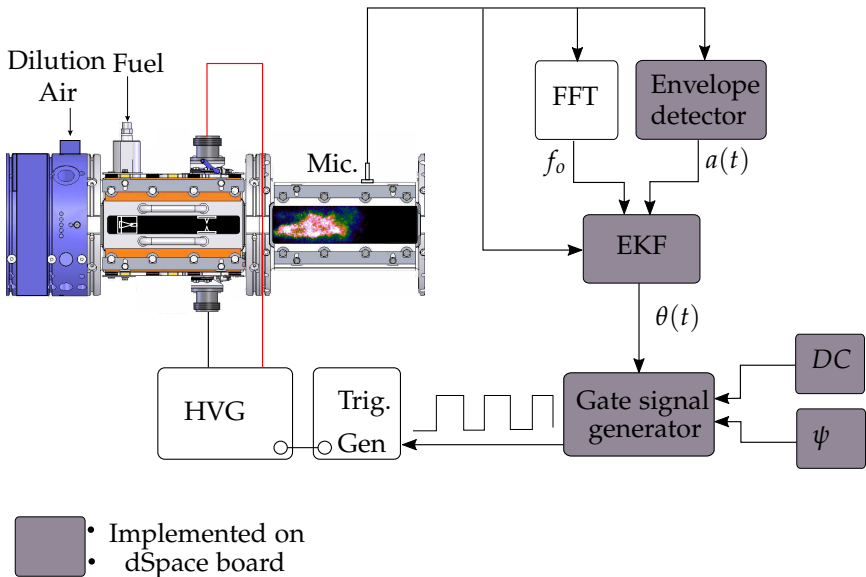


FIGURE A.1: Experimental setup showing only the second stage combustor and the signal chain diagram. The main experimental setup can be seen in Chapter 5 and Chapter 2. HVG: High voltage generator, Trig. Gen : Trigger generator, FFT: Fast Fourier Transform, DC: Duty cycle, ψ : Phase shift in degree, EKF: Extended Kalman filter. Elements in gray boxes are implemented on a dSpace board (DS1104). The FFT algorithm is not operating in real-time.

The simplified version of the experimental setup and the signal chain diagram of the feedback control implementation are shown in Figure A.1. The elements in gray boxes are implemented on a dSpace board (DS1104). The pulse repetition frequency (PRF) of the generator is fixed at 10 kHz. The generator voltage is set to ± 13.5 kV when $DC \leq 80\%$ and to ± 12.5 kV when continuous forcing is applied.

A.2.2 Extended Kalman filter

A detailed derivation of the Kalman filter equations can be seen in [159, 160]. Only the relevant equations are briefly outlined here. Because the implementation of the filter is on a dSpace board which works in a discrete time step, the state-space equations are written in discrete form. The time index is denoted by $k \in \mathbb{Z}^+$. The sampling time of the board, T_s , is 0.1 ms.

The states vector, \mathbf{x} , consists of the envelope of the acoustic pressure signal a , the peak frequency of the signal f_o , and the phase of the acoustic signal $\theta = 2\pi f_o k T_s$: $\mathbf{x} = [a \ f_o \ \theta]^T$. The measurement output vector \mathbf{y} consists of a , f_o , and the bandpass filtered acoustic pressure p : $\mathbf{y} = [a \ f_o \ p]^T$. The dynamic of the states, and the output measurement are described by the following equations:

$$\mathbf{x}_k = \mathbf{A}\mathbf{x}_{k-1} + \mathbf{w}_k, \quad \mathbf{w} \sim \mathcal{N}(0, \mathbf{Q}). \quad (\text{A.1})$$

$$\mathbf{y}_k = \mathbf{h}(\mathbf{x}_k) + \mathbf{v}_k, \quad \mathbf{v} \sim \mathcal{N}(0, \mathbf{R}), \quad (\text{A.2})$$

where \mathbf{w} is the process noise with zero mean and covariance matrix \mathbf{Q} , and \mathbf{v} is the measurement noise with zero mean and covariance matrix \mathbf{R} . The entries of the covariance matrices are hyperparameters of the filter that can be tuned. Following the procedure in [161], the transition matrix \mathbf{A} is assumed to have the following structure:

$$\mathbf{A} = \begin{bmatrix} 1 & 0 & 0 \\ 0 & 1 & 0 \\ 0 & 2\pi T_s & 1 \end{bmatrix}, \quad (\text{A.3})$$

the measurement function \mathbf{h} is expressed as:

$$\mathbf{h}(\mathbf{x}_k) = \begin{bmatrix} x_{1,k} \\ x_{2,k} \\ x_{1,k} \sin x_{2,k} \end{bmatrix}. \quad (\text{A.4})$$

Note that, in the measurement function above, the peak frequency, $x_{2,k} = f_o$, is assumed to be measured in real-time. However, as previously mentioned, the real-time FFT algorithm is not implemented. Hence, the frequency f_o is given as an adjustable input to the dSpace board that can be modified via a user interface software. During the experiment, a separate LabVIEW script is used to get the f_o and then the value is fed to the user interface software. This is similar to the implementation described in [54]. The benefit of including f_o in both the state and measurement vectors is that once the real-time FFT algorithm is feasible, the Kalman filter implementation does not have to be substantially changed.

Essentially, Kalman filter is a Bayesian solution to the problem of sequentially estimating the state of the dynamical system [159]. Because the noise is assumed to be Gaussian distributed, the close form solution of the posterior prediction could be attained. Due to the presence of noise, the estimates of the states also follow the Gaussian distributions. Let the subscript $k | k - 1$ denote the prior update step (**prediction step**) and the subscript $k | k$ denote the posterior update step after (**measurement update step**) including the output measurement. Furthermore, let $\hat{\mathbf{x}}$ and \mathbf{P} denote the mean and the covariance matrix of the state distribution, respectively. Assume that at time $k - 1$, the posterior mean, $\hat{\mathbf{x}}_{k-1|k-1}$ and the variance $\mathbf{P}_{k-1|k-1}$ are available. After performing the prediction step, the mean and covariance of the estimates of the states are expressed as follows:

$$\hat{\mathbf{x}}_{k|k-1} = \mathbf{A}\hat{\mathbf{x}}_{k-1|k-1}, \quad (\text{A.5})$$

$$\mathbf{P}_{k|k-1} = \mathbf{A}\mathbf{P}_{k-1|k-1}\mathbf{A}^T + \mathbf{Q}. \quad (\text{A.6})$$

In the measurement update step, the posterior distribution of the states is calculated by combining the measurement likelihood, which is derived from equation A.2, and the results from the prediction step. The posterior mean and covariance are then expressed as follows:

$$\hat{\mathbf{x}}_{k|k} = \hat{\mathbf{x}}_{k|k-1} + \mathbf{K}_k(\mathbf{y}_k - \mathbf{H}_k\hat{\mathbf{x}}_{k|k-1}), \quad (\text{A.7})$$

$$\mathbf{P}_{k|k} = \mathbf{P}_{k|k-1} - \mathbf{K}_k\mathbf{H}_k\mathbf{P}_{k|k-1}, \quad (\text{A.8})$$

where \mathbf{K}_k and \mathbf{H}_k are the optimal Kalman filter gain and the Jacobian matrix of the measurement function, respectively:

$$\mathbf{K}_k = \mathbf{P}_{k|k-1} \mathbf{H}_k^T (\mathbf{H}_k \mathbf{P}_{k|k-1} \mathbf{H}_k^T + \mathbf{R})^{-1}, \quad (\text{A.9})$$

$$\mathbf{H}_k = \left. \frac{\partial \mathbf{h}}{\partial \mathbf{x}} \right|_{\hat{\mathbf{x}}_{k|k-1}}. \quad (\text{A.10})$$

All equations are implemented on the dSpace board, which is programmed with SIMULINK. The controller parameters ψ and DC can be changed during the test via a user interface software. When $\theta(k) = \psi$, a square signal with a width of $DC \times 1/f_o$ is created and fed to the trigger generator.

A.3 RESULTS

The duty cycle and the phase shift are uniformly swept to see their effect on the acoustic pressure pulsations in the sequential combustion chamber. The duty cycle is swept from 10% to 80% and the phase shift is swept from 20° to 340°. Figure A.2 shows the frequency spectra of the acoustic pressure signal in four different combinations of control parameters. When no control is applied, the combustor exhibits high acoustic pressure pulsations of 168 dB at 370 Hz.

When the duty cycle is set to 10% and the phase shift is set to 160°, the peak frequency shifts to 327 Hz and the power is 148 dB, which is 20 dB less than the uncontrolled case. A secondary peak at around 410 Hz also presents in the signal. After analyzing the signal histogram of the bandpass-filtered signal around the peak frequency (not shown here), under this condition, the system remains linearly unstable despite a significant reduction in the pressure pulsations.

When the duty cycle is 80% and the phase shift is 140°, the peak frequency changes to 380 Hz with a power of 146 dB, which is 2 dB lower than the previous case. However, the plasma power is eight times more than in the previous case.

The best performance in terms of pulsation reduction is obtained when continuous forcing is applied. As seen, the peak around 370 Hz is completely eliminated.

To compare different combinations of control parameters, the measured signal is bandpass filtered, and subsequently the root mean squared (RMS) value is computed. The cut-on and cut-off frequencies of the bandpass filter are shown by the black dashed lines in Figure A.2.

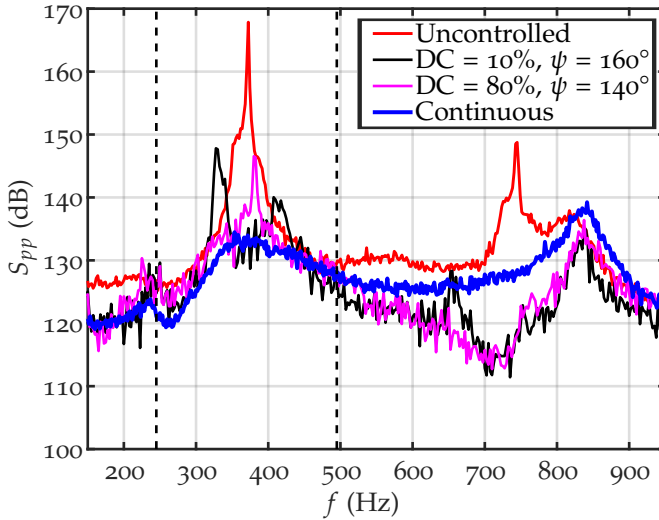


FIGURE A.2: Acoustic spectra of the pressure pulsations inside the sequential combustion chamber with different control parameters combinations. Continuous forcing is equivalent to $DC = 100\%$. The dashed lines show the frequency range of the bandpass filter for the RMS computation. The generator voltage in the continuous forcing case is set to ± 12.2 kV, whereas, in the feedback control strategy it is set to ± 13.5 kV.

The resulting acoustic pressure RMS (p'_{rms}) map as a function of the control parameters is shown in Figure A.3. The red and blue lines in Figure A.3 show the RMS pressure of the uncontrolled and continuous forcing cases, respectively. There are in total 153 measurement points, each with a recording length of four seconds to compute the RMS value. As can be seen, at every DC value, there is a notable minimum p'_{rms} located when $\psi = 140 - 180^\circ$.

On average, increasing the duty cycle leads to a decrease in the RMS value. It should be noted that for some DC , depending on the value of ψ , the acoustic pulsation could be higher than the uncontrolled case. The highest RMS value occurs at $DC = 10\%$ and $\psi = 20^\circ$, where the p'_{rms} is 91 mbar. The RMS value of the uncontrolled case is 63 mbar. The minimum value of p'_{rms} at $DC = 10\%$ is 14 mbar, whereas, at $DC = 80\%$, the minimum value is 11 mbar. The RMS value of the continuous forcing case is 7.8 mbar. However,

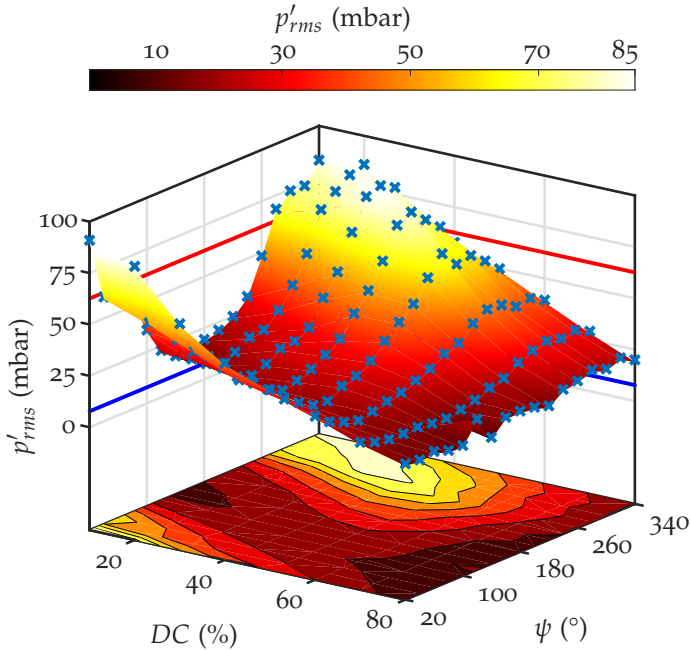


FIGURE A.3: Surface map of the acoustic RMS (root mean squared) pressure in the sequential combustion chamber as a function of the control parameters (duty cycle and phase shift). The crosses indicate the measurement points. The red line indicates the pressure RMS value without control, and the blue line shows the pressure RMS value with continuous forcing.

note that in the continuous forcing case, the voltage of the generator is ± 12.2 kV instead of ± 13.5 kV. Therefore, looking only at the values of p'_{rms} , it is more advantageous to apply the continuous forcing strategy instead of the feedback control, as it gives the lowest p'_{rms} without the need for hardware and software to implement the feedback controller. However, when NO emission is also part of the consideration, situations might change.

To obtain a surface map of the NO emission efficiently, the Bayesian optimization algorithm in Chapter 3 is tuned to maximize the information gain at every iteration. This is needed because the emission analyzer requires about two minutes to converge, and hence obtaining 153 measurement points as in the previous case is unfeasible. Figure A.4 shows the surface

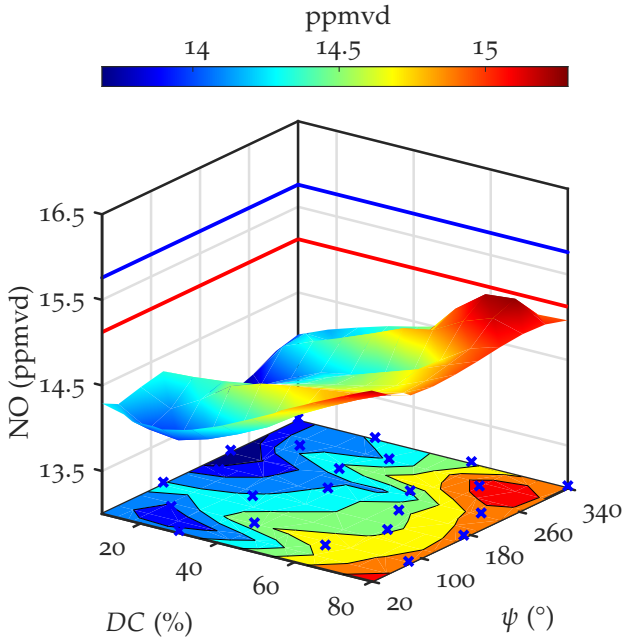


FIGURE A.4: Surface map of the NO emissions. The crosses indicate the measurement points. The red line indicates the NO emission without control, and the blue line shows NO emission with continuous forcing. The uncertainty of the emission analyzer in this range is ± 0.8 ppmvd.

map of NO emissions. The number of measurements is 26 for this case. Figure A.4 shows the resulting NO emission map. The uncertainty of the emission analyzer in this range is ± 0.8 ppmvd. The highest NO emission occurs when continuous forcing is applied, as shown by the blue line in Figure A.4. In the feedback forcing control case, NO emission increases on average as DC increases. Almost all of the measurement points with feedback control strategy have a lower NO emission compared to the controlled case. Therefore, this boils down to a trade-off between the p'_{rms} and the NO emission. For example, if NO emission is not allowed to exceed 15 ppmvd and the p'_{rms} safety threshold is 15 mbar, indeed the feedback control strategy with DC = 10% is the optimum choice, as at this condition, the power requirement for the plasma generator is also the lowest.

A.4 CONCLUSION AND OUTLOOK

The feedback control strategy has been implemented for the actuation of NRPD in sequential combustor operated at a mean pressure of 2 bar. The effect of the duty cycle and the phase shift of the controller on the acoustic pressure pulsations and NO emissions is studied.

Depending on the combination of control parameters, the pressure pulsations can be amplified instead of suppressed. The optimum choice for the controller phase change is between 140 and 160 °for all duty cycles. However, the continuous forcing strategy outperforms the feedback control strategy in terms of pulsation reductions. On the other hand, the continuous forcing strategy performs the worst in terms of NO emission. Hence, the trade-off between NO and p'_{rms} should be considered in the selection of the control strategy.

Future studies could include optimization of control parameters with the Bayesian algorithm described in Chapter 3. For example, NO emission could be treated as a constraint, and the objective is to minimize p'_{rms} , or vice versa. On the controller side, the real-time implementation of the FFT algorithm could be studied. Doing so would allow the controller to track the peak frequency of the acoustic pressure pulsation during, for example, transient changes in operating conditions.

BIBLIOGRAPHY

- [1] J. A. J. Gowlett. "The discovery of fire by humans: a long and convoluted process". In: *Philosophical Transactions of the Royal Society B: Biological Sciences* 371 (2016), p. 20150164.
- [2] Andrew C. Scott, William G. Chaloner, Claire M. Belcher, and Christopher I. Roos. "The interaction of fire and mankind: Introduction". In: *Philosophical Transactions of the Royal Society B: Biological Sciences* 371 (2016), p. 20150162.
- [3] Dietrich Eckardt. *Gas Turbine Powerhouse. The development of the power generation gas turbine at BBC-ABB-Alstom*. Oldenbourg Verlag Munchen, 2014.
- [4] "History of Combustion". In: *Combustion*. Ed. by Á.B. Palotás M. Lackner and F. Winter. John Wiley & Sons, Ltd, 2013. Chap. 1, pp. 1–17. ISBN: 9783527667185.
- [5] Hannah Ritchie, Pablo Rosado, and Max Roser. "Energy". In: *Our World in Data* (2023). <https://ourworldindata.org/energy>.
- [6] World Bank. *World Development Indicators*. Accessed on: December 12, 2023. 2023. URL: [%5Curl%7Bhttps://databank.worldbank.org/reports.aspx?source=2&series=SP.POP.TOTL&country=HIC#advancedDownloadOptions%7D](https://databank.worldbank.org/reports.aspx?source=2&series=SP.POP.TOTL&country=HIC#advancedDownloadOptions%7D).
- [7] Hannah Ritchie, Pablo Rosado, and Max Roser. "Energy Production and Consumption". In: *Our World in Data* (2020). URL: <https://ourworldindata.org/energy-production-consumption>.
- [8] International Energy Agency. *World Energy Outlook 2023*. Paris, 2023.
- [9] Hannah Ritchie, Pablo Rosado, and Max Roser. "CO₂ and Greenhouse Gas Emissions". In: *Our World in Data* (2023). URL: <https://ourworldindata.org/co2-and-greenhouse-gas-emissions>.
- [10] G. Peters, R. Andrew, J. Canadell, et al. "Key indicators to track current progress and future ambition of the Paris Agreement". In: *Nature Climate Change* 7 (2017), pp. 118–122.
- [11] International Energy Agency. *The Role of Gas in Today's Energy Transitions*. Paris, 2019.

- [12] Chao Chen, Ziming Yang, and Guoping Hu. "Signalling the cost of intermittency: What is the value of curtailed renewable power?" In: *Journal of Cleaner Production* 302 (2021), p. 126998.
- [13] J. Blondeau and J. Mertens. "Impact of intermittent renewable energy production on specific CO₂ and NO_x emissions from large scale gas-fired combined cycles". In: *Journal of Cleaner Production* 221 (2019), pp. 261–270.
- [14] Qusay Hassan, Sameer Algburi, Aws Zuhair Sameen, Hayder M. Salman, and Marek Jaszczur. "Green hydrogen: A pathway to a sustainable energy future". In: *International Journal of Hydrogen Energy* 50 (2024), pp. 310–333.
- [15] P. P. Edwards, V. L. Kuznetsov, and W. I.F. David. "Hydrogen energy". In: *Philosophical Transactions of the Royal Society A: Mathematical, Physical and Engineering Sciences* 365 (2007), pp. 1043–1056.
- [16] Omar J. Guerra, Jiazi Zhang, Joshua Eichman, Paul Denholm, Jennifer Kurtz, and Bri-Mathias Hodge. "The value of seasonal energy storage technologies for the integration of wind and solar power". In: *Energy Environ. Sci.* 13 (7 2020), pp. 1909–1922.
- [17] *Development of a Fuel Flexible H₂-Natural Gas Gas Turbine Combustion Technology Platform*. Vol. Volume 3B: Combustion, Fuels, and Emissions. Turbo Expo: Power for Land, Sea, and Air. June 2022, V03BT04A036.
- [18] Nikolaos Skordoulias, Efthymia Ioanna Koytsoumpa, and Sotirios Karellas. "Techno-economic evaluation of medium scale power to hydrogen to combined heat and power generation systems". In: *International Journal of Hydrogen Energy* 47 (2022), pp. 26871–26890.
- [19] Mirko R. Bothien, Andrea Ciani, John P. Wood, and Gerhard Fruechtel. "Toward Decarbonized Power Generation With Gas Turbines by Using Sequential Combustion for Burning Hydrogen". In: *Journal of Engineering for Gas Turbines and Power* 141 (2019), p. 121013.
- [20] Douglas A. Pennell, Mirko R. Bothien, Andrea Ciani, Victor Granet, Ghislain Singla, Steven Thorpe, Anders Wickstroem, Khalid Oumejjoud, and Matthew Yaquinto. "An introduction to the ansaldo GT36 constant pressure sequential combustor". In: *Proceedings of ASME Turbo Expo 2023* 4B (2017).

- [21] *Development of the Sequential Combustion System for the ABB GT24/GT26 Gas Turbine Family*. Vol. Volume 4: Heat Transfer; Electric Power; Industrial and Cogeneration. Turbo Expo: Power for Land, Sea, and Air. June 1996, V004T10A022.
- [22] *Second Generation Low-Emission Combustors for ABB Gas Turbines: Burner Development and Tests at Atmospheric Pressure*. Vol. Volume 3: Coal, Biomass and Alternative Fuels; Combustion and Fuels; Oil and Gas Applications; Cycle Innovations. Turbo Expo: Power for Land, Sea, and Air. June 1990, V003T06A031.
- [23] Oliver Schulz and Nicolas Noiray. "Autoignition flame dynamics in sequential combustors". In: *Combustion and Flame* 192 (2018), pp. 86–100.
- [24] "Chapter 1 - Introduction of self-sustained thermoacoustic instability". In: *Thermoacoustic Combustion Instability Control*. Ed. by Dan Zhao. Academic Press, 2023, pp. 1–112.
- [25] R. I. Sujith and Samadhan A. Pawar. "Introduction". In: *Thermoacoustic Instability: A Complex Systems Perspective*. Cham: Springer International Publishing, 2021, pp. 1–30.
- [26] Timothy C Lieuwen and Vigor Yang. *Combustion instabilities in gas turbine engines: operational experience, fundamental mechanisms and modeling*. Vol. 210. 2005, pp. 8–25. ISBN: 156347669X.
- [27] Nicolas Noiray. "Analyse linéaire et non-linéaire des instabilités de combustion : application aux systèmes à injection multipoints et stratégies de contrôle". Thèse de doctorat. Châtenay-Malabry: Ecole Centrale de Paris, 2007.
- [28] N. Noiray, D. Durox, T. Schuller, and S. Candel. "A unified framework for nonlinear combustion instability analysis based on the flame describing function". In: *Journal of Fluid Mechanics* 615 (2008), pp. 139–167.
- [29] B. Higgins. "On the sound produced by a current of hydrogen gas passing through a tube". In: *Journal of Natural Philosophy, Chemistry and the Arts* 1 (1802), pp. 129–131.
- [30] Rayleigh. "The explanation of certain acoustical phenomena". In: *Nature* 18 (1878), pp. 319–321.
- [31] J. W. S. Rayleigh. *The theory of sound: in two volumes*. Vol. 2. Macmillan, 1896.

- [32] J. C. Oefelein and V. Yang. "Comprehensive review of liquid-propellant combustion instabilities in F-1 engines". In: *Journal of Propulsion and Power* 9 (1993), pp. 657–677.
- [33] T. Poinso. "Prediction and control of combustion instabilities in real engines". In: *Proceedings of the Combustion Institute* 36 (2017), pp. 1–28.
- [34] Jesse Sewell and Peter Sobieski. "Monitoring of Combustion Instabilities: Calpine's Experience". In: *Combustion Instabilities In Gas Turbine Engines: Operational Experience, Fundamental Mechanisms, and Modeling*. Ed. by Timothy Lieuwen and Vigor Yang. American Institute of Aeronautics and Astronautics, 2005, pp. 611–634.
- [35] R. H. Cantrell and R. W. Hart. "Interaction between Sound and Flow in Acoustic Cavities: Mass, Momentum, and Energy Considerations". In: *The Journal of the Acoustical Society of America* 36 (July 1964), pp. 697–706.
- [36] R. Gaudron, D. Yang, and A. S. Morgans. "Acoustic Energy Balance During the Onset, Growth, and Saturation of Thermoacoustic Instabilities". In: *Journal of Engineering for Gas Turbines and Power* 143 (Mar. 2021), p. 041026.
- [37] Bruno Schuermans, Jonas Moeck, Audrey Blondé, Bayu Dharmaputra, and Nicolas Noiray. "The Rayleigh integral is always positive in steadily operated combustors". In: *Proceedings of the Combustion Institute* 39.4 (2023), pp. 4661–4669.
- [38] N. Noiray and A. Denisov. "A method to identify thermoacoustic growth rates in combustion chambers from dynamic pressure time series". In: *Proceedings of the Combustion Institute* 36 (2017), pp. 3843–3850.
- [39] Mirko Bothien Nicolas Noiray and Bruno Schuermans. "Investigation of azimuthal staging concepts in annular gas turbines". In: *Combustion Theory and Modelling* 15 (2011), pp. 585–606.
- [40] Nicolas Noiray. "Linear Growth Rate Estimation From Dynamics and Statistics of Acoustic Signal Envelope in Turbulent Combustors". In: *Journal of Engineering for Gas Turbines and Power* 139 (Oct. 2016), p. 041503.

- [41] E. Boujo and N. Noiray. “Robust identification of harmonic oscillator parameters using the adjoint Fokker–Planck equation”. In: *Proceedings of the Royal Society A: Mathematical, Physical and Engineering Sciences* 473 (2017), p. 20160894.
- [42] Bruno Schuermans. “Modeling and control of thermoacoustic instabilities”. PhD thesis. Lausanne: EPFL, 2003.
- [43] T. Emmert, S. Bomberg, S. Jaensch, and W. Polifke. “Acoustic and intrinsic thermoacoustic modes of a premixed combustor”. In: *Proceedings of the Combustion Institute* 36 (2017), pp. 3835–3842.
- [44] Alexander Avdonin, Stefan Jaensch, Camilo F. Silva, Matic Češnovar, and Wolfgang Polifke. “Uncertainty quantification and sensitivity analysis of thermoacoustic stability with non-intrusive polynomial chaos expansion”. In: *Combustion and Flame* 189 (2018), pp. 300–310.
- [45] Xingsi Han, Jingxuan Li, and Aimee S. Morgans. “Prediction of combustion instability limit cycle oscillations by combining flame describing function simulations with a thermoacoustic network model”. In: *Combustion and Flame* 162 (2015), pp. 3632–3647.
- [46] Francesco Gant, Birute Bunkute, and Mirko R. Bothien. “Reheat flames response to entropy waves”. In: *Proceedings of the Combustion Institute* 38 (2021), pp. 6271–6278.
- [47] M. Weilenmann, Y. Xiong, and N. Noiray. “On the dispersion of entropy waves in turbulent flows”. In: *Journal of Fluid Mechanics* 903 (2020), R1.
- [48] Bayu Dharmaputra, Sergey Shcherbanev, Audrey Blondé, Bruno Schuermans, and Nicolas Noiray. “Entropy transfer function measurement with tunable diode laser absorption spectroscopy”. In: *Proceedings of the Combustion Institute* 39 (2023), pp. 4621–4630.
- [49] Mirko Bothien, Demian Lauper, Yang Yang, and Alessandro Scarpato. “Reconstruction and Analysis of the Acoustic Transfer Matrix of a Reheat Flame From Large-Eddy Simulations”. In: *Journal of Engineering for Gas Turbines and Power* 141 (Oct. 2018), p. 021018.
- [50] Dan Zhao. “Chapter 6 - Active control of thermoacoustic instability”. In: *Thermoacoustic Combustion Instability Control*. Ed. by Dan Zhao. Academic Press, 2023, pp. 443–512.
- [51] N. Noiray, D. Durox, T. Schuller, and S. Candel. “Dynamic phase converter for passive control of combustion instabilities”. In: *Proceedings of the Combustion Institute* 32 II (2009), pp. 3163–3170.

- [52] Raghavan Pandalai and Hukam Mongia. "Combustion instability characteristics of industrial engine dry low emission combustion systems". In: *AIAA Meeting Paper* (1998), p. 3379.
- [53] M. Bothien, N. Noiray, and B. Schuermans. "A novel damping device for Broadband Attenuation of Low-frequency combustion pulsations in gas turbines". In: *Journal of Engineering Gas Turbine and Power* 136 (2014), p. 041504.
- [54] Jonas P. Moeck, Deanna A. Lacoste, Christophe O. Laux, and Christian Oliver Paschereit. "Control of combustion dynamics in a swirl-stabilized combustor with nanosecond repetitively pulsed discharges". In: *51st AIAA Aerospace Sciences Meeting including the New Horizons Forum and Aerospace Exposition 2013* (2013), pp. 1–11.
- [55] D. A. Lacoste, J. P. Moeck, D. Durox, C. O. Laux, and T. Schuller. "Effect of nanosecond repetitively pulsed discharges on the dynamics of a swirl-stabilized lean premixed flame". In: *Journal of Engineering Gas Turbine and Power* 135 (2013).
- [56] Alexander Fridman. "Introduction to Theoretical and Applied Plasma Chemistry". In: *Plasma Chemistry*. Cambridge University Press, 2008, pp. 1–11.
- [57] Sergey A. Shcherbanev, Quentin Malé, Bayu Dharmaputra, Roberto Solana-Pérez, and Nicolas Noiray. "Effect of plasma-flow coupling on the ignition enhancement with non-equilibrium plasma in a sequential combustor". In: *Journal of Physics D: Applied Physics* 55 (2022). ISSN: 13616463.
- [58] C O Laux, T G Spence, C H Kruger, and R N Zare. "Optical diagnostics of atmospheric pressure air plasmas". In: *Plasma Sources Science and Technology* 12 (2003), p. 125.
- [59] Andrey Starikovskiy and Nickolay Aleksandrov. "Plasma-assisted ignition and combustion". In: *Progress in Energy and Combustion Science* 39 (2013), pp. 61–110.
- [60] Yiguang Ju and Wenting Sun. "Plasma assisted combustion: Dynamics and chemistry". In: *Progress in Energy and Combustion Science* 48 (2015), pp. 21–83.

- [61] S Barbosa, G Pilla, DA Lacoste, P Scoufflaire, S Ducruix, CO Laux, and D Veynante. "Influence of nanosecond repetitively pulsed discharges on the stability of a swirled propane/air burner representative of an aeronautical combustor". In: *Philosophical Transactions of the Royal Society A: Mathematical, Physical and Engineering Sciences* 373.2048 (2015), p. 20140335.
- [62] D. A. Lacoste, D. A. Xu, J. P. Moeck, and C. O. Laux. "Dynamic response of a weakly turbulent lean-premixed flame to nanosecond repetitively pulsed discharges". In: *Proceedings of the Combustion Institute* 34 (2013), pp. 3259–3266.
- [63] N.A. Popov and S.M. Starikovskaia. "Relaxation of electronic excitation in nitrogen/oxygen and fuel/air mixtures: fast gas heating in plasma-assisted ignition and flame stabilization". In: *Progress in Energy and Combustion Science* 91 (2022), p. 100928.
- [64] Deanna A Lacoste. "Flames with plasmas". In: *Proceedings of the Combustion Institute* 39 (2023), pp. 5405–5428.
- [65] N. Popov. "Investigation of the mechanism for rapid heating of nitrogen and air in gas discharges". In: *Plasma Physics Reports* 27 (2001), pp. 886–896.
- [66] Mirko R. Bothien, Andrea Ciani, John P. Wood, and Gerhard Fruechtel. "Sequential Combustion in Gas Turbines: The Key Technology for Burning High Hydrogen Contents With Low Emissions". In: *Turbo Expo: Power for Land, Sea, and Air Volume 4A: Combustion, Fuels, and Emissions* (2019).
- [67] Andrea Ciani, Mirko Bothien, Birute Bunkute, John Wood, and Gerhard Fruechtel. "Superior fuel and operational flexibility of sequential combustion in Ansaldo Energia gas turbines". In: *Journal of the Global Power and Propulsion Society* 3 (2019), pp. 630–638.
- [68] Roberto Solana-Pérez, Sergey A Shcherbanev, Bayu Dharmaputra, Andrea Ciani, and Nicolas Noiray. "Combustion regime transition of H₂ flames during steady and transient operation of a sequential combustor". In: *Proceedings of the Combustion Institute* 39 (2023), pp. 4335–4344.
- [69] Oliver Schulz and Nicolas Noiray. "Combustion regimes in sequential combustors: Flame propagation and autoignition at elevated temperature and pressure". In: *Combustion and Flame* 205 (2019), pp. 253–268.

- [70] Giacomo Bonciolini and Nicolas Noiray. "Synchronization of Thermoacoustic Modes in Sequential Combustors". In: *Journal of Engineering Gas Turbine and Power* 141 (2018).
- [71] O. Schulz, U. Doll, D. Ebi, J. Droujko, C. Bourquard, and N. Noiray. "Thermoacoustic instability in a sequential combustor: Large eddy simulation and experiments". In: *Proceedings of the Combustion Institute* 37 (2019), pp. 5325–5332.
- [72] Yuan Xiong, Jessica Droujko, Oliver Schulz, and Nicolas Noiray. "Investigation of thermoacoustic instability in sequential combustor during first stage lean blow-off". In: *Proceedings of the Combustion Institute* 38 (2021), pp. 6165–6172.
- [73] Luigi Miniero, Georg A. Mensah, Claire Bourquard, and Nicolas Noiray. "Failure of thermoacoustic instability control due to periodic hot gas ingestion in Helmholtz dampers". In: *Journal of Sound and Vibration* 548 (2023), p. 117544.
- [74] Selma Zahirovic and Klaus Knapp. "Ansaldo GT26 Sequential Combustor Performance in Long-Term Commercial Operation". In: *Proceedings of the ASME Turbo Expo* 4B (2017), p. 64289.
- [75] Nicolas Docquier and Sébastien Candel. "Combustion control and sensors: A review". In: *Progress in Energy and Combustion Science* 28 (2002), pp. 107–150.
- [76] Ann P. Dowling and Aimee S. Morgans. "Feedback control of combustion oscillations". In: *Annual Review of Fluid Mechanics* 37 (2005), pp. 151–182.
- [77] Mirko R. Bothien, Jonas P. Moeck, and Christian Oliver Paschereit. "Active control of the acoustic boundary conditions of combustion test rigs". In: *Journal of Sound and Vibration* 318 (2008), pp. 678–701.
- [78] J. Hermann, S. Gleis, and D. Vortmeyer. "Active instability control (AIC) of spray combustors by modulation of the liquid fuel flow rate". In: *Combustion Science and Technology* 118 (1996), pp. 1–25.
- [79] J. R. Seume, N. Vortmeyer, W. Krause, J. Hermann, C.-C. Hantschk, P. Zangl, S. Gleis, D. Vortmeyer, and A. Orthmann. "Application of Active Combustion Instability Control to a Heavy Duty Gas Turbine". In: *Journal of Engineering Gas Turbine and Power* 120 (1998), pp. 721–726.

- [80] Deanna A. Lacoste, Yuan Xiong, Jonas P. Moeck, Suk Ho Chung, William L. Roberts, and Min Suk Cha. "Transfer functions of laminar premixed flames subjected to forcing by acoustic waves, AC electric fields, and non-thermal plasma discharges". In: *Proceedings of the Combustion Institute* 36 (2017), pp. 4183–4192.
- [81] Wookyung Kim and Jeffrey Cohen. "Plasma-Assisted Combustor Dynamics Control at Realistic Gas Turbine Conditions". In: *Combustion Science and Technology* 193 (2021), pp. 869–888.
- [82] Yuan Xiong, Oliver Schulz, Claire Bourquard, Markus Weilenmann, and Nicolas Noiray. "Plasma enhanced auto-ignition in a sequential combustor". In: *Proceedings of the Combustion Institute* 37 (2019), pp. 5587–5594.
- [83] Francesco Di Sabatino and Deanna A. Lacoste. "Enhancement of the lean stability and blow-off limits of methane-air swirl flames at elevated pressures by nanosecond repetitively pulsed discharges". In: *Journal of Physics D: Applied Physics* 53 (2020).
- [84] Francesco Di Sabatino, Thibault F Guiberti, Jonas P Moeck, William L Roberts, and Deanna A Lacoste. "Actuation efficiency of nanosecond repetitively pulsed discharges for plasma-assisted swirl flames at pressures up to 3 bar". In: 54 (2020), p. 075208.
- [85] Wookyung Kim, Jordan Snyder, and Jeffrey Cohen. "Plasma assisted combustor dynamics control". In: *Proceedings of the Combustion Institute* 35 (2015), pp. 3479–3486.
- [86] Ammar M Alkhalifa, Abdulrahman Alsalem, Davide Del Cont-Bernard, and Deanna A Lacoste. "Active control of thermoacoustic fluctuations by nanosecond repetitively pulsed glow discharges". In: *Proceedings of the Combustion Institute* 39 (2023), pp. 5429–5437.
- [87] DL Rusterholtz, DA Lacoste, GD Stancu, DZ Pai, and CO Laux. "Ultrafast heating and oxygen dissociation in atmospheric pressure air by nanosecond repetitively pulsed discharges". In: *Journal of Physics D: Applied Physics* 46 (2013), p. 464010.
- [88] N Q Minesi, V P Blanchard, E Pannier, G D Stancu, and C O Laux. "Plasma-assisted combustion with nanosecond discharges. I: Discharge effects characterization in the burnt gases of a lean flame". In: *Plasma Sources Science and Technology* 31 (2022), p. 045029.

- [89] W. Kim, H. Do, M. G. Mungal, and M. A. Cappelli. "Flame stabilization enhancement and NO_x production using ultra short repetitively pulsed plasma discharges". In: *Collection of Technical Papers - 44th AIAA Aerospace Sciences Meeting* 9 (2006), pp. 6770–6772.
- [90] Liang Yu, B. Aravind, and Deanna A. Lacoste. "Mitigating the response of premixed swirl flames to acoustic excitation by nanosecond repetitively pulsed discharges at elevated pressures". In: *Combustion and Flame* 256 (2023), p. 112944.
- [91] Kah Joon Yong, Maximilian Meindl, Wolfgang Polifke, and Camilo F. Silva. "Thermoacoustic Spectrum of a Swirled Premixed Combustor With Partially Reflecting Boundaries". In: *Journal of Engineering for Gas Turbines and Power* 142 (Nov. 2019), p. 011005.
- [92] Ann P. Dowling and Simon R. Stow. "Acoustic Analysis of Gas Turbine Combustors". In: *Journal of Propulsion and Power* 19 (2003), pp. 751–764.
- [93] Giulio Ghirardo, Matthew P. Juniper, and Mirko R. Bothien. "The effect of the flame phase on thermoacoustic instabilities". In: *Combustion and Flame* 187 (2018), pp. 165–184.
- [94] "Low order modelling of thermoacoustic instabilities and intermittency: Flame response delay and nonlinearity". In: *Combustion and Flame* 226 (2021), pp. 396–411.
- [95] Max Meindl, Malte Merk, Fabian Fritz, and Wolfgang Polifke. "Determination of Acoustic Scattering Matrices from Linearized Compressible Flow Equations with Application to Thermoacoustic Stability Analysis". In: *Journal of Theoretical and Computational Acoustics* 27 (2019), p. 1850027.
- [96] Geo A. Richards, Douglas L. Straub, and Edward H. Robey. "Passive Control of Combustion Dynamics in Stationary Gas Turbines". In: *Journal of Propulsion and Power* 19 (2003), pp. 795–810.
- [97] Geo. Richards and Douglas. Straub. "Passive Control of Combustion Instabilities in Stationary Gas Turbines". In: *Combustion Instabilities In Gas Turbine Engines: Operational Experience, Fundamental Mechanisms, and Modeling*. Ed. by Timothy Lieuwen and Vigor Yang. American Institute of Aeronautics and Astronautics, 2005, pp. 533–579.

- [98] V. Bellucci, P. Flohr, C. O. Paschereit, and F. Magni. "On the use of Helmholtz resonators for damping acoustic pulsations in industrial gas turbines". In: *Journal of Engineering Gas Turbine and Power* 126 (2004), pp. 271–275.
- [99] C. Bourquard and N. Noiray. "Stabilization of acoustic modes using Helmholtz and Quarter-Wave resonators tuned at exceptional points". In: *Journal of Sound and Vibration* 445 (2019), pp. 288–307.
- [100] Jeffery A. Lovett and Kevin T. Uznanski. "Prediction of Combustion Dynamics in a Staged Premixed Combustor". In: *Turbo Expo 2002: Power for Land, Sea, and Air; 2002 June 3-6; Amsterdam (The Netherlands)*. Vol. Volume 1: Turbo Expo 2002. The American Society of Mechanical Engineers, 2009, pp. 807–815.
- [101] Peter Berenbrink and Stefan Hoffmann. "Suppression of Dynamic Combustion Instabilities by Passive and Active Means". In: *Turbo Expo 2000: Power for Land, Sea, and Air; 2000 May 8-11; Munich (Germany)*. Vol. Volume 2: Coal, Biomass and Alternative Fuels; Combustion and Fuels; Oil and Gas Applications; Cycle Innovations. The American Society of Mechanical Engineers, 2014, V002T02A001.
- [102] Eirik Æsøy, Håkon T. Nygård, Nicholas A. Worth, and James R. Dawson. "Tailoring the gain and phase of the flame transfer function through targeted convective-acoustic interference". In: *Combustion and Flame* 236 (2022), p. 111813.
- [103] Jakob. Hermann and Stefan Hoffmann. "Implementation of Active Control in a Full-Scale Gas-Turbine Combustor". In: *Combustion Instabilities In Gas Turbine Engines: Operational Experience, Fundamental Mechanisms, and Modeling*. Ed. by Timothy Lieuwen and Vigor Yang. American Institute of Aeronautics and Astronautics, 2005, pp. 611–634.
- [104] Gregor Gelbert, Jonas P. Moeck, Mirko R. Bothien, Rudibert King, and Christian Oliver Paschereit. "Model predictive control of thermoacoustic instabilities in a swirl-stabilized combustor". In: *46th AIAA Aerospace Sciences Meeting and Exhibit; 2008 Jan 7-10; Reno, Nevada*. January. American Institute of Aeronautics and Astronautics, 2012. ISBN: 9781563479373.
- [105] Max Schwenzer, Muzaffer Ay, Thomas Bergs, and Dirk Abel. "Review on model predictive control: an engineering perspective". In: *International Journal of Advanced Manufacturing Technology* 117 (2021), pp. 1327–1349.

- [106] J. P. Moeck. "Analysis, modeling, and control of thermoacoustic instabilities". In: *Analysis, modeling, and control of thermoacoustic instabilities* (2010).
- [107] Hongzhi Zhu, Fanglong Weng, Makeximu, Donghai Li, and Min Zhu. "Active control of combustion oscillation with active disturbance rejection control (ADRC) method". In: *Journal of Sound and Vibration* 540 (2022), p. 117245.
- [108] Jingqing Han. "From PID to active disturbance rejection control". In: *IEEE Transactions on Industrial Electronics* 56 (2009), pp. 900–906.
- [109] Sezai Tokat, M. Sami Fadali, and Osman Eray. "A Classification and Overview of Sliding Mode Controller Sliding Surface Design Methods". In: *Recent Advances in Sliding Modes: From Control to Intelligent Mechatronics*. Ed. by Xinghuo Yu and Mehmet Önder Efe. Cham: Springer International Publishing, 2015, pp. 417–439.
- [110] Bayu Dharmaputra, Sergey Shcherbanev, Bruno Schuermans, and Nicolas Noiray. "Thermoacoustic stabilization of a sequential combustor with ultra-low-power nanosecond repetitively pulsed discharges". In: *Combustion and Flame* 258 (2023), p. 113101. ISSN: 0010-2180.
- [111] Felix Berkenkamp, Angela P. Schoellig, and Andreas Krause. "Safe controller optimization for quadrotors with Gaussian processes". In: *2016 IEEE International Conference on Robotics and Automation (ICRA)*. 2016, pp. 491–496.
- [112] Felix Berkenkamp, Andreas Krause, and Angela P. Schoellig. "Bayesian optimization with safety constraints: safe and automatic parameter tuning in robotics". In: *Machine Learning* 112.10 (2023), pp. 3713–3747.
- [113] Mohammad Khosravi, Christopher König, Markus Maier, Roy S. Smith, John Lygeros, and Alisa Rupenyan. "Safety-Aware Cascade Controller Tuning Using Constrained Bayesian Optimization". In: *IEEE Transactions on Industrial Electronics* 70 (2023), pp. 2128–2138.
- [114] Johann Moritz Reumschüssel, Jakob G R Von Saldern, Bernhard Čosić, and Christian Oliver Paschereit. "Multi-Objective Experimental Combustor Development Using Surrogate Model-Based Optimization". In: *Journal of Engineering Gas Turbine and Power* 146 (Nov. 2023), p. 031001.

- [115] Carl Edward Rasmussen and Christopher K. I. Williams. *Gaussian Processes for Machine Learning*. The MIT Press, Nov. 2005. ISBN: 9780262256834.
- [116] Adam D. Bull. “Convergence Rates of Efficient Global Optimization Algorithms”. In: *Journal of Machine Learning Research* 12.88 (2011), pp. 2879–2904.
- [117] Yanan Sui, Alkis Gotovos, Joel Burdick, and Andreas Krause. “Safe Exploration for Optimization with Gaussian Processes”. In: *Proceedings of the 32nd International Conference on Machine Learning*. Ed. by Francis Bach and David Blei. Vol. 37. Proceedings of Machine Learning Research. Lille, France: PMLR, 2015, pp. 997–1005.
- [118] Yanan Sui, Vincent Zhuang, Joel Burdick, and Yisong Yue. “Stage-wise Safe Bayesian Optimization with Gaussian Processes”. In: *Proceedings of the 35th International Conference on Machine Learning*. Ed. by Jennifer Dy and Andreas Krause. Vol. 80. Proceedings of Machine Learning Research. PMLR, 2018, pp. 4781–4789.
- [119] Andreas Krause and Cheng Ong. “Contextual Gaussian Process Bandit Optimization”. In: *Advances in Neural Information Processing Systems*. Ed. by J. Shawe-Taylor, R. Zemel, P. Bartlett, F. Pereira, and K.Q. Weinberger. Vol. 24. Curran Associates, Inc., 2011.
- [120] Bruno Schuermans, Felix Guethe, Douglas Pennell, Daniel Guyot, and Christian Oliver Paschereit. “Thermoacoustic Modeling of a Gas Turbine Using Transfer Functions Measured Under Full Engine Pressure”. In: *Journal of Engineering Gas Turbine and Power* 132 (Aug. 2010), p. 111503.
- [121] Hervé Lissek, Romain Boulandet, and Romain Fleury. “Electroacoustic absorbers: Bridging the gap between shunt loudspeakers and active sound absorption”. In: *The Journal of the Acoustical Society of America* 129 (2011), pp. 2968–2978.
- [122] Etienne Rivet, Sami Karkar, and Hervé Lissek. “Multi-degree-of-freedom low-frequency electroacoustic absorbers through coupled resonators”. In: *Applied Acoustics* 132 (2018), pp. 109–117.
- [123] Ann P. Dowling and Yasser Mahmoudi. “Combustion noise”. In: *Proceedings of the Combustion Institute* 35 (2015), pp. 65–100.
- [124] “Compositional and entropy indirect noise generated in subsonic non-isentropic nozzles”. In: *Journal of Fluid Mechanics* (2021).

- [125] "Prediction of combustion noise for an aeroengine combustor". In: *J. Propuls. Power* 30 (2014), pp. 114–122.
- [126] Markus Weilenmann, Ulrich Doll, Rolf Bombach, Audrey Blondé, Dominik Ebi, Yuan Xiong, and Nicolas Noiray. "Linear and nonlinear entropy-wave response of technically-premixed jet-flames-array and swirled flame to acoustic forcing". In: *Proceedings of the Combustion Institute* 38 (2021), pp. 6135–6143.
- [127] M. Weilenmann and N. Noiray. "Experiments on sound reflection and production by choked nozzle flows subject to acoustic and entropy waves". In: *Journal of Sound and Vibration* 492 (2021).
- [128] Chee Su Goh and Aimee S. Morgans. "The influence of entropy waves on the thermoacoustic stability of a model combustor". In: *Combustion Science and Technology* 185 (2013), pp. 249–268.
- [129] Andrea Giusti, Nicholas A. Worth, Epaminondas Mastorakos, and Ann P. Dowling. "Experimental and numerical investigation into the propagation of entropy waves". In: *AIAA Journal* 55 (2017), pp. 446–458.
- [130] Dominik Wassmer, Bruno Schuermans, Christian Oliver Paschereit, and Jonas P. Moeck. "Measurement and modeling of the generation and the transport of entropy waves in a model gas turbine combustor". In: *International Journal of Spray and Combustion Dynamics* 9 (2017), pp. 299–309.
- [131] Francesca De Domenico, Priyav Shah, Steven M. Lowe, Luming Fan, Paul Ewart, Benjamin A. O. Williams, and Simone Hochgreb. "High Frequency Measurement of Temperature and Composition Spots With LITGS". In: *Journal of Engineering Gas Turbine and Power* 141 (Oct. 2018).
- [132] Guoqing Wang, Xunchen Liu, Sirui Wang, Lei Li, and Fei Qi. "Experimental investigation of entropy waves generated from acoustically excited premixed swirling flame". In: *Combustion and Flame* 204 (2019), pp. 85–102.
- [133] Gregory B. Rieker, Jay B. Jeffries, and Ronald K. Hanson. "Calibration-free wavelength-modulation spectroscopy for measurements of gas temperature and concentration in harsh environments". In: *Applied Optics* 48 (2009), p. 5546.

- [134] Christopher S. Goldenstein, R. Mitchell Spearrin, Jay B. Jeffries, and Ronald K. Hanson. "Infrared laser-absorption sensing for combustion gases". In: *Progress in Energy and Combustion Science* 60 (2017), pp. 132–176.
- [135] Ritobrata Sur, Kai Sun, Jay B. Jeffries, John G. Socha, and Ronald K. Hanson. "Scanned-wavelength-modulation-spectroscopy sensor for CO, CO₂, CH₄ and H₂O in a high-pressure engineering-scale transport-reactor coal gasifier". In: *Fuel* 150 (2015), pp. 102–111.
- [136] Christopher S. Goldenstein, Christopher A. Almodóvar, Jay B. Jeffries, Ronald K. Hanson, and Christopher M. Brophy. "High-bandwidth scanned-wavelength-modulation spectroscopy sensors for temperature and H₂O in a rotating detonation engine". In: *Measurement Science and Technology* 25 (2014).
- [137] Garrett Mathews and Christopher Goldenstein. "Near-GHz scanned-wavelength-modulation spectroscopy for MHz thermometry and H₂O measurements in aluminized fireballs of energetic materials". In: *Applied Physics B* 126 (2020).
- [138] C S Goldenstein, R M Spearrin, I A Schultz, J B Jeffries, and R K Hanson. "Wavelength-modulation spectroscopy near 1.4 μm for measurements of H₂O and temperature in high-pressure and -temperature gases". In: *Measurement Science and Technology* 25 (2014), p. 055101.
- [139] Ronald K. Hanson, R. Mitchell Spearrin, and Christopher S. Goldenstein. *Spectroscopy and optical diagnostics for gases*. Springer, 2016, pp. 1–279.
- [140] Aimee S. Morgans, Chee Su Goh, and Jeremy A. Dahan. "The dissipation and shear dispersion of entropy waves in combustor thermoacoustics". In: *Journal of Fluid Mechanics* 733 (2013), R2.
- [141] Lin Strobio Chen, Sebastian Bomberg, and Wolfgang Polifke. "Propagation and generation of acoustic and entropy waves across a moving flame front". In: *Combustion and Flame* 166 (2016), pp. 170–180.
- [142] Richard Bluemner, Christian O. Paschereit, and Kilian Oberleithner. "Generation and transport of equivalence ratio fluctuations in an acoustically forced swirl burner". In: *Combustion and Flame* 209 (2019), pp. 99–116.

- [143] C. O. Paschereit, B. Schuermans, W. Polifke, and O. Mattson. "Measurement of Transfer Matrices and Source Terms of Premixed Flames". In: *Journal of Engineering Gas Turbine and Power* 124 (Mar. 2002), pp. 239–247.
- [144] Thomas Steinbacher, Max Meindl, and Wolfgang Polifke. "Modelling the generation of temperature inhomogeneities by a premixed flame". In: *International Journal of Spray and Combustion Dynamics* 10 (2018), pp. 111–130.
- [145] "Analysis of the pressure fields in a swirling annular jet flow". In: *Exp Fluids* 58 (2017), pp. 1–13.
- [146] Bernhard C. Bobusch, Bernhard Ćosić, Jonas P. Moeck, and Christian Oliver Paschereit. "Optical Measurement of Local and Global Transfer Functions for Equivalence Ratio Fluctuations in a Turbulent Swirl Flame". In: *Journal of Engineering Gas Turbine and Power* 136 (Nov. 2013).
- [147] Jocelino Rodrigues, Andrea Busseti, and Simone Hochgreb. "Numerical investigation on the generation, mixing and convection of entropic and compositional waves in a flow duct". In: *Journal of Sound and Vibration* 472 (2020), p. 115155.
- [148] Loizos Christodoulou, Nader Karimi, Andrea Cammarano, Manosh Paul, and Salvador Navarro-Martinez. "State prediction of an entropy wave advecting through a turbulent channel flow". In: *Journal of Fluid Mechanics* 882 (2020).
- [149] Alexander J. Eder, Bayu Dharmaputra, Marcel Désor, Camilo F. Silva, Alex M. Garcia, Bruno Schuermans, Nicolas Noiray, and Wolfgang Polifke. "Generation of Entropy Waves by Fully Premixed Flames in a Non-Adiabatic Combustor With Hydrogen Enrichment". In: *Journal of Engineering Gas Turbine and Power* 145.11 (2023), p. 111001.
- [150] Roberto Solana-Pérez, Sergey A. Shcherbanev, Bayu Dharmaputra, Andrea Ciani, and Nicolas Noiray. "Combustion regime transition of H₂ flames during steady and transient operation of a sequential combustor". In: *Proceedings of the Combustion Institute* (2022).
- [151] Giacomo Bonciolini, Dominik Ebi, Ulrich Doll, Markus Weilenmann, and Nicolas Noiray. "Effect of wall thermal inertia upon transient thermoacoustic dynamics of a swirl-stabilized flame". In: *Proceedings of the Combustion Institute* 37 (2019), pp. 5351–5358.

- [152] Giacomo Bonciolini and Nicolas Noiray. “Bifurcation dodge: avoidance of a thermoacoustic instability under transient operation”. In: *Nonlinear Dynamics* 96 (2019), pp. 703–716.
- [153] John Strollo, Stephen Peluso, and Jacqueline O’Connor. “Effect of hydrogen on steady-state and transient combustion instability characteristics”. In: *Journal of Engineering for Gas Turbines and Power* 143 (2021).
- [154] Byeonguk Ahn, Thomas Indlekofer, James Dawson, and Nicholas Worth. “Transient Thermo-Acoustic Responses of Methane/Hydrogen Flames in a Pressurized Annular Combustor”. In: *Journal of Engineering for Gas Turbines and Power* 144 (2022).
- [155] B Aravind, Liang Yu, and Deanna Lacoste. “Enhancement of lean blowout limits of swirl stabilized $\text{NH}_3\text{-CH}_4\text{-Air}$ flames using nanosecond repetitively pulsed discharges at elevated pressures”. In: *Applications in Energy and Combustion Science* 16 (2023), p. 100225.
- [156] Guillaume Vignat, Nicolas Minesi, Preethi Rajendram Soundararajan, Daniel Durox, Antoine Renaud, Victorien Blanchard, Christophe O. Laux, and Sébastien Candel. “Improvement of lean blow out performance of spray and premixed swirled flames using nanosecond repetitively pulsed discharges”. In: *Proceedings of the Combustion Institute* 38 (2021), pp. 6559–6566.
- [157] Jonas Moeck, Mirko Bothien, Christian Paschereit, Gregor Gelbert, and Rudibert King. “Two-Parameter Extremum Seeking for Control of Thermoacoustic Instabilities and Characterization of Linear Growth”. In: *45th AIAA Aerospace Sciences Meeting and Exhibit*.
- [158] G. Bonciolini, A. Faure-Beaulieu, C. Bourquard, and N. Noiray. “Low order modelling of thermoacoustic instabilities and intermittency: Flame response delay and nonlinearity”. In: *Combustion and Flame* 226 (2021), pp. 396–411.
- [159] Narayan Kovvali, Mahesh Banavar, and Andreas Spanias. *An Introduction to Kalman Filtering with MATLAB Examples*. Springer Cham, 2013.
- [160] Charles K. Chui and Guanrong Chen. *Kalman Filtering: with Real-Time Applications*. 5th. Springer Publishing Company, Incorporated, 2017. ISBN: 3319476106.

- [161] Mark Pastoor, Lars Henning, Bernd R. Noack, Rudibert King, and Gilead Tadmor. “Feedback shear layer control for bluff body drag reduction”. In: *Journal of Fluid Mechanics* 608 (2008), pp. 161–196.

CURRICULUM VITAE

PERSONAL DATA

Name Bayu Adi Dharmaputra
Date of Birth September 13, 1995
Place of Birth Malang, Indonesia
Citizen of Indonesia

EDUCATION

2016 – 2019 ETH Zurich
Zurich, Switzerland
Final degree: Master of Science ETH

2013 – 2016 University of Twente,
Enschede, Netherlands
Final degree: Bachelor of Science

EMPLOYMENT

March 2018 – September 2018 Intern, R&D Turbocharger Solutions
ABB Turbosystem,
Baden, Switzerland

PUBLICATIONS

Articles in peer-reviewed journals:

- [1] Bayu Dharmaputra, Sergey Shcherbanev, Bruno Schuermans, and Nicolas Noiray. "Thermoacoustic stabilization of a sequential combustor with ultra-low-power nanosecond repetitively pulsed discharges". In: *Combustion and Flame* 258 (2023), p. 113101. ISSN: 0010-2180.
- [2] Bayu Dharmaputra, Sergey Shcherbanev, Audrey Blondé, Bruno Schuermans, and Nicolas Noiray. "Entropy transfer function measurement with tunable diode laser absorption spectroscopy". In: *Proceedings of the Combustion Institute* 39 (2023), pp. 4621–4630.
- [3] Bayu Dharmaputra, Pit Reckinger, Bruno Schuermans, and Nicolas Noiray. "BOATS: Bayesian Optimization for Active control of ThermoacousticS". In: *Journal of Sound and Vibration* 582 (2024), p. 118415.
- [4] Alexander J. Eder, Bayu Dharmaputra, Marcel Désor, Camilo F. Silva, Alex M. Garcia, Bruno Schuermans, Nicolas Noiray, and Wolfgang Polifke. "Generation of Entropy Waves by Fully Premixed Flames in a Non-Adiabatic Combustor With Hydrogen Enrichment". In: *Journal of Engineering Gas Turbine and Power* 145.11 (2023), p. 111001.
- [5] Roberto Solana-Pérez, Sergey A Shcherbanev, Bayu Dharmaputra, Andrea Ciani, and Nicolas Noiray. "Combustion regime transition of H₂ flames during steady and transient operation of a sequential combustor". In: *Proceedings of the Combustion Institute* 39 (2023), pp. 4335–4344.
- [6] Sergey A. Shcherbanev, Quentin Malé, Bayu Dharmaputra, Roberto Solana-Pérez, and Nicolas Noiray. "Effect of plasma-flow coupling on the ignition enhancement with non-equilibrium plasma in a sequential combustor". In: *Journal of Physics D: Applied Physics* 55 (2022). ISSN: 13616463.
- [7] Quentin Malé, Nicolas Barléon, Sergey Shcherbanev, Bayu Dharmaputra, and Nicolas Noiray. "Numerical study of nitrogen oxides chemistry during plasma assisted combustion in a sequential combustor". In: *Combustion and Flame* 260 (2024), p. 113206.

- [8] Bruno Schuermans, Jonas Moeck, Audrey Blondé, Bayu Dharmaputra, and Nicolas Noiray. “The Rayleigh integral is always positive in steadily operated combustors”. In: *Proceedings of the Combustion Institute* 39.4 (2023), pp. 4661–4669.

Articles under review process:

- [1] Bayu Dharmaputra, Sergey Shcherbanev, and Nicolas Noiray. “Plasma-assisted thermoacoustic stabilization of transiently operated sequential combustor at high pressure”. In: *Submitted to Proceedings of the combustion institute* (2023).
- [2] Alexander Eder, Bayu Dharmaputra, Alex Garcia, Camilo Silva, and Wolfgang Polifke. “Identification of entropy waves in a partially premixed combustor”. In: *Submitted to Proceedings of the combustion institute* (2023).

Articles in preparation:

- [1] Bayu Dharmaputra, Bruno Schuermans, and Nicolas Noiray. *On The Causality of Flame Transfer Function Model*.
- [2] Tobias Sugandi, Bayu Dharmaputra, and Nicolas Noiray. *A deep operator network for Bayesian parameter identification in thermoacoustics*.
- [3] Audrey Blondé, Bruno Schuermans, Bayu Dharmaputra, and Nicolas Noiray. *Experiments and Modelling on the Effect of a Tunable Boundary on Thermoacoustic Stability*.

Conference contributions:

- [1] Bayu Dharmaputra, Alain Williner, Bruno Schuermans, and Nicolas Noiray. “Bayesian Optimization Based Adaptive Control of Thermoacoustic Instabilities”. In: 51st International Congress and Exposition on Noise Control Engineering (INTER-NOISE 2022); Glasgow, United Kingdom; August 21-24, 2022. Institute of Noise Control Engineering, pp. 1736–1743.
- [2] Sergey Shcherbanev, Bayu Dharmaputra, Roberto Solana Pérez, and Nicolas Noiray. “Flame stabilization with nanosecond repetitively pulsed discharge in a sequential combustor”. In: AIAA SCITECH Forum 2022; San Diego, CA, USA; January 3–7, 2022. American Institute of Aeronautics and Astronautics, AIAA 2022–2254.

- [3] Bayu Dharmaputra, Yuan Xiong, Sergey A. Shcherbanev, Audrey Blondé, and Nicolas Noiray. “Entropy Waves Measurement by Tunable Diode Laser Absorption Spectroscopy”. In: AIAA SCITECH Forum 2022; San Diego, CA, USA; January 3–7, 2022. American Institute of Aeronautics and Astronautics, 2022, AIAA 2022–1746.